이학박사 학위논문

The Tip of the Red Giant Branch Distances to Type Ia Supernova Host Galaxies and the Hubble Constant

적색거성가지 최대밝기를 이용한 제1a형 초신성 모은하까지의 거리측정 그리고 허블상수

2016년 08월

서울대학교 대학원
물리천문학부 천문학전공
장 인 성

The Tip of the Red Giant Branch Distances to Type Ia Supernova Host Galaxies and the Hubble Constant

적색거성가지 최대밝기를 이용한 제1a형 초신성 모은하까지의 거리측정 그리고 허블상수

지도교수 이 명 균

이 논문을 이학박사 학위논문으로 제출함

2016년 06월

서울대학교 대학원

물리천문학부 천문학전공

장 인 성

장 인 성의 이학박사 학위논문을 인준함

2016년 08월

위 원 장 _____

부 위 원 장 _____

위 원 _____

위 원 _____

위 원 _____

The Tip of the Red Giant Branch Distances to Type Ia Supernova Host Galaxies and the Hubble Constant

by

In Sung Jang
(isjang@astro.snu.ac.kr)

A dissertation submitted in partial fulfillment of the requirements for the degree of

Doctor of Philosophy

in

Astronomy

in

Astronomy Program
Department of Physics and Astronomy
Seoul National University

Committee:

Professor	Myungshin Im
Professor	Myung Gyoon Lee
Professor	Jounghun Lee
Professor	Sung-Chul Yoon
Professor	Deokkeun An

To My Family

For Their Endless Love and Support

throughout My Entire Life

ABSTRACT

Measuring the value of the Hubble constant is a fundamental step in extragalactic astronomy and cosmology. A tremendous work to determine the value of the Hubble constant has been carried out over the past decades. However, the estimated values have been controversial until recently. Type Ia Supernovae (SNe Ia) are one of the most powerful indicators for distant galaxies in the cosmic expansion dominated field ($d \gtrsim 100$ Mpc). The value of the Hubble constant can be obtained from the absolute calibration of SNe Ia. Previous absolute calibrations of SNe Ia were carried out using Cepheids, a population I distance indicator. However, recent values of H_0 show a significant discrepancy with the values from the Cosmic Microwave Background Radiation (CMBR) analysis. It is called "the Hubble tension", being an issue in the modern cosmology. The Tip of the Red Giant Branch (TRGB) is a precise and population II distance indicator for resolved stellar systems. It has several advantages over over the Cepheids. An absolute calibration of SNe Ia with the TRGB will be useful for more accurate calibration of SNe Ia and the Hubble constant.

We present the results of an absolute calibration of SNe Ia based on the TRGB. In order to derive an accurate calibration of SNe Ia, we refine the TRGB calibration. A modified TRGB calibration corrected for the color (metallicity) dependence of the TRGB, the QT magnitude, is introduced for better detection of the TRGB. We determine the color-magnitude relation of the TRGB from photometry of deep images of HST/ACS fields around eight nearby galaxies. The zero-point of the TRGB at the fiducial metallicity ([Fe/H] $= -1.6, (V-I)_{0,TRGB} = 1.5$)) is obtained from photometry of two distance anchors, NGC 4258 (M106) and the LMC, to which precise geometric distances are known: $M_{I,TRGB} = -4.121 \pm 0.067$ mag from NGC 4258 and $M_{I,TRGB} = -4.033 \pm 0.063$ mag from the LMC. A weighted mean of the two zero-points is $M_{I,TRGB} = -4.074 \pm 0.046$ mag. The quoted uncertainty is $2 \sim 3$ times smaller than those of the previous calibrations.

With the revised TRGB calibration, we determine the distances to eight SN Ia host galaxies: M101 hosting SN 2011fe, M66 hosting SN 1989B, M96 hosting SN 1998bu, NGC 4038/39 hosting SN 2007sr, NGC 5584 hosting SN 2007af, NGC 3021 hosting SN 1995al, NGC 3370 hosting SN 1994ae, and NGC 1309 hosting SN 2002fk. Luminosity functions of red giant stars in the outer regions of these galaxies show the TRGB to range from $I \approx QT = 25.083 \pm 0.034$ (M101) to 28.398 ± 0.048 (NGC 1309) mag. The TRGB distances to these galaxies are estimated to range from $(m - M)_0 = 29.168 \pm 0.034$ (M101) to 32.475 ± 0.048 (NGC 1309). By combining the TRGB distance estimates to SN Ia host galaxies derived from this study with the SN Ia calibration provided by Riess et al. (2011), we obtain a value of the Hubble constant: $H_0 = 71.15 \pm 1.80$(random) $\pm$ 1.51(systematic) km s^{-1} Mpc^{-1}(a 3.3% uncertainty including systematics) from all eight SNe, and $H_0 = 72.95 \pm 2.03$(random) $\pm$ 1.55(systematic) km s^{-1} Mpc^{-1}(a 3.5% uncertainty including systematics) from six low-reddened SNe. We obtain our best estimate, $H_0 = 70.45 \pm 1.67$(random) $\pm$ 1.65(systematic) km s^{-1} Mpc^{-1}(a 3.2% uncertainty including systematics), from the combination of the absolute magnitude of six low-reddened SNe with the recent SN Ia calibration given by Riess et al. (2016). This value is between those from Cepheid calibrated SNe Ia and those from CMB analysis.

Keywords: galaxies: distances and redshifts – galaxies: individual (M66, M96, M101, NGC 1309, NGC 3021, NGC 3370, NGC 4038/39, NGC 4258, and NGC 5584) – galaxies: stellar content – supernovae: individual (SN 1989B, SN 1994ae, SN 1995al, SN 1998bu, SN 2002fk, SN 2007af, SN 2007sr, and SN 2011fe)

Student Number: 2011-30130

Contents

List of Figures

List of Tables

Chapter 1

INTRODUCTION

1.1 Introduction

1.1.1 Determining Cosmological Parameters and the Hubble constant

An accurate determination of cosmological parameters as well as the Hubble constant is a crucial step for precision cosmology. A tremendous work to estimate the value of H_0 has been conducted over the past few decades and the accuracy of the measured values of H_0 has improved dramatically. In the 20th century, the value of the Hubble constant was very uncertain, ranging from $H_0 = 50$ to 100 km s^{-1} Mpc^{-1} with large uncertainties (de Vaucouleurs & Peters 1981; de Vaucouleurs 1993; Sandage & Tammann 1974a,b,c,d, 1975a,b, 1976; van den Bergh 1960a,b, 1975, 1994). The value of H_0 has settled down to around the middle of them, $H_0 \sim 70$ km s^{-1} Mpc^{-1} with the advent of Hubble Space Telescope (HST) (Freedman et al. 2001; Sandage et al. 2006). Recent estimations yielded values with accuracy reaching the $3 \sim 5\%$ level from Cepheid calibrated SNe Ia (Freedman et al. 2012; Riess et al. 2011; Riess et al. 2016). Not only for H_0 but also for other cosmological parameters ($\Omega_b, \Omega_m, \Omega_\Lambda, \tau, n_s$, and A) are being improved with similar accuracy. All these cosmological parameters have played a key role in constructing the standard cosmological model, called "the

concordance model" (Spergel et al. 2007; Komatsu et al. 2011; Planck Collaboration et al. 2015).

Although the accuracy of these cosmological parameters has been improved and the range of measured values of the cosmological parameters has narrowed, there is still a serious conflict between the values of the Hubble constant measured from the classical distance ladder method and from the inverse distance ladder method. The classical distance ladder method uses stellar or geometric distance indicators (e.g. Cepheids, supernovae, RR-Lyrae, red giant stars, and megamasers) to derive distances to external galaxies and a value of the H_0. Recent progresses on the classical distance ladder method have been focusing on the calibration of Type Ia Supernovae (SNe Ia). Supernovae and H_0 for the equation of state (SH0ES, (Riess et al. 2011)) and Carnegie Hubble Program (CHP, (Freedman et al. 2012)) measured distances to eight Type Ia supernova (SN Ia) host galaxies using Cepheids. From the mean absolute peak luminosity of SNe Ia, they derived a value of the Hubble constant: $H_0 = 74.8 \pm 3.1$ km s^{-1} Mpc^{-1}(Riess et al. 2011) and 74.3 ± 2.1 km s^{-1} Mpc^{-1}(Freedman et al. 2012). More recently, the SH0ES project presented an updated value, $H_0 = 73.02 \pm 1.79$ km s^{-1} Mpc^{-1} from 18 SN Ia host galaxies with Cepheid distances (Riess et al. 2016). These three estimations agree very well within uncertainties.

However, these values of H_0 are somewhat larger than those from the inverse distance ladder method. The inverse distance ladder method is based on the measurement of high-z sources including CMBR and Baryon Acoustic Oscillation (BAO) to determine the value of H_0. Bennett et al. (2013) derived the cosmological parameters from the analysis of the angular power spectrum of CMBR in WMAP9 assuming a flat ΛCDM cosmology, and presented $H_0 = 69.32 \pm 0.80$ km s^{-1} Mpc^{-1}. Later, the Planck Collaboration led to an even smaller value of the Hubble constant, $H_0 = 67.8 \pm 0.9$ km s^{-1} Mpc^{-1}, using new CMBR data from the Planck satellite (Planck Collaboration et al. 2014, 2015). It is noted that the errors of these estimates are much smaller than those based on SNe Ia. In addition, recent studies of

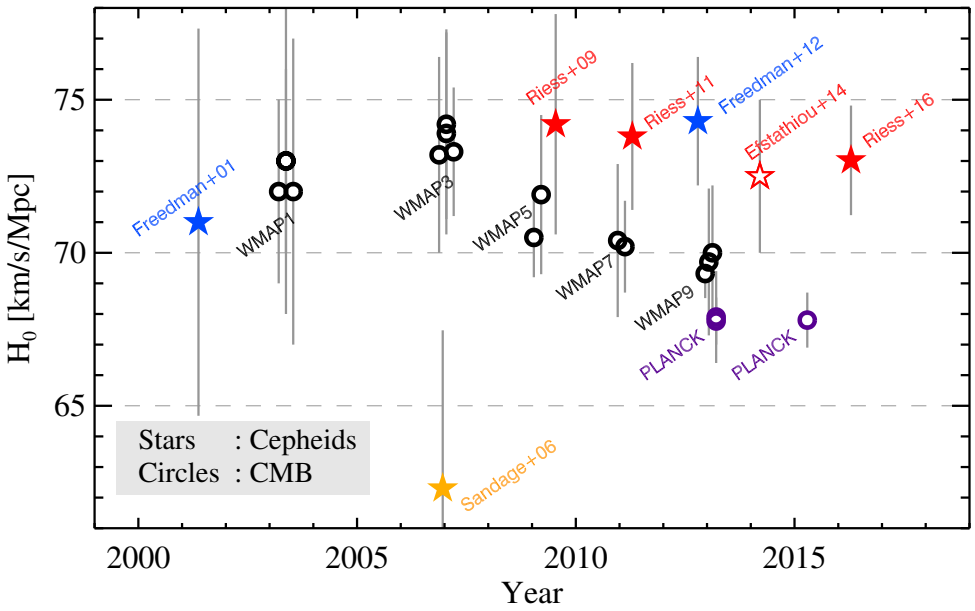

Figure 1.1: A comparison of H_0 estimates from recent studies based on the Cepheid calibrated SNe Ia (starlets), and the CMB analysis (circles). One open star denotes the revised value of H_0 based on the revised water maser distance to NGC 4258 (Efstathiou 2014). Note the systematic difference between the values of H_0 from the Cepheid calibrated SNe Ia and those from the CMB analysis.

the BAO in the range of redshift combined with SNe Ia data have shown similar values to those from CMBR analysis (Aubourg et al. 2015).

Figure 1.1 shows the distribution of recent determinations of H_0 as a function of time. Starlets and circles indicate the values of H_0 from the two independent methods: the classical distance ladder method (Cepheid calibrated SNe Ia, starlets) and the inverse distance ladder method (CMB analysis, circles). A few features are noted. First, in the early 2000s, two independent estimates of H_0 provided similar results: $H_0 = 71 \pm 2(\text{random}) \pm 6(\text{systematic})$ km s^{-1} Mpc^{-1}(the Hubble Key Project (Freedman et al. 2001)) and $H_0 = 73 \pm 3$ (WMAP1 (Spergel et al. 2003)). Second, the value, $H_0 = 62.3 \pm 1.3(\text{random}) \pm 5.0(\text{systematic})$ km s^{-1} Mpc^{-1}presented by Sandage et al. (2006), is significantly lower than all other estimations. Third, the values of H_0 from the CMB analysis has been decreasing since 2007. Whereas, those from the Cepheid calibrated SNe Ia stay at higher values, so that recent estimations of H_0 between these two methods show $2 \sim 3\sigma$ systematic difference.

This systematic difference is called "the Hubble tension" being one of the most important issues in the modern cosmology. It has yet to be confirmed whether the discrepancy is signaling new physics or the result of systematic errors. Both methods show some systematic effects that need to be refined (Efstathiou 2014; Addison et al. 2016). This thesis is aiming to improve the SN Ia calibration for the classical distance ladder method.

1.1.2 SNe Ia as a Cosmological Probe

SNe Ia are among the brightest stellar objects in the Universe. The typical absolute peak magnitude of SNe Ia is $M_V \simeq -19.2$ mag. It is comparable to the absolute magnitudes of bright galaxies. Although the underlying physics of SNe Ia is still needed to be investigated, SNe Ia have been used as a powerful extragalactic distance indicator.

The calibration of SNe Ia as a distance indicator has a long history. An implication of Type I SNe as a distance indicator was suggested first by Kowal (1968). He compiled light curves of 33 SNe, including 22 Type I SNe, and derived a mean absolute peak magnitude of Type I SNe: $M_{pg} = -18.6 + 5log(H_0/100)$ with a dispersion

of 0.61 mag, where M_{pg} is the photographic magnitude. From this, he suggested that Type I SNe can be exceedingly useful distance indicators for external galaxies. During the 1970s and the early 1990s there have been a number of studies for the calibration of SNe Ia. (Barbon et al. 1975; Branch & Bettis 1978; Sandage & Tammann 1982; Cadonau et al. 1985; Capaccioli et al. 1990; Tammann & Leibundgut 1990; Fukugita & Hogan 1991; Branch & Tammann 1992; van den Bergh & Pazder 1992). However, derived mean absolute magnitudes of SNe Ia showed a sizeable scatter ($M_B = -18 \sim -20$ mag) with large uncertainties ($\sigma = 0.5 \sim 1.0$ mag).

SNe Ia as precise distance indicators was established by Phillips (1993). He reported that there is a strong relationship between the absolute peak luminosities of SNe Ia and the decline rates of SNe Ia light curves (Δm_{15}). This means that bright SNe Ia fade slowly, whereas faint SNe Ia fade rapidly, as shown in Figure 1.2. Applying the correction for the decline rate, the luminosity dispersion of SNe Ia can be decreased from 0.59 mag to 0.28 mag in the V-band (Phillips 1993). Riess et al. (1995) presented a revised light curve fitting method that uses empirical light curve templates. Applying the revised method, Riess et al. (1995) derived even smaller V-band luminosity dispersion of SNe Ia, $\sigma_V = 0.21$ mag. Modern light curve fitting methods (using MLCS2k2, SALT, and SNooPy) combining with well monitored SN Ia light curves provide smaller luminosity dispersions of $0.13 \sim 0.16$ mag in the optical wavelength (Guy et al. 2005; Jha et al. 2007; Guy et al. 2010; Burns et al. 2011; Riess et al. 2016). SNe Ia are being one of the most powerful and precise distance indicators for galaxies in the cosmic expansion dominated field ($d \gtrsim 100$ Mpc).

SNe Ia have played an important role in constructing modern cosmology. In the Friedmann-Robertson-Walker cosmological model, the luminosity distance D_L can be expressed as a function of cosmological parameters as well as the redshift, z:

$$D_L = cH_0^{-1}(1+z)\,|\Omega_k|^{-1/2}\, sinn\left\{|\Omega_k|^{1/2} \times \int_0^z [(1+z)^2(1+\Omega_M z) - z(2+z)\Omega_\Lambda]^{-1/2} dz\right\}$$

where c is the speed of light, H_0 is the Hubble constant, Ω_M is the matter density

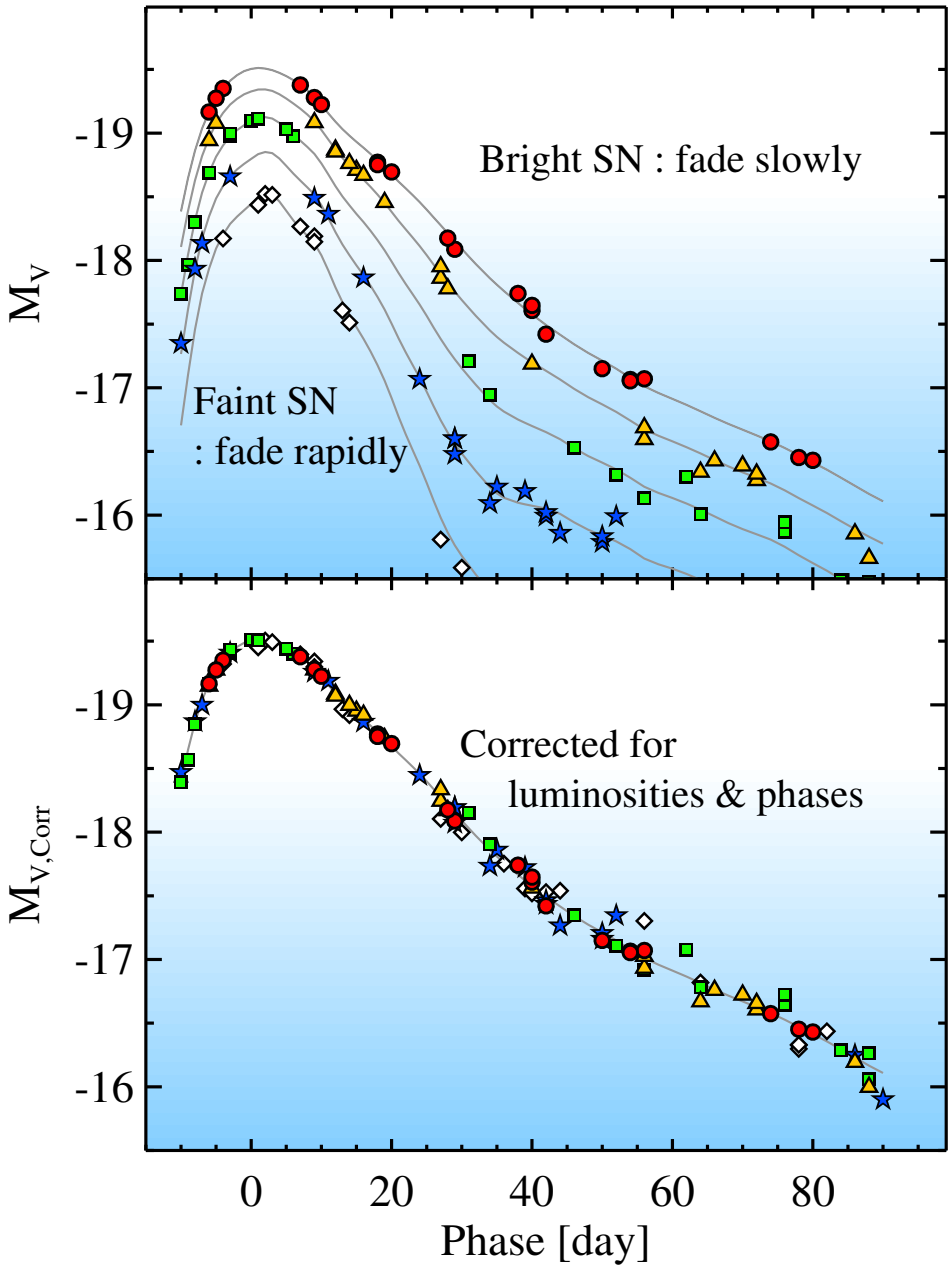

Figure 1.2: A schematic view of SN Ia light curves. (Top) V-band light curves of SNe Ia that show different decline rates (Δm_{15}). Bright SNe Ia tend to fade slowly, whereas faint SNe Ia are fading rapidly. (Bottom) light curves of SNe Ia corrected for luminosities and phases differences by stretching the time scale of of each light curve.

parameter, Ω_Λ is the dark energy density parameter, Ω_k is $1 - \Omega_M - \Omega_\Lambda$, and sinn is sinh and sin for $\Omega_k \geq 0$ and $\Omega_k \leq 0$, respectively. Since SNe Ia are bright standardizable candles, they can be used to derive cosmological parameters.

Figure 1.3 shows a Hubble diagram for 588 SNe Ia obtained from the Supernova Cosmology Project (the Union2.1 compilation (Suzuki et al. 2012)). Overlaid three guide lines represent different cosmologies. SNe Ia data are fitted well by $\Omega_M = 0.31$ and $\Omega_\Lambda = 0.69$ model, whereas the two models without dark energy density ($\Omega_\Lambda = 0.00$) show larger Hubble residuals. This suggests a necessity for introducing the dark energy density parameter, Ω_Λ, in the cosmology. This type of analysis was carried out first by the two groups in the late 1990s: the High-z Supernova Search Team (Riess et al. 1998) and the Supernova Cosmology Project (Perlmutter et al. 1999).

Figure 1.3 implies a possibility that SNe Ia can be used to measure not only Ω_M and Ω_Λ, but also the Hubble constant, H_0. In the studies of Riess et al. (1998) and Perlmutter et al. (1999), they estimated distances to SNe Ia based on the radial velocity of SNe Ia by assuming a value of H_0 ($= 65$ km s^{-1} Mpc^{-1}(Riess et al. 1998) and $= 63$ km s^{-1} Mpc^{-1}(Perlmutter et al. 1999)). Distances to SNe Ia can also be measured by comparing the apparent magnitude and the absolute magnitude of the SNe Ia ($(m - M)_0 = 5log(v/H_0) - 5$). Since we know the radial velocity (v) and the apparent magnitude (m) of each SN Ia, H_0 can be obtained by determining the absolute magnitude (M) of SNe Ia. This is being one of the most powerful routes to measure H_0 based on the distance ladder method.

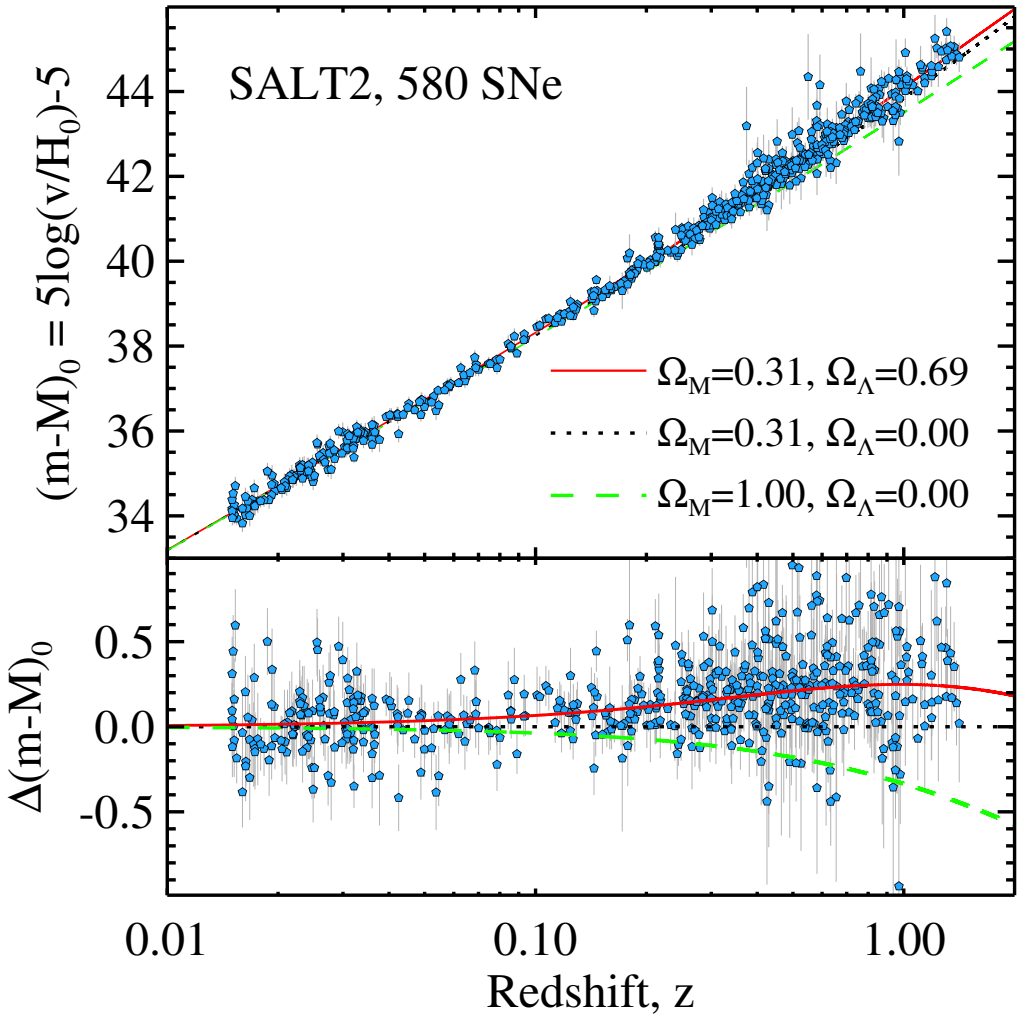

Figure 1.3: A Hubble diagram for 580 SNe Ia provided by the Supernova Cosmology Project (the Union2.1 compilation (Suzuki et al. 2012)). Three guide lines are overlaid: $\Omega_M = 0.31$ and $\Omega_\Lambda = 0.69$ model (solid line), $\Omega_M = 0.31$ and $\Omega_\Lambda = 0.00$ model (dotted line), and $\Omega_M = 1.00$ and $\Omega_\Lambda = 0.00$ model (dashed line).

1.1.3 Luminosity calibration of SNe Ia through Cepheids

Cepheids are a class of variable stars that pulsate regularly changing their luminosities. A strong relationship between the period and the luminosity for Cepheids was discovered by Leavitt (1908) and Leavitt & Pickering (1912) from the analysis of variable stars in the Magellanic Clouds. Many follow up studies have been carried out over the past hundred years to improve the calibration of Cepheids (see Freedman & Madore (2010) and references therein for detail). Cepheids are now one of the most powerful distance indicators for resolved stellar systems.

With the Cepheids, several large projects were carried out to calibrate the absolute magnitude of SNe Ia and the corresponding value of the Hubble constant, as listed in Table 1.1. The Hubble Key Project on the extragalactic distance scale was one of the key projects for the HST in the 1990s. They measured the Cepheid distances to eight SN Ia host galaxies (NGC 4639, NGC 4536, NGC 3627, NGC 3368, NGC 5253, IC 4182, NGC 4496A, and NGC 4414) and obtained the mean absolute peak magnitude of SNe Ia, $M^0_{V,corr} = -19.37 \pm 0.05$. By combining the absolute magnitude with the supernova Hubble diagram that was constructed from 36 SNe Ia in the Hubble flow ($0.01 \leq z \leq 0.1$), they presented a value of the Hubble constant, $H_0 = 71 \pm 2(\text{random}) \pm 6(\text{systematic})$ km s^{-1} Mpc^{-1}(Freedman et al. 2001).

A few years later, however, the SN HST project presented a somewhat different value, $M^0_{V,corr} = -19.46 \pm 0.04$, from the Cepheid distances to ten SN Ia host galaxies (the above plus NGC 2841 and NGC 3982). By combining this with 62 SNe Ia in the Hubble flow ($0.01 \leq z \leq 0.1$) they obtained a value of the Hubble constant, $H_0 = 62.3 \pm 1.3(\text{random}) \pm 5.0(\text{systematic})$ (Sandage et al. 2006). The level of difference between the value of H_0 from the Hubble key project and that from the SN HST project is $\sim 1.5\sigma$.

A similar study was carried out by the the SH0ES group. Riess et al. (2011) and Riess et al. (2016) presented distance estimates to eight and eighteen SNe Ia host galaxies using Cepheids, respectively. They derived the value of the Hubble constant,

Table 1.1. A Summary of H_0 From Cepheid Calibrated SNe Ia

Program	Number of SNe Ia (Absolute calibration)	Number of SNe Ia (SN Ia Hubble diagram)	H_0 [km s^{-1} Mpc^{-1}]
Hubble Key Project (Freedman et al. 2001)	8 SNe Ia	36 SNe Ia	$71 \pm 2_r \pm 6_s$ (8.9%[a])
SN HST Project (Sandage et al. 2006)	10 SNe Ia	62 SNe Ia	$62.3 \pm 1.3_r \pm 5.0_s$ (8.3%)
SH0ES (Riess et al. 2011)	8 SNe Ia	140 SNe Ia	73.8 ± 2.4 (3.3%)
Carnegie Hubble Program (Freedman et al. 2012)	8 SNe Ia[b]	36 SNe Ia	74.3 ± 2.1 (2.8%)
SH0ES (Riess et al. 2016)	18 SNe Ia	233 SNe Ia	73.02 ± 1.79 (2.5%)

[a]Accuracy

[b]The same SNe Ia used in the Hubble Key Project (Freedman et al. 2001)

$H_0 = 73.8 \pm 2.4$ km s^{-1} Mpc^{-1} from Riess et al. (2011) and $H_0 = 73.02 \pm 1.79$ km s^{-1} Mpc^{-1} from Riess et al. (2016). Recently, the Carnegie Hubble Program updated their previous estimation of the Hubble Key Project by applying the revised distance to the LMC, $H_0 = 74.3 \pm 2.1$ km s^{-1} Mpc^{-1}(Freedman et al. 2012). These recent estimations agree well. However, these are $2 \sim 3\sigma$ larger than those of CMB analysis.

Although Cepheids play an important role in the study of the distance scale of the Universe, they have several disadvantages as calibrators for SNe Ia as follows. First, Cepheids are mostly young massive giant stars and they are found only in late type galaxies. SNe Ia explode not only in late type galaxies but also in early type galaxies. Thus, it is really difficult to measure Cepheid distances to early type galaxies that host SNe Ia (e.g. NGC 1316 hosting four SNe Ia, SN 1980N, SN 1981D, SN 2006dd, and SN 2006mr). Second, most of the bright Cepheids are located in star forming regions where internal extinctions are often significant. Additional extinction corrections to the Cepheid luminosity should be applied, which increases uncertainties. Third, it is known that the period-luminosity relation of Cepheids can be affected by the metallicity. However, the dependence on metallicity is still controversial ($\gamma_\mu = \delta(m-M)_0/\delta[O/H] = -0.2 \sim -0.4$, Gerke et al. 2011)

Current luminosity calibrations of SNe Ia in the literature are mainly based on Cepheids. An independent calibration of SNe Ia without Cepheids would be useful for more accurate calibration of SNe Ia and the Hubble constant. The TRGB can be a good alternative to the Cepheids.

1.1.4 The TRGB as a Distance Indicator

The TRGB represents the brightest part of the Red Giant Branch (RGB) in the color-magnitude diagrams (CMDs) of old stellar systems such as globular clusters and halos in galaxies. It corresponds to the core-He flash point in the evolutionary stages of low mass stars. In comparison with Cepheid variables, which are well known precise distance indicators, the TRGB has several advantages. First, the

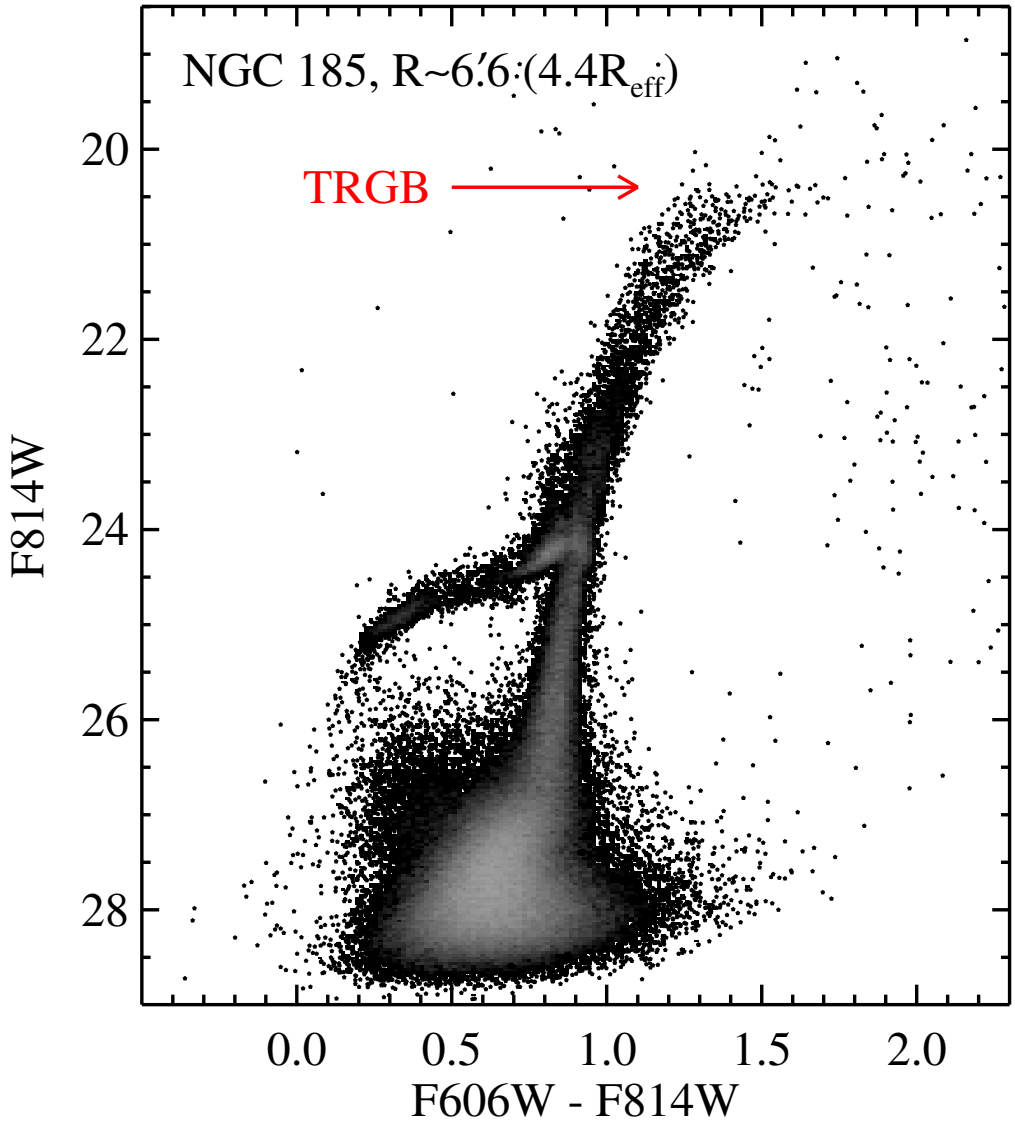

Figure 1.4: F814W–(F606W–F814W) CMD of resolved stars in the outer region ($R \sim 4.4R_{eff}$) of NGC 185 (E3 pec). We obtained the photometry of resolved stars from the archival ACS/WFC images of NGC 185 (PID = 11724) used by Geha et al. (2015). The TRGB represents the brightest part of RGB of old stellar systems as marked by the red arrow.

TRGB method uses Population II RGB stars. It enables the measurement of the distances to both early type galaxies and late type galaxies, while Cepheid variables can be used only for late type galaxies. Second, the TRGB method mainly uses RGB stars in the halo regions, where stellar densities are low and internal extinctions are negligible, while Cepheid variables are located in the star-forming regions where internal extinctions are often significant. Third, the TRGB stars are non-variable stars, so that a single epoch observation is enough to get distances, while Cepheids require many epochs of observations.

On the other hand, the TRGB has the disadvantage that its luminosity is relatively fainter than the bright Cepheid variables. The absolute V-band magnitude of the brightest Cepheid variable is estimated to be $M_V \sim -7$ mag, about 4.5 mag brighter than that of the TRGB, $M_V \sim -2.5$ mag. This difference becomes smaller in the longer wavelength: Δmag = 3.9, 3.1, 2.6 and 2.6 mag in I, J, H, and K_S bands, respectively (Macri et al. 2006, 2015, assuming the maximum period of Cepheid variables (P_{max}) = 100 days). Thus, the TRGB as a distance indicator can be enhanced in the near infrared wavelength.

The TRGB enables the investigation of the distance scale of the Universe and the value of the Hubble constant without Cepheids. The two independent routes to H_0 will be useful in checking the robustness of the distance ladder method. Tammann & Reindl (2013) presented a luminosity calibration of SNe Ia based on the TRGB calibrated six SNe Ia: SN 2011fe in M101, SN 2007sr in NGC 4038/39, SN 1989B in M66, SN 1998bu in M96, SN 1972E in NGC 5253, and SN 1937C in IC 4182. Combining the mean absolute magnitude of SNe Ia ($M_V^0 = -19.41 \pm 0.05$) with the 62 SNe Ia in the Hubble flow ($3,000 < V < 20,000$ km s$^-$1), they derived a value of the Hubble constant, $H_0 = 63.7 \pm 2.3$ km s^{-1} Mpc^{-1}, which is significantly lower than those from the Cepheid calibrated SNe Ia ($H_0 \sim 74$ km s^{-1} Mpc^{-1}(Freedman et al. 2012; Riess et al. 2016)). It is noted, however, that they used heterogeneous TRGB distance estimates derived from various literature. Moreover, four of the six SNe Ia used in their study are old SNe that were observed using photographic or photoelec-

tric detectors (SN 1937C and SN 1972E), or highly reddened SNe (SN 1989B and SN 1998bu). Thus, absolute magnitudes derived from these old or highly reddened SNe are probably less reliable. It is needed to carry out the luminosity calibration of SNe Ia using the low-reddened modern SNe Ia based on the homogeneous analysis of the TRGB.

1.1.5 Purpose of This Thesis

This thesis is aiming to determine the value of the Hubble constant accurate to 3% using the distance ladder method. To attain this goal, I calibrate the absolute magnitude of SNe Ia, which are powerful distance indicators for external galaxies in the Hubble flow ($d \gtrsim 100 Mpc$). I use the TRGB, a population II distance indicator, to measure distances to SN Ia host galaxies. Combining the absolute magnitude of SNe Ia with the supernova Hubble diagram, I determine the value of the Hubble constant. The value of H_0 derived in this study will be a good reference on the controversy over the value of H_0 between from Cepheid calibrated SNe Ia and from CMB analysis.

This thesis is composed of seven Chapters as follows. Chapter 2 presents the TRGB distance to M101 (NGC 5457) hosting SN 2011fe, which is one of the nearest SNe Ia with the modern photometry. In Chapter 3, I address the distances to M66 (NGC 3627) and M96 (NGC 3368), in the Leo I group, based on the TRGB. These two galaxies host two SNe Ia, SN 1989B and SN 1998bu, which belong to the nearest SNe Ia group. In Chapter 4, I derive the TRGB distances to two additional galaxies, NGC 4038/39 and NGC 5584, hosting SN 2007sr and SN 2007af, respectively. Chapter 5 describes the revised calibration of the TRGB accurate to 2.4%. In Chapter 6, I present the TRGB distances to three SN Ia host galaxies, NGC 3021 hosting SN 1995al, SN 3370 hosting SN 1994ae, and NGC 1309 hosting SN 2002fk with the revised TRGB calibration presented in Chapter 5. I also update the TRGB distances to five SN Ia host galaxies presented in Chapter 2, 3, and 4. From the TRGB distance estimates to eight SN Ia host galaxies, I calibrate the absolute peak

magnitude of SNe Ia and corresponding a value of the Hubble constant. Primary results are summarized in the final Chapter.

Chapter 2

The Distance to M101 Hosting SN Ia 2011fe Based on the TRGB

2.1 Introduction

M101 (NGC 5457) is a well-known face-on spiral galaxy (SAB(rs)cd) in the M101 group. In 2011 a new Type Ia supernova (SN Ia) 2011fe was discovered in this galaxy, being the fourth SN discovered in the same galaxy (Nugent et al. 2011; Liu et al. 2012; Richmond & Smith 2012). It is one of the nearest among the known galaxies hosting SNe Ia. SN 2011fe suffers little from interstellar extinction ($A_V \sim 0.04$) and was discovered in less than one day after explosion(Nugent et al. 2011). Therefore it plays an important role for calibrating the absolute luminosity of SNe Ia as well as for studying the properties of SNe Ia including their progenitors (Reindl et al. 2005; Nugent et al. 2011; Tammann & Reindl 2012; Bloom et al. 2012; Röpke et al. 2012; Matheson et al. 2012).

Surprisingly recent measurements of the distance to M101 show a large range, $(m - M)_0 = 29.04$ to 29.71 (Shappee & Stanek (2011); Matheson et al. (2012);

Vinko et al. (2012) and references therein). Even the measurements based on two primary distance indicators, Cepheids and the tip of the red giant branch (TRGB) (Lee et al. 1993), show a significant dispersion: $(m - M)_0 = 29.04$ to 29.71 for Cepheids (Kelson et al. 1996; Kennicutt et al. 1998; Stetson et al. 1998; Freedman et al. 2001; Macri et al. 2001; Saha et al. 2006; Shappee & Stanek 2011), and $(m - M)_0 = 29.05$ to 29.42 for the TRGB (Sakai et al. 2004; Rizzi et al. 2007; Shappee & Stanek 2011). Note that one of the most recent estimates, Shappee & Stanek (2011), shows significant differences in both Cepheid and TRGB distances from previous ones. Therefore the distance to M101 is still significantly uncertain in spite of its importance. Consequently, a determination of the Hubble constant based solely on the photometry of SN 2011fe and previously-published distances can yield values ranging from 56 to 76 km s^{-1} Mpc^{-1} (Matheson et al. 2012).

In this study we present a new determination of the distance to M101 using the TRGB, from the images for several fields within this galaxy available in the *Hubble Space Telescope* (HST) archive. While previous studies to derive the TRGB distances to M101 were based on one or two fields, we used nine fields. This allows us to estimate the M101 distance with much smaller statistical uncertainty than previous studies.

2.2 Data Reduction

We used $F555W$ and $F814W$ images of M101 taken with the HST/Advanced Camera for Surveys (ACS) (Proposal IDs: 9490, 9492, and 10918) and with the WFPC2 (Proposal ID: 8584). Figure 2.1 displays a finding chart for M101, showing the HST fields used in this study (F1, F2, F3, F4, F5, and F6) and previous studies (S1 and S2 in Shappee & Stanek (2011) and S04 in Sakai et al. (2004)). Note that the S04 field is isolated in the outskirts of the disk, while S1 and S2 are much closer to the center than the other fields. Two fields used in previous Cepheid studies (Kelson et al. 1996; Kennicutt et al. 1998) are denoted by 'outer' and 'inner', respectively.

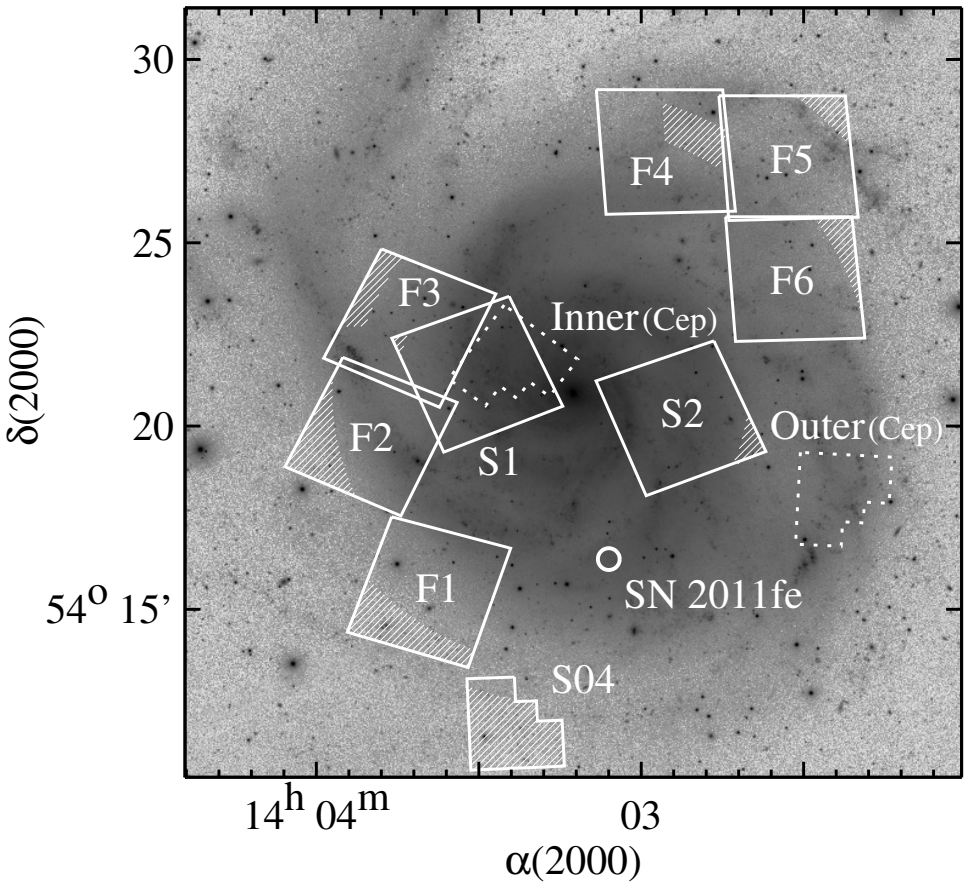

Figure 2.1: Location of the HST fields marked on the gray scale map of a $21' \times 21'$ SDSS i-band image of M101. F1, F2, F3, F4, F5, and F6 represent the fields used in this study, S1 and S2 used in Shappee & Stanek (2011), and S04 in Sakai et al. (2004). Two fields used in previous Cepheid studies (Kelson et al. 1996; Kennicutt et al. 1998) are labeled by 'outer' and 'inner', respectively. Only the hatched regions were used in the analysis. North is up and east to the left.

We derived instrumental magnitudes of point sources in the ACS images using the IRAF/DAOPHOT package that is designed for point spread function (PSF) fitting photometry (Stetson 1994). We used 2-σ as the detection threshold, and derived the PSFs using isolated bright stars in the images. We derived aperture corrections using a large aperture with radius of $1''$ for several isolated bright stars in the images. The uncertainties associated with aperture correction are on average 0.02 mag for both filters. We transformed the instrumental magnitudes into the standard Johnson-Cousins VI magnitudes, following equations (1) and (12) for observed magnitudes of Sirianni et al. (2005). In the case of WFPC2 images we used Dolphot (http://americano.dolphinsim.com/dolphot/). The uncertainties associated with the photometric transformations are on average 0.02 mag.

2.3 Results

2.3.1 Color-magnitude Diagrams of Resolved Stars

M101 is an almost face-on galaxy (inclination angle = 17 deg (Zaritsky et al. 1990)) and all HST fields available in the archive are overlapped with the disk of the galaxy so that they must include a mixture of disk stars and old halo stars. To reduce the fraction of young disk stars as much as possible in constructing the color-magnitude diagrams (CMDs) for each field, we chose the stars located away from the spiral arms of star-forming regions in each field. Thus selected regions in each field are marked by the hatched region in Figure 2.1. Foreground reddening toward M101 is known to be very small, $E(B-V) = 0.008$ (Schlegel et al. 1998; Schlafly & Finkbeiner 2011). Corresponding values are $A_I = 0.013$ and $E(V-I) = 0.010$. Internal reddening for red giants in the arm-free regions of this face-on galaxy is expected to be negligible so that it is not corrected in the following analysis.

Figure 2.2 displays the CMDs for the stars in the selected regions of F1, F2, F3, F4, F5, F6, (S1 + S2), and S04 fields. The CMDs for all fields show a prominent red giant branch (RGB) as well as weaker asymptotic giant branch (AGB), massive

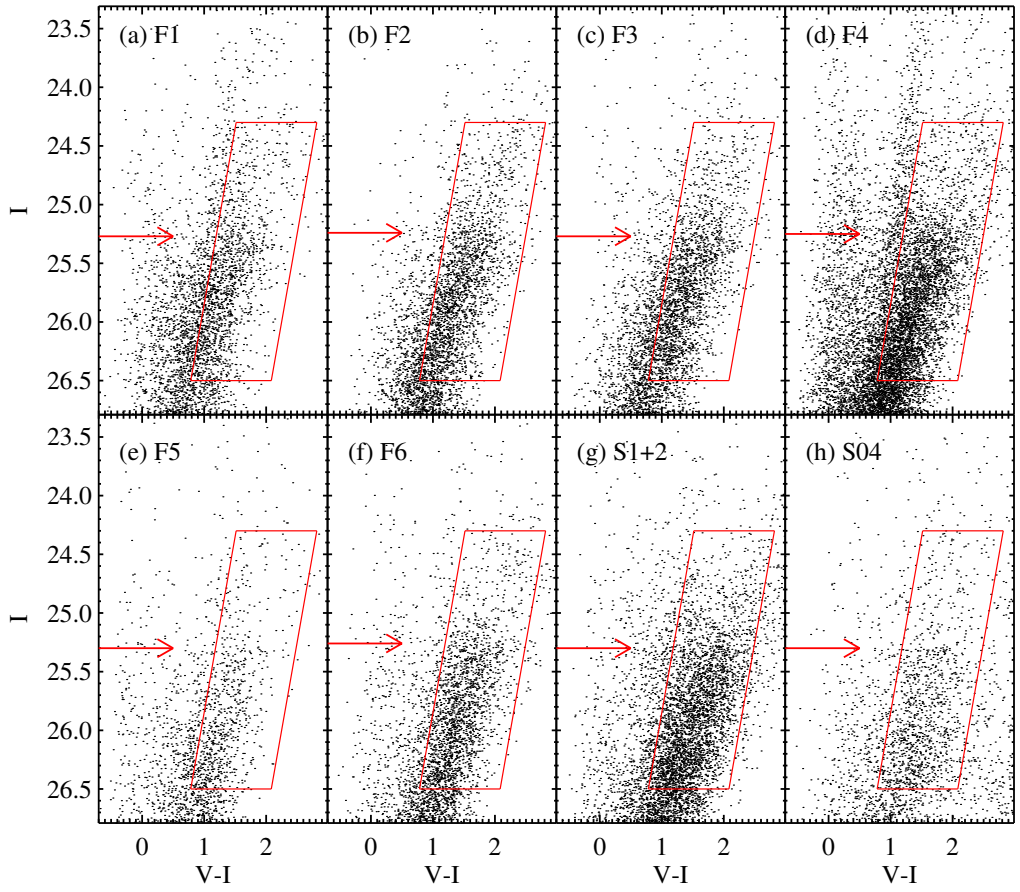

Figure 2.2: $I-(V-I)$ color-magnitude diagrams of the stars in the arm-free regions in each field of M101. Note the the prominent RGBs are seen as well as other weaker features. Boxes represent the boundary of the red giants used for deriving the luminosity functions of the red giant stars in each field. Arrows represent the positions of the TRGB.

giants, and blue main sequence. These RGBs are useful for estimating the magnitude of the TRGB and the distance to M101.

2.3.2 Distance Estimation

We determined the distance to the target fields using the TRGB method, which is known to be an excellent distance indicator for resolved stellar systems (Lee et al. 1993; Sakai et al. 1996; Méndez et al. 2002; Bellazzini 2008; Mouhcine et al. 2010; Salaris 2011). First we derived the I-band luminosity functions of the red giants in each field using the stars inside the boundary marked in Figure 2.2, and plotted them in Figure 2.3. Figure 2.3 shows that there appears to be a sudden jump at $I \approx 25.3$ mag in each field, which corresponds to the TRGB.

Using the edge-detecting algorithm (Sakai et al. 1996; Méndez et al. 2002; Mouhcine et al. 2010), we determined the TRGB magnitude more quantitatively. We calculated an edge-detection response function $E(m)$ $(= \Phi(m + \sigma_m) - \Phi(m - \sigma_m)$ where $\Phi(m)$ is the luminosity function of magnitude m and σ_m is the mean photometric error within a bin of ± 0.05 mag about magnitude m), as shown in Figure 2.3. The errors for the TRGB magnitudes were determined using bootstrap resampling method with one million simulations. In each simulation we resampled randomly the RGB sample with replacement to make a new sample of the same size. We estimated the TRGB magnitude for each simulation using the same procedure, and derived the standard deviation of the estimated TRGB magnitudes. The median color of the TRGB is derived from the colors of the bright red giants close to the TRGB.

We used the recent calibration for the absolute magnitude of the TRGB given in Rizzi et al. (2007): $M_{\mathrm{I,TRGB}} = -4.05(\pm 0.02) + 0.217(\pm 0.01)((V-I)_0 - 1.6)$ (where $(V-I)_0$ is a reddening corrected color of the TRGB), which is very similar to that given in Tammann et al. (2008). Then we calculate the distance modulus using $(m-M)_0 = I_{0,\mathrm{TRGB}} - M_{\mathrm{I,TRGB}}$.

We also derived the distance using the composite magnitude T for the RGB

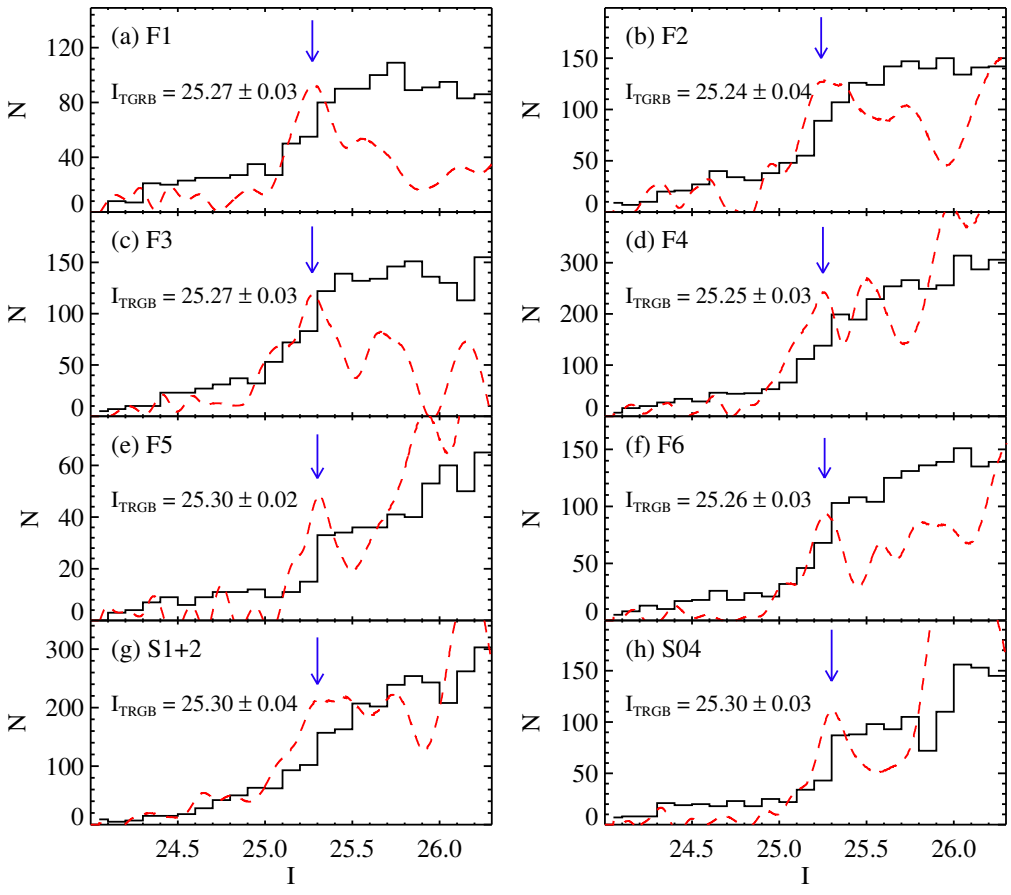

Figure 2.3: *I*-band luminosity functions of the red giants in each field of M101 (solid line histograms). Dashed lines represent edge-detection responses, and arrows represent the positions of the TRGB.

introduced in Madore et al. (2009): $T = I_{0,TRGB} - 0.20[(V-I)_0 - 1.5)]$ and $(m - M)_0 = T - M_{I,TRGB} = I_{0,TRGB} - 0.20(V-I)_0 + 4.35$. This calibration is based on the absolute TRGB magnitude of $M_{I,TRGB} = -4.05$ for $(V-I)_0 = 1.5$, similar to the calibration in Rizzi et al. (2007).

Table 2.1 lists a summary of the distance determination for the fields in M101 derived in this study, which is also shown in Figure 2.4. Table 2.1 includes I-band magnitudes of the TRGB, T magnitudes of the RGB, $(V-I)$ color of the RGB (before foreground reddening correction), absolute I-band magnitudes of the TRGB, and distance moduli from I-band magnitudes and T magnitudes. Remarkably the I-band magnitudes of the TRGB derived for all nine fields show a small range from 25.24 (F2) to 25.30 (F5, S1, S2 and S04). A weighted mean value is derived to be $I_{\rm TRGB} = 25.28 \pm 0.01$ (where the error is a standard error) with a standard deviation of only 0.02. Similarly the distance moduli for all fields show a small range from $(m-M)_0 = 29.26 \pm 0.03$ (F4) to 29.33 ± 0.02 (F5). We derive a weighted mean value of distance modulus $(m - M)_0 = 29.30 \pm 0.01$ where 0.01 is a random error, corresponding to a linear distance of 7.24 ± 0.03 Mpc. Its systematic error is estimated to be 0.12, considering (a) the TRGB calibration error of 0.12 (Bellazzini et al. 2001, 2004; Mager et al. 2008), (b) the aperture correction error of 0.02, (c) and the standard calibration error of 0.02 for ACS/WFC (Sirianni et al. 2005) and 0.07 for WFPC2 (Stetson 1998). Similar results are obtained from the T magnitude method, $(m - M)_0 = 29.26 \pm 0.01$, but with three times larger standard deviation (0.07). We adopt the results from the traditional I-band magnitude method, as the distance to M101, which shows a smaller scatter than the T magnitude results.

2.4 Discussion

2.4.1 Comparison with Previous Distance Estimates

We compare our estimates for the distance to M101 with those in the literature based on TRGB, Cepheids, and SN Ia in Figure 2.4. Recently Shappee & Stanek

Table 2.1. A Summary of TRGB Distance Measurements of M101

Field	Region	I_{TRGB}	T_{RGB}	$(V-I)_{TRGB}$	$M_{I,TRGB}$	$(m-M)_{0,I}$	$(m-M)_{0,T}$
F1	$R_{GC} \geq 7'.5$	25.27 ± 0.03	25.19 ± 0.02	1.54 ± 0.04	-4.065 ± 0.009	29.32 ± 0.03	29.24 ± 0.02
F2	$R_{GC} \geq 6'.5$	25.24 ± 0.04	25.15 ± 0.03	1.60 ± 0.05	-4.052 ± 0.011	29.28 ± 0.04	29.20 ± 0.03
F3	$R_{GC} \geq 5'.9$, Dec $\geq 54\,^{\circ}.4$	25.27 ± 0.03	25.15 ± 0.04	1.66 ± 0.05	-4.039 ± 0.011	29.30 ± 0.03	29.20 ± 0.04
F4	$7'.3 \leq R_{GC} < 8'.3$, R.A. $< 210\,^{\circ}.73$	25.25 ± 0.03	25.24 ± 0.03	1.72 ± 0.06	-4.026 ± 0.013	29.26 ± 0.03	29.29 ± 0.03
F5	$R_{GC} \geq 10'.1$	25.30 ± 0.02	25.17 ± 0.02	1.65 ± 0.05	-4.041 ± 0.011	29.33 ± 0.02	29.22 ± 0.02
F6	$R_{GC} \geq 8'.1$	25.26 ± 0.03	25.26 ± 0.04	1.71 ± 0.05	-4.028 ± 0.011	29.28 ± 0.03	29.31 ± 0.04
S1	$R_{GC} \geq 4'.75$	25.30 ± 0.04	25.29 ± 0.03	1.81 ± 0.04	-4.007 ± 0.009	29.29 ± 0.04	29.34 ± 0.03
S2	$R_{GC} \geq 4'.75$	25.30 ± 0.04	25.33 ± 0.03	1.91 ± 0.03	-3.985 ± 0.007	29.27 ± 0.04	29.38 ± 0.03
S1+2	$R_{GC} \geq 4'.75$	25.30 ± 0.04	25.33 ± 0.03	1.87 ± 0.05	-3.994 ± 0.011	29.28 ± 0.04	29.38 ± 0.03
S04	$R_{GC} \geq 8'.5$	25.30 ± 0.03	25.24 ± 0.03	1.81 ± 0.05	-4.007 ± 0.011	29.29 ± 0.03	29.29 ± 0.03
Weighted mean of F1∼6, S1+2 and S04		25.28 ± 0.01	25.21 ± 0.01	1.68 ± 0.02	-4.034 ± 0.004	29.30 ± 0.01	29.26 ± 0.01

(2011) derived a TRGB distance from the analysis of S1 and S2 fields, $(m-M)_0 = 29.05 \pm 0.06(\text{random}) \pm 0.12(\text{systematic})$. This value is 0.3 to 0.4 mag smaller than the previous TRGB distance estimates by Sakai et al. (2004) and Rizzi et al. (2007). The TRGB magnitudes for M101 derived in the previous studies are $I_{0,\text{TRGB}} = 25.40 \pm 0.04$ in Sakai et al. (2004), 25.29 ± 0.08 in Rizzi et al. (2007), and $T = 25.00 \pm 0.06$ in Shappee & Stanek (2011). Therefore the large difference among the previous TRGB distance estimates are mainly due to the difference in the measured TRGB magnitudes. Our mean value of the TRGB magnitudes (after foreground extinction correction), $I_{0,\text{TRGB}} = 25.27 \pm 0.01$ (and $T_{\text{RGB}} = 25.33 \pm 0.03$ for (S1+S2) fields) is close to the value in Rizzi et al. (2007), 0.13 mag brighter than the value in Sakai et al. (2004), and 0.33 mag fainter than the value in Shappee & Stanek (2011). Our values for the S04 field ($I_{0,\text{TRGB}} = 25.29 \pm 0.03$) and for the sum of S1 and S2 fields ($I_{0,\text{TRGB}} = 25.29 \pm 0.04$) are similar to the mean value of nine fields. The large difference in the TRGB magnitudes between this study and Shappee & Stanek (2011) is probably due to contamination by disk stars in the sample used by the latter.

The Cepheid distance estimates for M101 derived in the previous studies show a large range. Two HST fields in M101 (inner field and outer field, as shown Figure 2.1) were used for Cepheids in the previous studies. They show on average ~ 0.2 smaller values for the inner field (Stetson et al. 1998; Saha et al. 2006; Kennicutt et al. 1998; Macri et al. 2001; Shappee & Stanek 2011) than those for the outer field (Kelson et al. 1996; Kennicutt et al. 1998; Macri et al. 2001; Saha et al. 2006). This difference between the inner and outer fields may be considered to be mainly due to metallicity gradient in the galaxy disk. However, the distance modulus difference shows a large range from almost zero (Saha et al. 2006) to ~ 0.4 mag (Macri et al. 2001), depending on the authors. This difference has been explained. Saha et al. (2006) adopted a metallicity correction very similar to Freedman et al. (2001), which led them to Cepheid distances of 29.16 for the inner field and 29.18 for the outer field. These compare well to the H_0 Key Project final value of 29.13 ± 0.11

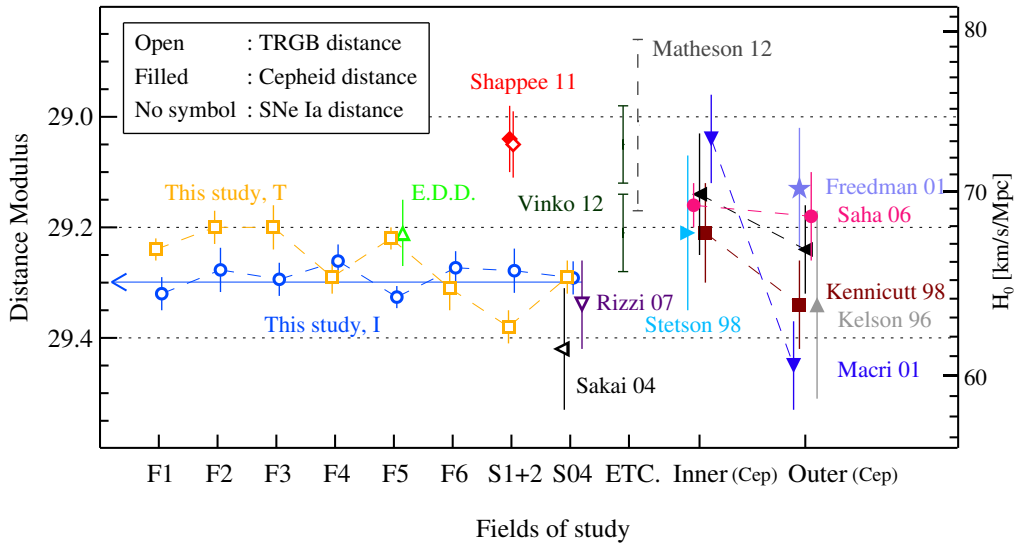

Figure 2.4: Comparison of the distance measurements for M101 based on the TRGB (open symbols), Cepheids (filled symbols), and SN 2011fe (bars without any symbol) versus fields of study: F1-F6 in this study, S1 and 2 in Shappee & Stanek (2011), S04 in Sakai et al. (2004), inner and outer fields for Cepheids, and others. The long horizontal arrow represents the weighted mean value of the TRGB distance estimates derived in this study. The bar at the right end represents the H_0 value depending on the M101 distance, based on the relation in Reindl et al. (2005).

mag (Freedman et al. 2001). Macri et al. (2001) carried out artificial star tests and showed that their NICMOS photometry for the inner field was by ∼0.2 mag affected by blending. Cepheid distance estimates show a large scatter (of ∼ 0.3 mag) even for the outer field where blending effect is less severe, depending on the authors. The distance estimates by Freedman et al. (2001); Sakai et al. (2004); Saha et al. (2006) show a good agreement among them, but they are ∼0.2 mag shorter than those by Kelson et al. (1996); Kennicutt et al. (1998); Macri et al. (2001). The cause for this scatter needs to be investigated.

In contrast, our measurements of the TRGB magnitude for nine fields show a remarkably small dispersion. Note that our measurements show an excellent agreement among independent photometry (for example, between DAOPHOT photometry of ACS images and DOLPHOT photometry of WFPC2 images, among three different sets of HST images (F fields, S1 and S2 fields, and S04 fields), and among all nine fields).

2.4.2 The Absolute Calibration of SNe Ia and the Hubble Constant

We can use the distance measurement for M101 to check the calibration of SN Ia and to derive a value for the Hubble constant. Using two SN Ia optical light curve fitting methods with $BVRI$ photometry of SN 2011fe, Vinko et al. (2012) obtained two estimates for the distance to M101 (assuming $H_0 = 73$ km s^{-1} Mpc $^{-1}$): $(m - M)_0 = 29.21 \pm 0.07$ from the MLCS2k2 method (Jha et al. 2007) and $(m-M)_0 = 29.05 \pm 0.08$ from the SALT2 method (Guy et al. 2007). They concluded that the difference between these two estimates is considered to be due to difference in the zero point calibration of the fiducial SN peak magnitude in the two methods. Our result is closer to the value from the MLCS2k2 method (Jha et al. 2007), indicating that the calibration of the MLCS2k2 method is closer to the TRGB calibration, for the adopted $H_0 = 73$ km s^{-1} Mpc $^{-1}$.

Richmond & Smith (2012) presented optical maximum magnitudes of SN 2011fe: $B_{\rm max} = 10.00 \pm 0.02$, $V_{\rm max} = 9.99 \pm 0.01$, $R_{\rm max} = 9.99 \pm 0.02$ and $I_{\rm max} = 10.21 \pm$

0.03, and derived absolute magnitudes of SN 2011fe adopting a distance modulus of $(m - M)_0 = 29.10 \pm 0.15$. They derived also similar values considering the decline rate of $\Delta m_{15}(B) = 1.21 \pm 0.03$. Adopting our distance measurement, we derive absolute magnitudes of SN 2011fe that are ∼0.2 mag brighter than those in Richmond & Smith (2012): $M_{B,\max} = -19.41 \pm 0.13$, $M_{V,\max} = -19.39 \pm 0.13$, and $M_{R,\max} = -19.38 \pm 0.13$, and $M_{I,\max} = -19.14 \pm 0.13$. ($M_{B,\max} = -19.45 \pm 0.13$, $M_{V,\max} = -19.38 \pm 0.13$, and $M_{R,\max} = -19.39 \pm 0.13$, and $M_{I,\max} = -19.12 \pm 0.13$ after the decline rate correction). The derived value of $M_{V,\max} = -19.38 \pm 0.13$ is between of the values derived from nearby SNe Ia in the previous studies: recent values in Riess et al. (2011) ($M_{V,\max} = -19.15 \pm 0.07$) and old values in Gibson et al (2000) ($M_{V,\max} = -19.46 \pm 0.05$) that are similar to those in Sandage et al. (2006).

Near-infrared (NIR) photometry of SN Ia is potentially a very promising tool for cosmology (Kattner et al. 2012; Barone-Nugent et al. 2012). However, recent calibrations of the NIR absolute magnitudes of SN Ia show large differences (∼ 0.4 mag) (Wood-Vasey et al. 2008; Folatelli et al. 2010; Burns et al. 2011; Mandel et al. 2009, 2011; Kattner et al. 2012), as summarized in Matheson et al. (2012). Our distance measurement for M101 is very useful for calibrating these NIR zero points of the SN Ia templates. Matheson et al. (2012) derived a large range of distance estimates from JHK_S photometry of SN 2011fe: $(m - M)_0 = 28.86$ to 29.17, depending on the adopted calibration. These values are much smaller than our distance measurement.

Matheson et al. (2012) presented JHK_s maximum magnitudes in each band for SN 2011fe: $J_{\max} = 10.51 \pm 0.04$, $H_{\max} = 10.75 \pm 0.04$, and $K_{s,\max} = 10.64 \pm 0.04$, and JHK_s magnitudes at the B-band maximum time for SN 2011fe: $J_{B_{\max}} = 10.62 \pm 0.04$, $H_{B_{\max}} = 10.85 \pm 0.04$, and $K_{s,B_{\max}} = 10.68 \pm 0.05$. ($A_K = 0.01$ is ignored here, as in Matheson et al. (2012) (see their Fig. 3)).

From these values with our distance estimate we derive the NIR absolute magnitudes for SN 2011fe: $M_{J,\max} = -18.79 \pm 0.14$, $M_{H,\max} = -18.55 \pm 0.14$, and

$M_{K_s,\max} = -18.66 \pm 0.13$ ($M_{J,B_{\max}} = -18.68 \pm 0.14$, $M_{H,B_{\max}} = -18.45 \pm 0.14$, and $M_{K_s,B_{\max}} = -18.62 \pm 0.14$ for the B-band maximum time). These values are $\sim$0.2 mag or more brighter than recent calibration of the NIR magnitudes for SN Ia available in the literature (Wood-Vasey et al. 2008; Folatelli et al. 2010; Burns et al. 2011; Mandel et al. 2009, 2011; Kattner et al. 2012).

If we use absolute magnitudes of SN 2011fe derived in this study, we obtain a value for the Hubble constant using the equation $\log H_0 = 0.2M_\lambda(\max) + C_\lambda + 5$ (where $C_B = 0.693 \pm 0.004$, $C_V = 0.688 \pm 0.004$, and $C_I = 0.637 \pm 0.004$) (Reindl et al. 2005), $H_0 = 65.0 \pm 0.5(\text{random}) \pm 5.7(\text{systematic})$ km s^{-1} Mpc^{-1}(we included the internal luminosity dispersion of SNe Ia of 0.14 mag (Tammann & Reindl (2012)) for calculating the systematic error). This value is similar to that given in Tammann & Reindl (2012) based on six SNe Ia including SN 2011fe, $H_0 = 64.0 \pm 1.6 \pm 2.0$ km s^{-1} Mpc^{-1}, but smaller than other recent determinations (Riess et al. 2011; Freedman et al. 2012), $H_0 = 74 \pm 3$ km s^{-1} Mpc^{-1}. This implies three possibilities: (a) that the optical maximum magnitudes of SN 2011fe may be ~ 0.2 mag brighter than typical SNe Ia, (b) that the recent calibration of optical maximum magnitudes of SN Ia may be $\sim$0.2 mag fainter, or (c) that the value for the Hubble constant may be somewhat lower than the values derived recently in other studies.

2.5 Summary

We present a new determination of the distance to M101, host of the Type Ia SN 2011fe, using the tip of the red giant branch method (TRGB) from $F555W$ and $F814W$ images of nine fields within this galaxy in the Hubble Space Telescope archive. Primary results are as follows.

- Color-magnitude diagrams of arm-free regions in all fields show a prominent RGB.
- We measured the I-band magnitudes of the TRGB, obtaining a mean value of $I_{\text{TRGB}} = 25.28 \pm 0.01$ with a standard deviation of only 0.02, using an

edge-detection method. From this we derive a weighted mean value of distance modulus $(m - M)_0 = 29.30 \pm 0.01$(random), corresponding to a linear distance of 7.24 ± 0.03 Mpc. Its systematic error is estimated to be 0.12. Our measurements of the TRGB distances for nine fields show a small dispersion of only 0.02, much smaller than the previous estimates.

- With this distance value we derive the optical and NIR absolute maximum magnitudes of SN 2011fe (at the maximum of each band and at the B-band maximum time). Absolute magnitudes of SN 2011fe are $\sim$0.2 mag brighter in the optical band and much more in the NIR than the recent calibrations of SN Ia in the literature.

- From the optical magnitudes of SN 2011fe and our distance measurement for M101 we obtain a value of the Hubble constant, $H_0 = 65.0 \pm 0.5$(random) $\pm$ 5.7(systematic) km s^{-1} Mpc^{-1}, somewhat smaller than other recent determinations Riess et al. (2011); Freedman et al. (2012). This implies (a) that optical maximum magnitudes of SN 2011fe may be $\sim$0.2 mag brighter than typical SNe Ia, (b) that the recent calibration of optical maximum magnitudes of SN Ia may be ~ 0.2 mag fainter, or (c) that the value for the Hubble constant may be somewhat lower than other recent determinations.

This Chapter has been published in *The Astrophysical Journal* as Lee & Jang 2012, v. 760, p. L14.

Chapter 3

The TRGB Distances to SN Ia Host Galaxies. II. M66 and M96 in the Leo I Group

3.1 Introduction

Type Ia Supernovae (SNe Ia) are a powerful tool to investigate the expansion history of the universe, because their peak luminosity is as bright as a galaxy and is known as an excellent standard candle. Since the discovery of the acceleration of the universe based on the observations of SNe Ia, higher than ever accuracy of their peak luminosity is needed to investigate various problems in cosmology (Freedman & Madore 2010; Riess et al. 2011; Lee & Jang 2012; Tammann & Reindl 2013).

We started a project to improve the accuracy of the calibration of the peak luminosity of SNe Ia by measuring accurate distances to nearby resolved galaxies that host SNe Ia. We derive accurate distances to the SN Ia host galaxies using the method to measure the luminosity of the tip of the red giant branch (TRGB) (Lee et al. 1993). We presented the result of the first target, M101, a well-known spiral galaxy hosting SN 2011fe that is the nearest SN Ia since 1972 (Lee & Jang 2012

(Paper I)). This paper is the second of the series, presenting the results for M66 and M96 in the Leo I Group.

M66 (NGC 3627, SAB(s)b) and M96 (NGC 3368, SAB(rs)ab) are nearby bright spiral galaxies hosting SNe Ia: SN 1989B in M66 (Evans & McNaught 1989; Wells et al. 1994) and SN 1998bu in M96 (Villi et al. 1998; Suntzeff et al. 1999; Jha et al. 1999; Hernandez et al. 2000; Spyromilio et al. 2004). M66 has been host to other three SNe as well: SN II 1973R (Ciatti & Rosino 1977), SN imposter SN 1997bs (Van Dyk et al. 2000), and SN II-L 2009hd (Elias-Rosa et al. 2011).

They are considered to be the members of the compact Leo I Group that includes three subgroups: the Leo Triplet (M66, M65, and NGC 3628), the M96 Group (including M96 (NGC 3368), M95 (NGC 3351), and M105 (NGC 3379)), and the NGC 3607 Group (de Vaucouleurs 1975; Saha et al. 1999). The Leo I Group has played an important role as a stepping stone for calibration of the secondary distance indicators, because it includes both early and late type galaxies at the distance closer than the Virgo cluster and because it hosts SNe Ia. In particular M66 and M96 have been used as important calibrators for the absolute magnitudes of SNe Ia and the Tully-Fisher relation (Saha et al. 1999; Suntzeff et al. 1999; Saha et al. 2006; Jha et al. 2007; Hislop et al. 2011; Tammann & Reindl 2013).

Harris et al. (2007a) derived a value for the distance to the Leo I Group, $(m - M)_0 \approx 30.10 \pm 0.05$ (≈ 10.5 Mpc), from the mean of the known distances to five brightest galaxies in the group (M66, M95, M96, M105, NGC 3351 and NGC 3377). Often the member galaxy candidates without known distances are assumed to be at the same distance, but it is still important to derive a precise distance to each member galaxy candidate for investigating various aspects of the member galaxies.

Unfortunately recent estimates of the distances to M66 and M96 based on resolved stars show a large range (Hislop et al. 2011; Tammann & Reindl 2013). Saha et al. (1999) found 68 Cepheids in M66 from $F555W$ and $F814W$ images obtained with the *Hubble Space Telescope (HST)*/Wide Field Planetary Camera 2 (WFPC2) and derived a distance modulus of $(m - M)_0 = 30.22 \pm 0.12$ from the photometry

of 25 good Cepheids. Later Cepheid estimates range from $(m-M)_0 = 29.70 \pm 0.07$ (Willick & Batra 2001) to 30.50 ± 0.09 (Saha et al. 2006), showing as much as 0.8 mag differences. On the other hand, Mould & Sakai (2009a) presented a distance modulus $(m-M)_0 = 29.82 \pm 0.10$ using the TRGB method from $F555W$ and $F814W$ images obtained with the HST/Advanced Camera for Surveys (ACS) . Furthermore Tully et al. (2009) presented an even smaller TRGB distance estimate, $(m-M)_0 = 29.60 \pm 0.09$. Thus there is a significant difference between the Cepheid distances and TRGB distances as well as among the estimates of each method.

In the case of M96, Tanvir et al. (1995) found 7 Cepheids from HST/WFPC2 $F555W$ and $F814W$ images and derived a distance modulus of $(m-M)_0 = 30.32 \pm 0.16$. Later Cepheid estimates showed a significant spread, ranging from $(m-M)_0 = 29.94 \pm 0.13$ (Willick & Batra 2001) to 30.42 ± 0.15 (Kochanek 1997). Surprisingly Mould & Sakai (2009b) presented a much smaller TRGB distance estimate $(m-M)_0 = 29.65 \pm 0.28$ derived from the HST images. Thus the difference between the Cepheid distances and TRGB distance is as much as 0.3 to 0.7 mag and the range of the Cepheid distances is about 0.4.

In this study we use the well-known TRGB method to estimate the distances to M66 and M96 from the images available in the HST archive. The TRGB method is an efficient and precise primary distance indicator for resolved galaxies so that it is an excellent tool for calibration of more powerful distance indicators such as SN Ia and Tully-Fisher relations (Lee et al. 1993; Sakai et al. 1996; Jang et al. 2012; Tammann & Reindl 2013). Section 2 describes how we derive photometry of the point sources in the images and §3 presents color-magnitude diagrams of the resolved stars in each galaxy, and derive distances to each galaxy using the TRGB method. We discuss implications of our results in §4, and summarizes primary results in the final section.

Table 3.1: A Summary of HST Observations for M66 and M96

Target	R.A. (J2000.0)	Dec (J2000.0)	Instrument	Exposure time $F555W$	Exposure time $F814W$	Prop. ID.
M66	11 20 00.00	12 59 28.0	ACS/WFC	2224 s	8872 s	10433
M96	10 46 32.89	11 48 16.0	ACS/WFC	2280 s	9112 s	10433

3.2 Data Reduction

Table 3.1 lists the information of the HST/ACS images we used for the TRGB analysis in this study: $F555W$ and $F814W$ images of M66 and M96 (Proposal ID: 10433). We made drizzled images for each filter combining the flat fielded images in the HST archive using Tweakreg and AstroDrizzle task in DrizzlePac provided by the Space Telescope Science Institute (http://www.stsci.edu/hst/HST_overview/drizzlepac/). Total exposure times for $F555W$ and $F814W$ are, respectively, 2224 s and 8872 s for M66, and 2280 s and 9112 s for M96. In Figure 3.1 we illustrate the locations of the HST fields in the gray scale maps of i-band Sloan Digital Sky Survey images of M66 and M96. The HST fields cover the west region of each galaxy off from the galaxy center. Two known SNe Ia (SN 1989B and SN 1998bu) are located close to the center of each galaxy and are not covered by these images, as marked in Figure 3.1.

Instrumental magnitudes of point sources in the images were obtained using the DAOPHOT package in IRAF (Stetson 1994), as done for M101 in Lee & Jang (2012). Details are described in Lee & Jang (2012). Mean values for the aperture correction errors are 0.02 mag for both filters. The instrumental magnitudes were converted into the standard Johnson-Cousins VI magnitudes, using the information in Sirianni et al. (2005). The average errors for this transformation are 0.02 mag. We adopted the standard Johnson-Cousins VI magnitudes for transformation to compare our results with others in the literature and combine our results with those for other

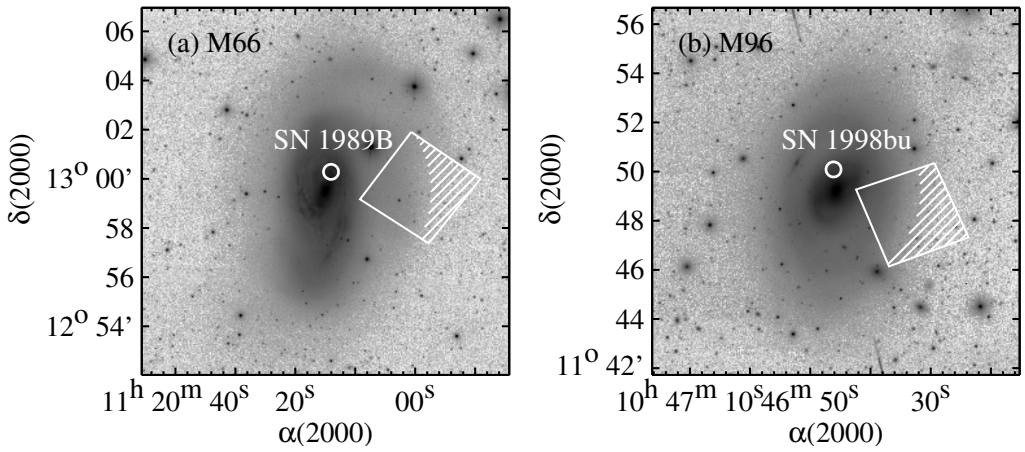

Figure 3.1: Finding charts for the *HST* fields of M66 (a) and M96 (b) (boxes). Gray scale maps represent i-band Sloan digital sky survey images. The hatched regions represent the regions used in the analysis for distance determination. Positions of SN 1989B and SN 1998bu are marked by circles.

galaxies sometimes based on F606W images.

3.3 Results

3.3.1 Photometry of Resolved Stars

The *HST*/ACS fields cover disk regions with spiral arms in each galaxy. We need to select resolved old red giants for the analysis of the TRGB method. Therefore we selected an outer region avoiding arms in each field, as marked by the hatched region in Figure 3.1. Thus chosen regions have the lowest sky background level in the images.

Color-magnitude diagrams (CMDs) of the resolved stars in the selected regions in M66 and M96 are plotted in Figure 3.2. It shows that most of the resolved stars in each galaxy are red giants belonging to the thick slanted feature, which is a red giant branch (RGB). The brightest part of the RGB is seen at $I \approx 26.2$ mag in each galaxy, which corresponds to the TRGB. We adopted the foreground reddening values, $E(B-V) = 0.028$ for M66 and 0.022 for M96 in Schlegel et al. (1998); Schlafly & Finkbeiner (2011). These values yield $A_I = 0.049$ and $E(V-I) = 0.040$ for M66 and $A_I = 0.038$ and $E(V-I) = 0.031$ for M96. We assumed that internal reddening for the old red giants is zero.

3.3.2 TRGB Distance Measurement

We estimated the distances to M66 and M96 from the photometry of the resolved stars using the TRGB method, as described in Lee & Jang (2012). Figure 3.3(a) and (c) plot the I-band luminosity functions of the red giants obtained counting the stars inside the box as marked in Figure 3.2. In Figure 3.3 an abrupt discontinuity is seen at $I \approx 26.2$ mag for each galaxy, which is also noticed in the CMDs. This matches the TRGB in each galaxy.

We performed a quantitative analysis of the TRGB measurement using the edge-detecting algorithm (Sakai et al. 1996; Méndez et al. 2002; Mouhcine et al. 2010). When the I-band luminosity function of the stars is given by $N(I)$ and σ_I is the mean photometric error, $E(I)$ $(= N(I+\sigma_I) - N(I-\sigma_I))$. The values of the TRGB

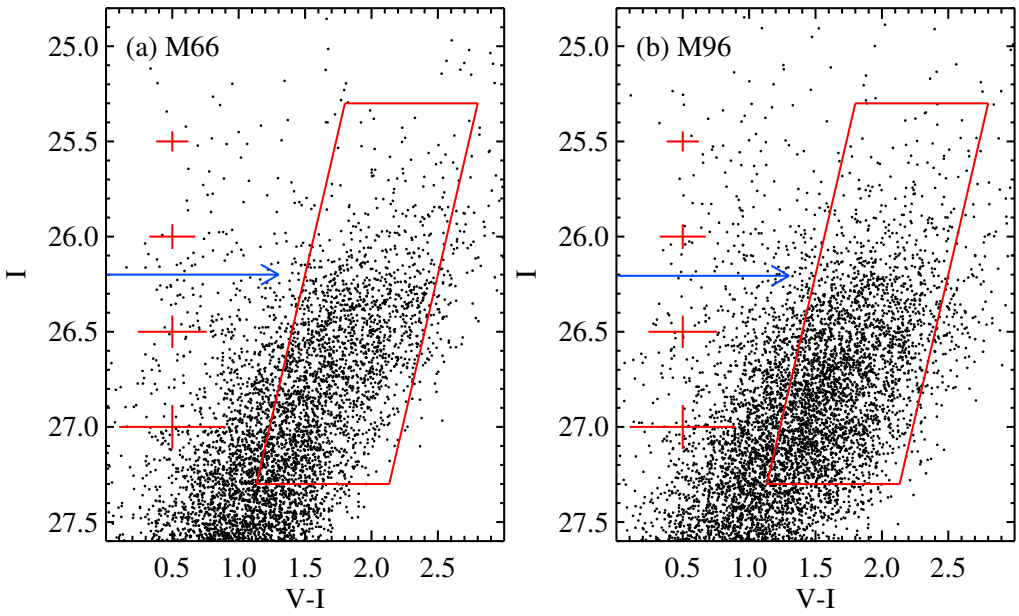

Figure 3.2: $I-(V-I)$ color-magnitude diagrams of the detected stars in the selected regions of M66 (a) and M96 (b). Boxes denote the boundary of the red giants used for distance determination. Arrows indicate the magnitudes of the TRGB. Mean photometric errors for given magnitude bins are plotted by error bars.

magnitudes were determined from the peak values of the edge-detection response function. Figure 3.3(b) and (d) illustrate the edge-detection response functions for M66 and M96, respectively. The edge-detection response function for each galaxy shows a strong peak at the position corresponding to the TRGB. We estimated the measurement errors for the TRGB magnitudes using bootstrap resampling method as described in Lee & Jang (2012). Thus estimated TRGB magnitudes are $I_{\rm TRGB} = 26.20 \pm 0.03$ for M66 and 26.21 ± 0.03 for M96, both of which are almost the same. We obtained a median color value of the TRGB from the color of the brightest part of the RGB: $(V-I)_{\rm TRGB} = 1.97 \pm 0.05$ for M66 and 1.93 ± 0.04 for M96. For calculating distance moduli from apparent TRGB magnitudes we adopted a relation Rizzi et al. (2007) derived: $M_{\rm I,TRGB} = -4.05(\pm 0.02) + 0.217(\pm 0.01)((V-I)_{0,TRGB} - 1.6)$.

After correction for foreground reddening, we derived distance modulus : $(m - M)_0 = 30.12 \pm 0.03$ for M66 and $(m - M)_0 = 30.15 \pm 0.03$ for M96 (where 0.03 is a measurement error). We derived a value of the systematic error to be 0.12, from the combination of the TRGB magnitude error, aperture correction error, and standard transformation error, as described in Lee & Jang (2012). Thus derived distance to these galaxies are $10.57 \pm 0.15 \pm 0.58$ Mpc for M66 and $10.72 \pm 0.15 \pm 0.59$ Mpc for M96. Our distance estimates for M66 and M96 are summarized in Table 3.2.

3.4 Discussion

3.4.1 Comparison with Previous Distance Estimates

There are numerous previous estimates for the distances to M66 and M96 based on various methods (TRGB, Cepheids, Tully-Fisher relations, surface brightness fluctuation (SBF), planetary nebula luminosity functions (PNLFs), and SNe Ia), as listed in Tables 3.3 and 3.3. We compare our estimates for the distances to M66 and M96 with these previous estimates. Figure 3.4 shows a comparison of distance measurements for each galaxy in this study and previous studies. We derived a probability density curve for each measurement with a normalized Gaussian function

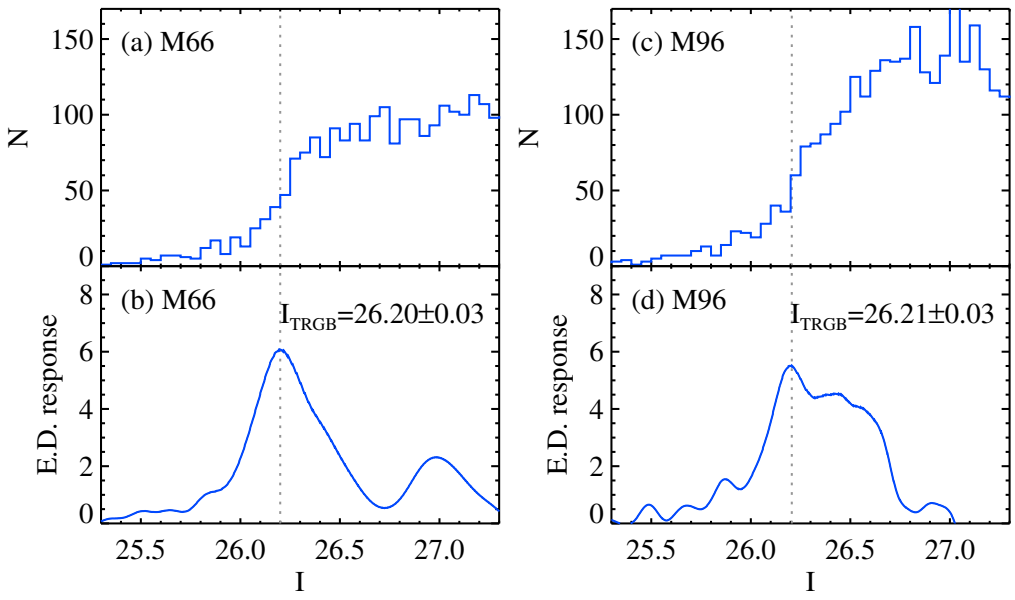

Figure 3.3: (a) and (c) denote I-band luminosity functions of the red giants in the selected regions of M66 and M96, respectively. (b) and (d) plot corresponding edge-detection responses ($E(I)$) for M66 and M96, respectively. Note that (b) and (d) show clearly a dominant single peak for each galaxy at the magnitude corresponding to the TRGB position (dotted lines).

Table 3.2: A Summary of TRGB Distance Measurements for M66 and M96

Parameter	M66	M96
TRGB magnitude, I_{TRGB}	26.20 ± 0.03	26.21 ± 0.03
TRGB color, $(V-I)_{TRGB}$	2.01 ± 0.05	1.96 ± 0.04
Foreground extinction at V, A_V	0.089	0.069
Foreground extinction at I, A_I	0.049	0.038
Foreground reddening, $E(V-I)$	0.040	0.031
Intrinsic TRGB magnitude $I_{0,TRGB}$	26.15 ± 0.03	26.17 ± 0.03
Intrinsic TRGB color, $(V-I)_{0,TRGB}$	1.97 ± 0.05	1.93 ± 0.04
Absolute TRGB magnitude, $M_{I,TRGB}$	-3.97 ± 0.12	-3.98 ± 0.12
Distance modulus, $(m-M)_0$	$30.12 \pm 0.03 \pm 0.12$	$30.15 \pm 0.03 \pm 0.12$
Distance	$10.57 \pm 0.15 \pm 0.58$	$10.72 \pm 0.15 \pm 0.59$

centered at the distance modulus value with a width equal to the measurement error.

Comparison of the TRGB distances derived in this study and previous studies (Mould & Sakai 2009a; Tully et al. 2009) shows significant differences. Our distance estimate for M66 is 0.3 mag larger than that of Mould & Sakai (2009a) ($(m-M)_0 = 29.82 \pm 0.10$) and 0.5 mag larger than that of Tully et al. (2009) ($(m-M)_0 = 29.60 \pm 0.09$). In the case of M96, our distance estimate is 0.5 mag larger than that of Mould & Sakai (2009b) ($(m-M)_0 = 29.65 \pm 0.18$). These differences are explained in terms of the TRGB magnitude differences: the two previous studies derived much brighter magnitudes for the TRGB than this study. Mould & Sakai (2009a) and Tully et al. (2009) presented $I_{\rm TRGB} = 25.83$ and 25.56, respectively, for M66, which are, respectively, 0.37 mag and 0.64 mag brighter than the our value. Similarly Mould & Sakai (2009b) presented $I_{\rm TRGB} = 25.66$ for M96, which is 0.55 mag brighter than our value. What caused these differences is not clear, but the previous measurements might have been affected by younger stars in the disk of each galaxy. Note that we used only the stars in the arm-free regions in each galaxy to reduce the contamination due to younger stars for our analysis.

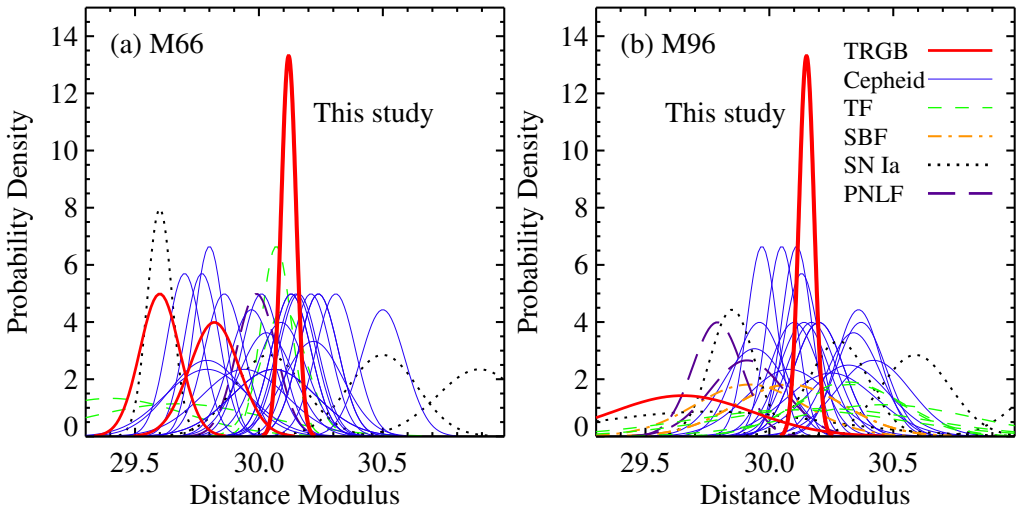

Figure 3.4: Comparison of the distance measurements for M66 (a) and M96 (b) derived in this study and previous studies based on the TRGB (thick solid lines), Cepheids (thin solid lines), Tully-Fisher relations (dashed lines), SBF (dot-dashed lines), SN Ia (dotted lines) and PNLF (long-dashed lines). A probability density curve for each measurement was derived from a Gaussian function centered at the distance modulus value with a width equal to the measurement error.

Our distance estimate is consistent with some of the previous estimates based on other distance indicators (Cepheids, Tully-Fisher relations, SBF, and SN Ia). However, the spread in the previous measurements for each method is significant and the errors for each measurement are mostly larger than ours. It is expected that our results will be useful for improving the calibration of these other distance indicators in the future.

Table 3.3. A List of Distance Measurements for M66

ID	Reference	Method	Distance Modulus	Remarks
1	Pierce (1994)	Tully-Fisher	29.40 ± 0.30	
2	Russell (2002)	Tully-Fisher	30.10 ± 0.09	I band calibration
3		Tully-Fisher	30.07 ± 0.06	B band calibration
4	Tully et al. (2009)[a]	Tully-Fisher	29.67 ± 0.35	
5	Ciardullo et al. (2002)	PNLF[b]	29.99 ± 0.08	N(PNe)=40
6	Mueller & Hoeflich (1994)	SN Ia (Opt)	29.60 ± 0.05	
7	Reindl et al. (2005)	SN Ia (Opt)	30.50 ± 0.14	$H_0 = 60.0$ km s^{-1} Mpc^{-1}
8	Jha et al. (2007)	SN Ia (Opt)	30.04 ± 0.14	$H_0 = 65.0$ km s^{-1} Mpc^{-1}
9	Takanashi et al. (2008)	SN Ia (Opt)	30.89 ± 0.17	$H_0 = 70.8$ km s^{-1} Mpc^{-1}
10	Saha et al. (1999)	Cepheids (LMC)	30.22 ± 0.12	N(Cep)=25, $(m-M)_{0,\mathrm{LMC}} = 18.50$
11	Gibson et al (2000)	Cepheids (LMC)	30.15 ± 0.08	N(Cep)=21, $(m-M)_{0,\mathrm{LMC}} = 18.50$
12		Cepheids (LMC)	30.06 ± 0.17	N(Cep)=17, $(m-M)_{0,\mathrm{LMC}} = 18.50$
13	Freedman et al. (2001)	Cepheids (LMC)	30.01 ± 0.15	N(Cep)=16, $(m-M)_{0,\mathrm{LMC}} = 18.50$
14		Cepheids (LMC)	29.86 ± 0.08	N(Cep)=16, $(m-M)_{0,\mathrm{LMC}} = 18.22$
15		Cepheids (LMC)	29.88 ± 0.08	N(Cep)=35, $(m-M)_{0,\mathrm{LMC}} = 18.50$
16		Cepheids (LMC)	29.71 ± 0.08	N(Cep)=35, $(m-M)_{0,\mathrm{LMC}} = 18.22$
17	Gibson & Stetson (2001)	Cepheids (LMC)	29.94 ± 0.17	N(Cep)=17, $(m-M)_{0,\mathrm{LMC}} = 18.45$
18		Cepheids (LMC)	29.79 ± 0.17	N(Cep)=17, $(m-M)_{0,\mathrm{LMC}} = 18.45$
19	Willick & Batra (2001)	Cepheids (LMC)	29.70 ± 0.07	N(Cep)=36, $(m-M)_{0,\mathrm{LMC}} = 18.50$
20	Dolphin & Kennicutt (2002)	Cepheids (LMC)	30.09 ± 0.10	N(Cep)=28, $(m-M)_{0,\mathrm{LMC}} = 18.50$
21		Cepheids (LMC)	30.03 ± 0.11	N(Cep)=28, $(m-M)_{0,\mathrm{LMC}} = 18.50$
22		Cepheids (LMC)	29.97 ± 0.09	N(Cep)=28, $(m-M)_{0,\mathrm{LMC}} = 18.50$
23	Paturel et al. (2002)	Cepheids (MW)	29.80 ± 0.06	N(Cep)=25
24		Cepheids (MW)	29.77 ± 0.07	N(Cep)=25
25	Kanbur et al. (2003)	Cepheids (MW)	30.31 ± 0.08	N(Cep)=25
26		Cepheids (MW)	30.24 ± 0.08	N(Cep)=25
27		Cepheids (MW)	30.21 ± 0.08	N(Cep)=25
28		Cepheids (LMC)	30.24 ± 0.08	N(Cep)=25, $(m-M)_{0,\mathrm{LMC}} = 18.50$
29		Cepheids (LMC)	30.16 ± 0.08	N(Cep)=25, $(m-M)_{0,\mathrm{LMC}} = 18.50$
30		Cepheids (LMC)	30.13 ± 0.08	N(Cep)=25, $(m-M)_{0,\mathrm{LMC}} = 18.50$
31		Cepheids (LMC)	30.13 ± 0.08	N(Cep)=25, $(m-M)_{0,\mathrm{LMC}} = 18.50$
32	Saha et al. (2006)	Cepheids (LMC)	30.50 ± 0.09	N(Cep)=22, $(m-M)_{0,\mathrm{LMC}} = 18.50$
33	Tully et al. (2009)[a]	TRGB	29.60 ± 0.09	$I_{TRGB} = 25.56, M_{\mathrm{I,TRGB}} = -4.10$
34	Mould & Sakai (2009a)	TRGB	29.82 ± 0.10	$I_{TRGB} = 25.83, M_{\mathrm{I,TRGB}} = -4.05$
35	This study	TRGB	30.12 ± 0.03	$I_{TRGB} = 26.20, M_{\mathrm{I,TRGB}} = -3.97$

[a]The Extragalactic Distance Database (EDD) (Tully et al. 2009).

[b]The Planetary Nebula Luminosity Function (PNLF).

Table 3.4. A List of Distance Measurements for M96

ID	Reference	Method	Distance Modulus	Remarks
1	Russell (2002)	Tully-Fisher	30.32± 0.21	B band calibration
2		Tully-Fisher	30.33± 0.22	I band calibration
3	Springob et al. (2009)	Tully-Fisher	30.10± 0.43	
4		Tully-Fisher	30.21± 0.41	
5	Tully et al. (2009)[a]	Tully-Fisher	30.46± 0.36	
6	Feldmeier et al. (1997)	PNLF[b]	29.91± 0.15	N(PNe)=74
7	Ciardullo et al. (2002)	PNLF[b]	29.79± 0.10	N(PNe)=74
8	Reindl et al. (2005)	SN Ia (Opt)	30.59± 0.14	$H_0 = 60.0$ km s^{-1} Mpc^{-1}
9	Jha et al. (2007)	SN Ia (Opt)	30.28± 0.12	$H_0 = 65.0$ km s^{-1} Mpc^{-1}
10	Takanashi et al. (2008)	SN Ia (Opt)	31.20± 0.17	$H_0 = 70.8$ km s^{-1} Mpc^{-1}
11	Wood-Vasey et al. (2008)	SN Ia (NIR)	29.76± 0.46	$H_0 = 72.0$ km s^{-1} Mpc^{-1}
12	Mandel et al. (2009)	SN Ia (NIR)	29.85± 0.09	$H_0 = 72.0$ km s^{-1} Mpc^{-1}
13	Ajhar et al. (2001)	SBF[c]	30.08± 0.22	
14	Tonry et al. (2001)	SBF[c]	30.08± 0.22	
15	Jensen et al. (2003)	SBF[c]	29.92± 0.22	
16	Tanvir et al. (1995)	Cepheids (LMC)	30.32± 0.16	N(Cep)=7, $(m-M)_{0,\mathrm{LMC}} = 18.50$
17	Kochanek (1997)	Cepheids (LMC)	30.14± 0.10	N(Cep)=7, $(m-M)_{0,\mathrm{LMC}} = 18.50$
18		Cepheids (LMC)	30.42± 0.15	N(Cep)=7, $(m-M)_{0,\mathrm{LMC}} = 18.50$
19	Tanvir et al. (1999)	Cepheids (LMC)	30.13± 0.07	N(Cep)=16, $(m-M)_{0,\mathrm{LMC}} = 18.50$
20		Cepheids (LMC)	30.25± 0.18	N(Cep)=16, $(m-M)_{0,\mathrm{LMC}} = 18.50$
21	Kelson et al. (2000)	Cepheids (LMC)	30.37± 0.10	N(Cep)=7, $(m-M)_{0,\mathrm{LMC}} = 18.50$
22	Gibson et al (2000)	Cepheids (LMC)	30.20± 0.10	N(Cep)=7, $(m-M)_{0,\mathrm{LMC}} = 18.50$
23		Cepheids (LMC)	30.36± 0.09	N(Cep)=7, $(m-M)_{0,\mathrm{LMC}} = 18.50$
24	Willick & Batra (2001)	Cepheids (LMC)	29.94± 0.13	N(Cep)=11, $(m-M)_{0,\mathrm{LMC}} = 18.50$
25	Gibson & Stetson (2001)	Cepheids (LMC)	29.96± 0.10	N(Cep)=7, $(m-M)_{0,\mathrm{LMC}} = 18.50$
26		Cepheids (LMC)	30.10± 0.10	N(Cep)=7, $(m-M)_{0,\mathrm{LMC}} = 18.50$
27	Freedman et al. (2001)	Cepheids (LMC)	29.97± 0.06	N(Cep)=9, $(m-M)_{0,\mathrm{LMC}} = 18.22$
28		Cepheids (LMC)	30.11± 0.06	N(Cep)=9, $(m-M)_{0,\mathrm{LMC}} = 18.50$
29		Cepheids (LMC)	29.95± 0.08	N(Cep)=11, $(m-M)_{0,\mathrm{LMC}} = 18.22$
30		Cepheids (LMC)	30.10± 0.08	N(Cep)=11, $(m-M)_{0,\mathrm{LMC}} = 18.50$
31	Paturel et al. (2002)	Cepheids (MW)	30.05± 0.06	N(Cep)=7
32		Cepheids (MW)	30.17± 0.10	N(Cep)=7
33	Saha et al. (2006)	Cepheids (LMC)	30.34± 0.11	N(Cep)=7, $(m-M)_{0,\mathrm{LMC}} = 18.54$
34	Mould & Sakai (2009b)	TRGB	29.65± 0.28	$I_{TRGB} = 25.66, M_{\mathrm{I,TRGB}} = -4.04$
35	This study	TRGB	30.15± 0.03	$I_{TRGB} = 26.21, M_{\mathrm{I,TRGB}} = -3.98$

[a]The Extragalactic Distance Database (EDD) (Tully et al. 2009).

[b]The Planetary Nebula Luminosity Function (PNLF).

[c]The Surface Brightness Fluxuation (SBF).

3.4.2 The Membership of the Leo I Group

The distance estimates derived in this study show that M66 and M96 are at the same distance and that they are located at the same distance as the mean distance to the Leo I Group (Harris et al. 2007a). These confirm that M66 and M96 are indeed the members of the Leo I Group.

M96 is the brightest member of the Leo I Group. However it is not located at the center of the M96 Group. An E1 galaxy M105 resides at the center of the M96 Group, and M96 is 48′ at the south-west of the group center. M96 has a large pseudo bulge (Nowak et al. 2010), and appears to be connected to a tidal feature extended out from the well-known giant HI ring surrounding a pair of M105 and NGC 3384 (SB0) (Schneider et al. 1983; Schneider 1989). Whether this giant gas ring around M105/NGC 3384 is primordial or formed via collision of disk galaxies (M105/NGC 3384 and M96) has been controversial (Thilker et al. 2009; Michel-Dansac et al. 2010). Precise distance estimates of M96 and M105/NGC 3384 will be useful to investigate the origin of this giant ring, because the relative distances (as well as velocities) are critical constraints for simulation models (Michel-Dansac et al. 2010).

Here we compare the distance to M96 with that of M105. Harris et al. (2007b) estimated the I-band magnitude of the TRGB for M105 to be $I_{TRGB} = 26.10 \pm 0.10$ from the HST/ACS $F606W$ and $F814W$ images of a field 630″ west and 173″ north of the galaxy center, and derived a distance modulus $(m-M)_0 = 30.10 \pm 0.16$ adopting the foreground reddening of $A_I = 0.05 \pm 0.02$ and the absolute TRGB magnitude given in Bellazzini et al. (2004), $M_{I,TRGB} = -4.05 \pm 0.12$. This value is nearly the same as the TRGB distance to M96 derived in this study, showing that M105 and M96 are at the same distance. The radial velocities of M96 and M105 are also very similar (897 ± 4 km s^{-1}and 911 ± 2 km s^{-1}, respectively), while they are $\sim$200 km s^{-1} larger than that of NGC 3384, 704 ± 2 km s^{-1}. These results indicate that the three galaxies (M96, M105, and NGC 3384) are close enough to interact with each other. This supports the collisional scenario that the giant gas ring was formed when M96 collided with NGC 3384/M105 (Michel-Dansac et al. 2010).

3.4.3 The Calibration of the Absolute Magnitudes of SNe Ia and the Hubble Constant

The distances to M66 and M96 derived in this study can be used to improve the calibration of the absolute magnitudes of SNe Ia. Tables 3.5 and 3.6 list, respectively, the V-band maximum magnitudes of SN 1989B and SN 1998bu derived in this study and previous studies (Gibson et al 2000; Sandage et al. 2006; Tammann & Reindl 2013).

Recently Tammann & Reindl (2013) derived $M_{V,\max} = -19.45 \pm 0.15$ for SN 1989B and $M_{V,\max} = -19.38 \pm 0.16$ for SN 1998bu from the photometry in the literature (Suntzeff et al. 1999; Jha et al. 1999; Hernandez et al. 2000; Wells et al. 1994), adopting a mean TRGB distance of the Leo I Group, $(m-M)_0 = 30.39 \pm 0.10$. These values were obtained after correcting for the Galactic extinction, host galaxy extinction, and decline rates (Δm_{15}). These values will become fainter by 0.27 and 0.24 mag if the TRGB distances to M66 and M96 derived in this study are used: $M_{V,\max} = -19.18 \pm 0.11$ for SN 1989B and -19.14 ± 0.12 for SN 1998bu. Other previous estimates (Gibson et al 2000; Sandage et al. 2006) are affected in the similar way, yielding $M_{V,\max} = -19.46 \pm 0.17$ for SN 1989B and -19.38 ± 0.11 for SN 1998bu in Gibson et al (2000), and $M_{V,\max} = -19.17 \pm 0.06$ for SN 1989B and -19.11 ± 0.06 for SN 1998bu in Sandage et al. (2006).

SN 2011fe in M101 is the nearest recent SN Ia with modern photometry so that it is an excellent object for calibration of SNe Ia. Lee & Jang (2012) derived maximum magnitudes of SN 2011fe from the photometry in the literature, adopting a new TRGB distance derived from the weighted mean of nine fields in M101, $M_{V,\max} = -19.38 \pm 0.05(\text{random}) \pm 0.12(\text{systematic})$. Thus V-band magnitudes of SN 1989B and SN 1998bu are ~ 0.2 mag fainter than that of SN 2011fe. This difference is similar to the dispersion of the absolute magnitudes of SNe Ia, 0.14 (Tammann & Reindl 2013). It is noted that the internal extinction for SN 2011fe is known to be negligible, $A_V = 0.04$ (Patat et al. 2011), while those for SN 1989B and 1998bu are not, as listed in Tables 3.7 and 3.8, respectively. The values for A_V derived in

the previous studies range from 0.82 ± 0.08 to 1.33 ± 0.14 for SN 1989B and from 0.74 ± 0.11 to 1.06 ± 0.11 for SN 1998bu (Reindl et al. 2005; Wang et al. 2006; Jha et al. 2007; Tammann & Reindl 2013). Therefore the errors due to internal extinction for SN 1989B and SN 1998bu are expected to be larger than that for SN 2011fe. Further studies to derive better estimates for internal extinction for both SNe are needed in the future.

Near-infrared (NIR) photometry of SN 1998bu in M96 is available in the literature so that SN 1998bu plays as one of the important calibrators for NIR magnitudes of SNe Ia. Tammann & Reindl (2013) derived JHK_s maximum magnitudes at each band of SN 1998bu from the previous photometry (Jha et al. 1999; Suntzeff et al. 1999; Hernandez et al. 2000; Wood-Vasey et al. 2008) : $J = 11.55 \pm 0.03$, $H = 11.59 \pm 0.03$, and $K_s = 11.42 \pm 0.03$. They adopted a value for internal extinction of $A_V = 0.74 \pm 0.11$. Corresponding extinctions in NIR bands are $A_J = 0.19 \pm 0.03$, $A_H = 0.12 \pm 0.02$, and $A_{K_S} = 0.08 \pm 0.01$. If we apply internal extinctions presented above and adopt our new TRGB distance, we obtain NIR absolute magnitudes of SN 1998bu : $M_{J,\max} = -18.79 \pm 0.05$, $M_{H,\max} = -18.68 \pm 0.05$, and $M_{K_s,\max} = -18.81 \pm 0.04$. Lee & Jang (2012) derived JHK_s magnitudes of SN 2011fe in M101 from the photometry in Matheson et al. (2012), adopting a new TRGB distance they derived: $M_{J,\max} = -18.79 \pm 0.04(\text{random}) \pm 0.12(\text{systematic})$, $M_{H,\max} = -18.55 \pm 0.04(\text{random}) \pm 0.12(\text{systematic})$, and $M_{K_s,\max} = -18.66 \pm 0.05(\text{random}) \pm 0.12(\text{systematic})$. Thus absolute J magnitude of SN 1998bu is the same as that of SN 2011fe, while H, K_s magnitudes of SN 1998bu are ~ 0.14 mag brighter than those of SN 2011fe. We derive weighted mean values of SN 1989bu and SN 2011fe from these: $M_{J,\max} = -18.79 \pm 0.03$, $M_{H,\max} = -18.60 \pm 0.03$, and $M_{K_s,\max} = -18.75 \pm 0.03$. It is noted that these values are $0.2 \sim 0.4$ mag brighter than recent calibrations of the NIR magnitudes for SNe Ia available in the literature (Krisciunas et al. 2004; Folatelli et al. 2010; Barone-Nugent et al. 2012; Kattner et al. 2012). Recently several calibrations of the NIR absolute magnitudes of SNe Ia were published, but they show a large spread with ~ 0.2 mag differences (Wood-Vasey et

al. 2008; Folatelli et al. 2010; Burns et al. 2011; Mandel et al. 2011; Kattner et al. 2012; Barone-Nugent et al. 2012; Matheson et al. 2012). Further studies are needed to understand these large differences in the NIR magnitudes of SNe Ia.

The relations between the Hubble constant and the absolute magnitude of SNe Ia are given by $\log H_0 = 0.2M_{V,max} + 5 + (0.688 \pm 0.004)$ in Reindl et al. (2005) or by the equations (2) and (4) in Gibson et al (2000). Using these relations we derive the Hubble constant : $H_0 = 69.1 \pm 3.2$(random) km s^{-1} Mpc^{-1}for SN 1989B, $H_0 = 71.0 \pm 2.6$(random) km s^{-1} Mpc^{-1}for SN 1998bu, and $H_0 = 65.0 \pm 2.1$(random) km s^{-1} Mpc^{-1}for SN 2011fe. A weighted mean of these three measurement is $H_0 = 67.6 \pm 1.5$(random) $\pm$ 3.7(systematic) km s^{-1} Mpc^{-1}. Note that this value for the Hubble constant is similar to the recent estimates based on the cosmic microwave background radiation maps in WMAP9 data, $H_0 = 69.32 \pm 0.80$ km s^{-1} Mpc^{-1}(Bennett et al. 2012) and Planck data $H_0 = 67.3 \pm 1.2$ km s^{-1} Mpc^{-1}(Planck Collaboration et al. 2013), but smaller than other recent determinations based on Cepheid calibration for SNe Ia luminosity, $H_0 = 74 \pm 3$ km s^{-1} Mpc^{-1} (Riess et al. 2011; Freedman et al. 2012) .

Table 3.5: A Summary of Optical Luminosity Calibrations for SN 1989B in M66

ID	References	$(m-M)_0$	V^a_{corr}	M^a_V	H_0 [km/s/Mpc]
(1)	Tammann & Reindl (2013)	30.39 ± 0.10	10.94 ± 0.11	-19.45 ± 0.15	62.8 ± 4.3
(2)	Gibson et al (2000)	30.06 ± 0.17	10.66 ± 0.16^b	-19.40 ± 0.24^b	68.9 ± 7.5
(3)	Sandage et al. (2006)	30.50 ± 0.10	10.95 ± 0.05	-19.55 ± 0.11	60.0 ± 3.1
(4)	This study	30.12 ± 0.03	Tammann & Reindl (2013)	-19.18 ± 0.11	71.1 ± 3.8
(5)	This study	30.12 ± 0.03	Gibson et al (2000)	-19.46 ± 0.17^b	67.1 ± 5.2
(6)	This study	30.12 ± 0.03	Sandage et al. (2006)	-19.17 ± 0.06	71.4 ± 2.0
(7)	This study	30.12 ± 0.03	Straight mean of (4) and (5)		69.1 ± 3.2
(8)	This study	30.12 ± 0.03	Weighted mean of (4) and (5)		69.7 ± 3.1

[a] Corrected for the Galactic extinction, host galaxy extinction and decline rate (Δm_{15}).

[b] We applied decline rate (Δm_{15}) correction using equation (21) of Phillips et al. (1999).

Table 3.6: A Summary of Optical Luminosity Calibrations for SN 1998bu in M96

ID	References	$(m-M)_0$	V_{corr} [a]	M_V [a]	H_0 [km/s/Mpc]
(1)	Tammann & Reindl (2013)	30.39 ± 0.10	11.01 ± 0.12	-19.38 ± 0.16	64.9 ± 4.7
(2)	Gibson et al (2000)	30.20 ± 0.10	10.77 ± 0.11 [b]	-19.43 ± 0.15 [b]	68.0 ± 4.7
(3)	Sandage et al. (2006)	30.34 ± 0.11	11.04 ± 0.05	-19.30 ± 0.12	67.3 ± 3.8
(4)	This study	30.15 ± 0.03	Tammann & Reindl (2013)	-19.14 ± 0.12	72.4 ± 3.9
(5)	This study	30.15 ± 0.03	Gibson et al (2000)	-19.38 ± 0.11 [b]	69.6 ± 3.6
(6)	This study	30.15 ± 0.03	Sandage et al. (2006)	-19.11 ± 0.06	73.5 ± 2.1
(7)	This study	30.15 ± 0.03	Straight mean of (4) and (5)		71.0 ± 2.6
(8)	This study	30.15 ± 0.03	Weighted mean of (4) and (5)		70.9 ± 2.6

[a] Same as Table 3.5.

[b] Same as Table 3.5.

Table 3.7: A Summary of Internal Extinction Values for SN 1989B in M66

References	$E(B-V)$	A_V	R_V	Remarks
Suntzeff et al. (1999)	0.37 ± 0.03	1.15 ± 0.09	3.1	BVI
Jha et al. (2007)	0.47 ± 0.07	1.33 ± 0.14	2.86 ± 0.29	$UBVRI$
Wang et al. (2006)	0.42 ± 0.06	0.97 ± 0.14	2.30 ± 0.11	$UBVI$
Reindl et al. (2005) & Tammann & Reindl (2013)	0.31 ± 0.03	0.82 ± 0.08	2.65 ± 0.15	BVI

Table 3.8: A Summary of Internal Extinction Values for SN 1998bu in M96

References	$E(B-V)$	A_V	R_V	Remarks
Suntzeff et al. (1999)	0.34 ± 0.03	1.05 ± 0.09	3.1	BVI
Jha et al. (2007)	0.34 ± 0.05	1.06 ± 0.11	3.13 ± 0.36	$UBVRI$
Wang et al. (2006)	0.36 ± 0.04	0.83 ± 0.10	2.30 ± 0.11	$UBVI$
Reindl et al. (2005) & Tammann & Reindl (2013)	0.28 ± 0.04	0.74 ± 0.11	2.65 ± 0.15	BVI

3.5 Summary

We present VI photometry of the resolved stars in two spiral galaxies M66 and M96 that host SNe Ia in the Leo I Group, derived from HST/ACS $F555W$ and $F814W$ images. Then we estimate the distances to these two galaxies applying the TRGB method to this photometry. We summarize main results in the following.

- Most of the resolved stars in the selected regions of M66 and M96 are red giants, allowing us to determine the distances to these galaxies.

- The I-band magnitudes of the TRGB are found to be $I_{\rm TRGB} = 26.20 \pm 0.03$ for M66 and 26.21 ± 0.03 for M96. These TRGB magnitudes yield distance modulus $(m - M)_0 = 30.12 \pm 0.03$(random) $\pm$ 0.12(systematic) for M66 and $(m - M)_0 = 30.15 \pm 0.03$(random) $\pm$ 0.12(systematic) for M96. This result shows that M66 and M96 are the members of the same group.

- The absolute maximum magnitudes of the SNe Ia are derived from the previous photometry and the distance measurement in this study, as listed in Tables 3.5 and 3.6. Similarly we derive NIR magnitudes for SN 1998bu: $M_{J,\rm max} = -18.79 \pm 0.05$, $M_{H,\rm max} = -18.68 \pm 0.05$, and $M_{K_s,\rm max} = -18.81 \pm 0.04$.

- Combining the results for SN 1989B and SN 1998bu with those for SN 2011fe in M101 based on the same method given in Lee & Jang (2012), we obtain an estimate of the Hubble constant, $H_0 = 67.6 \pm 1.5 \pm 3.7$ km s^{-1} Mpc^{-1}.

This Chapter has been published in *The Astrophysical Journal* as Lee & Jang 2013, v. 773, p. 13.

Chapter 4

The TRGB Distances to SN Ia Host Galaxies. III. NGC 4038/39 and NGC 5584

4.1 Introduction

Type Ia supernovae (SNe Ia) are one of the most powerful distance indicators for distant galaxies in the cosmic expansion dominated field ($d \gtrsim 100$ Mpc). Three advantages of SNe Ia - a bright peak luminosity, a small luminosity dispersion, and a homogeneity in the universe - have enabled us to investigate the cosmic expansion rate (H_0) (Freedman et al. 2001, 2012; Sandage et al. 2006; Riess et al. 2011) and the cosmic acceleration rate (Λ) (Riess et al. 1998; Perlmutter et al. 1999). Although great progress has been made over the last two decades, more accurate calibration of peak luminosity of SNe Ia is needed to derive more accurate values of cosmological parameters.

Recently, two large projects, Supernovae and H_0 for the Equation of State (SH0ES, (Riess et al. 2011)) and Carnegie Hubble Program (CHP, (Freedman et al. 2012)), have been working on the calibration of SNe Ia to improve the mea-

surement of cosmological parameters. They performed the luminosity calibration of SNe Ia based on the Cepheid distance estimates of 8 SNe Ia host galaxies and derived similar values of the Hubble constant: 74.8 ± 3.1 km s^{-1} Mpc^{-1}(Riess et al. 2011) and 74.3 ± 2.1 km s^{-1} Mpc^{-1} (Freedman et al. 2012).

However, these values of the Hubble constant are somewhat larger than those based on recent analysis of the cosmic microwave background radiation (CMBR). Bennett et al. (2013) derived the cosmological parameters from the analysis of the angular power spectrum of CMBR in WMAP9 assuming a flat ΛCDM cosmology, and presented $H_0 = 69.32 \pm 0.80$ km s^{-1} Mpc^{-1}. Later, the Planck Collaboration lead to an even smaller value of the Hubble constant, $H_0 = 67.8 \pm 0.9$ km s^{-1} Mpc^{-1}, using new CMBR data from the Planck satellite (Planck Collaboration et al. 2014, 2015). Thus the traditional distance ladder method and the CMBR analysis based on ΛCDM cosmology show a 2–3σ level of difference in the estimates of the Hubble constant (Bennett et al. 2014). This is called "the Hubble tension", one of the most critical issues in modern cosmology. In addition, recent studies of the baryon acoustic oscillation (BAO) in the range of redshift combined with SNe Ia data presented similar values to those from the CMBR analysis (Aubourg et al. 2014).

We have been working on the luminosity calibration of SN Ia by measuring the precise distances to SN Ia host galaxies based on the Tip of the Red Giant Branch (TRGB) (Lee et al. 1993). The TRGB method uses old red giant branch (RGB) stars, classified as population II. The metallicity dependence of I-band luminosities of TRGB stars is known to be small (Lee et al. 1993; Bellazzini et al. 2001; Rizzi et al. 2007; Madore et al. 2009; Salaris & Cassisi 1997). Moreover, the TRGB method often uses RGB stars located in the halo, where the internal extinction is expected to be negligible and the crowing of stars is much less than the disk or the bulge. Lee & Jang (2012) (Paper I) measured the TRGB distance to M101 hosting SN 2011fe, which is the nearest SN Ia with modern CCD photometry. Lee & Jang (2013) (Paper II) determined the TRGB distances to M66 and M96 in the Leo I Group, hosting SN

1989B and SN 1998bu. By combining the TRGB distance estimates of three SNe Ia from Papers I and II, and optical light curves for three SNe Ia, we derived the Hubble constant, $H_0 = 68.4 \pm 2.6$(random)$\pm$3.7(systematic) km s^{-1} Mpc^{-1} (Lee & Jang 2013), which is slightly smaller than values from the Cepheid calibrated SNe Ia (Riess et al. 2011; Freedman et al. 2012).

In this paper, we present the TRGB distances to two additional SN Ia host galaxies, NGC 4038/39 hosting SN 2007sr and NGC 5584 hosting SN 2007af. NGC 4038/39 are a well known pair of galaxies showing early stage merger of disk galaxies. In 2007, a supernova was discovered near the southern tidal tail of this galaxy, SN 2007sr (Drake et al. 2007). Spectroscopic observations confirmed that it is a SN Ia (Naito et al. 2007; Umbriaco et al. 2007). Photometric follow-up observations were made from optical to near-infrared (Schweizer et al. 2008; Hicken et al. 2009). Light curve fits on this SN suggested that its internal reddening is expected to be small, $A_V \sim 0.2$ (Schweizer et al. 2008; Phillips et al. 2013).

There are three distance estimates to NGC 4038/39 based on the TRGB in the literature. Saviane et al. (2004) analysed Hubble Space Telescope (HST)/Wide Field Planetary Camera 2 ($WFPC2$) images of a field on the southern tidal tail and derived a TRGB distance, $(m - M)_0 = 30.70 \pm 0.25$ ($d = 13.8 \pm 1.7$ Mpc). This value is significantly smaller than previous estimates based on radial velocities of NGC 4038/39 ($d \sim 20$ Mpc ($V_{Local\ Group} \sim 1400\ km\ s^{-1}$, assuming $H_0 \sim 70$ km s^{-1} Mpc^{-1})). Later, Saviane et al. (2004) presented a similar distance estimate, $(m-M)_0 = 30.62\pm0.17$ ($d = 13.3\pm1.0$ Mpc), using the new HST/Advanced Camera for Surveys (ACS) image data (Saviane et al. 2008). However, Schweizer et al. (2008) presented a significantly larger value, $(m-M)_0 = 31.51\pm0.17$ ($d = 20.0\pm1.6$ Mpc), based on the same ACS image data used in Saviane et al. (2008). On the other hand, Riess et al. (2011) detected Cepheid variables in the main bodies of NGC 4038/39 and derived a distance modulus, $(m - M)_0 = 31.66 \pm 0.08$ ($d = 21.5 \pm 0.6$ Mpc). This is similar to the value in Schweizer et al. (2008), but much larger than the value given by Saviane et al. (2008).

NGC 5584 is a moderately inclined ($\theta = 42.4°$) spiral galaxy hosting SN 2007af, which is one of the most well monitored SNe Ia. Before its pre-maximum, spectroscopic and photometric observations from optical to near infrared have been made (Hamuy et al. 2006; Hicken et al. 2009). Moreover the internal reddening for SN 2007af is known to be small, $A_V = 0.39 \pm 0.06$ (Simon et al. 2007). Thus, SN 2007af is an ideal target for the luminosity calibration of SNe Ia. Previous distance estimates based on the Tully-Fisher relation show a wide range of values with large uncertainty: $(m-M)_0 = 31.12 \sim 31.59$ with uncertainties of ~ 0.4 (Theureau et al. 2007; Springob et al. 2009; Sorce et al. 2012). Riess et al. (2011) detected 94 Cepheid variables based on the optical/near-infrared image data taken with HST/WFC3, and derived a distance, $(m-M)_0 = 31.72 \pm 0.07$ ($d = 22.1 \pm 0.7$ Mpc). This value is much larger than those based on the Tully-Fisher relations. To date, there is no TRGB distance estimate for NGC 5584.

This paper is composed as follows. Section 2 describes data reduction. Section 3 presents color-magnitude diagrams and distance estimates for each galaxy. Implications of our results are discussed in Section 4.

4.2 Data and Data Reduction

The image data for NGC 4038/39 and NGC 5584 were acquired from the HST archive. Table 4.1 lists the information for the HST image data used in this study. The image data for NGC 4038/39 covering the southern tidal tail, as shown in Figure 4.1 (a), were taken with the ACS in Wide Field Channel (WFC) mode (Proposal ID: 10580) with exposure times of $4 \times \sim 2700$s for $F606W$ and $3 \times \sim 2700$s for $F814W$. Corresponding total exposure times were 10870s and 8136s for $F606W$ and $F814W$, respectively. Charge transfer efficiency (CTE) corrected and flat fielded images (indicated by suffix _flc.fits) were combined to make a single drizzled image using the DrizzlePac[1]. Because individual _flc images were severely contaminated

[1] http://drizzlepac.stsci.edu/

Table 4.1. A Summary of *HST* Observations of NGC 4038/39 and NGC 5584

	NGC 4038/39	NGC 5584
R.A.(2000)	$12^h01^m27.^s45$	$14^h22^m23.^s62$
Dec(2000)	$-18°59'28.''7$	$-00°23'12.''7$
Prop ID.	10580	11570
Detector	ACS/WFC	WFC3/UVIS
Exposure, V	10,870s, $F606W$	45,540s, $F555W$
Exposure, I	8,136s, $F814W$	14,400s, $F814W$

by cosmic rays, the automatic image aligning tool, TweakReg task, failed to provide fine solutions. Thus, we used an alternative strategy, as described in the following.

First, we performed an aperture photometry on the _flc images with aperture radii of $0.''040$ and $0.''125$ using DAOPHOT in the IRAF package. The magnitude difference between these two aperture radii is defined as the concentration index, C. Next, sources with $0.9 < C \leq 1.6$ were selected. Through this process, sources with abnormally narrow (e.g., cosmic rays) or abnormally broad (e.g., background galaxies) radial profiles were rejected. Second, we converted image coordinates for the selected sources to the World Coordinate System (WCS) based on the information listed in the header. The WCS coordinates for a pair of _flc images were matched with a matching criteria of $0.''05$ (1 pixel). This process rejects most non-stellar objects such as cosmic rays and hot pixels. Finally, the files to be used with the TweakReg task were created. These files contain source coordinates and flux counts. Using these files, the TweakReg task output better solutions of ΔX and ΔY with a rms value of ~ 0.06 pixel ($0.''003$).

The aligned images were combined into a single drizzled images using the AstroDrizzle task. The final_pixfrac and final_scale values used are 1.0 and $0.''04$/pixel,

respectively. Output images show FWHM of 2.64 pixels ($0\farcs106$) for $F606W$ and 2.38 pixels ($0\farcs095$) for $F814W$.

Observations for NGC 5584 were done with the Wide Field Camera 3 (WFC3) in Ultraviolet-Visible (UVIS) mode with the primary aim of detecting Cepheid variables (Proposal ID : 11570). Centered on NGC 5584, the $2\farcm7 \times 2\farcm7$ field covering the main body and inner halo of the galaxy, as shown in Figure 4.1 (b), was observed with exposure times of $76 \times \sim 600$s for $F555W$ and $24 \times \sim 600$s for $F814W$. Total exposure times are 45,540s and 14,400s for $F555W$ and $F814W$, respectively. The _flc images were made from the flat-fielded images (indicated by suffix _flt.fits) and the raw images (indicated by suffix _raw.fits) by applying pixel-based CTE correction software[2]. Derived _flc images were aligned in the same way as was done for NGC 4038/39 images. Mean rms values for ΔX and ΔY from the TweakReg task are ~ 0.08 pixels ($\sim 0\farcs0032$) for both filters. Aligned _flc images were then combined using the AstroDrizzle task with a final_pixfrac value of 0.7 and a final_scale value of $0\farcs025$/pixel. RMS values of weight images for each filter are smaller than 4% of the median value. FWHMs for point sources in the final drizzled images are 3.00 pixels ($0\farcs075$) for $F555W$ and 3.22 pixels ($0\farcs081$) for $F814W$. Figure 4.2 shows $5'' \times 5''$ sections of the output $F814W$ images of NGC 4038/39 (a) and of NGC 5584 (b). Point sources and extended sources (mostly background galaxy) can be clearly seen in the images.

PSF photometry was done on the drizzled images using the standard routine : Daofind, Phot, and Allstar tasks in IRAF/DAOPHOT (Stetson 1987). Initial aperture photometry with aperture radii of $0\farcs040$ and $0\farcs125$ were done to derive the concentration index for each stellar object. With this combination of aperture radii, point sources show mean concentration index values of $C = 1.25$ for NGC 4038/39 and $C = 1.05$ for NGC 5584. PSF images were constructed for each galaxy based on ~ 50 bright, isolated, and $C \sim 1.25$ or 1.05 stellar objects. Source coordinates to be used in the photometry were determined from $F814W$-band images for each

[2]http://www.stsci.edu/hst/wfc3/ins_performance/CTE/

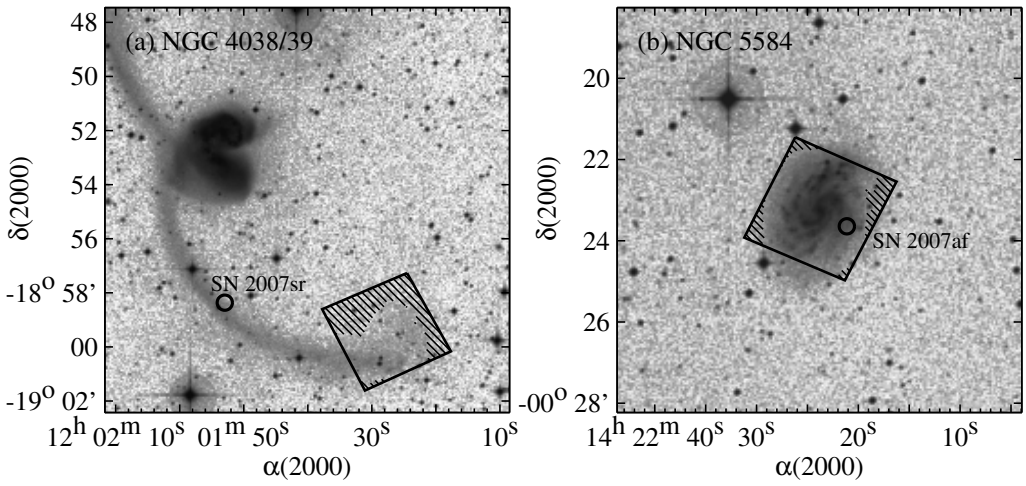

Figure 4.1: Identification of *HST* fields for NGC 4038/39 (a) and NGC 5584 (b) overlaid on grey scale maps of the Digitized Sky Survey images. Only resolved stars in the hatched region of each field were used in the analysis. Locations of known SNe Ia are marked by open circles.

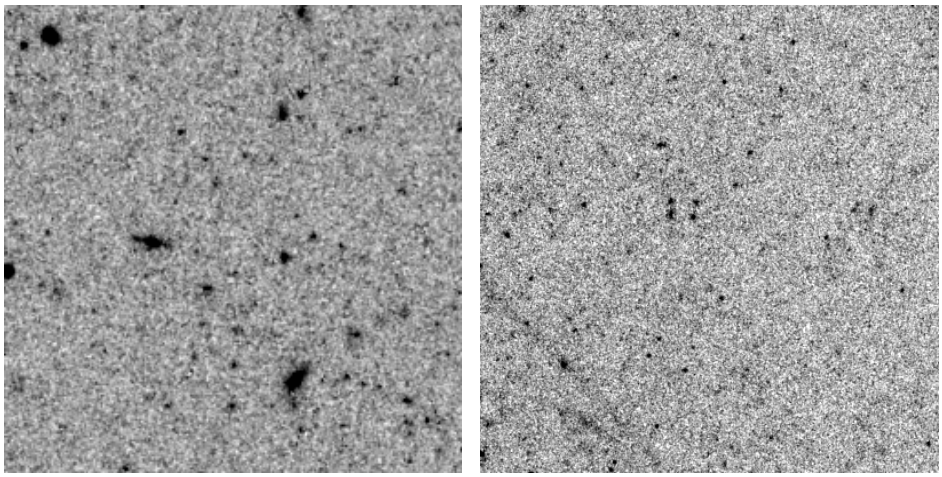

Figure 4.2: $5'' \times 5''$ sections of reconstructed $F814W$ images for NGC 4038/39 (left) and NGC 5584 (right). The pixel scales of each image are $0\overset{''}{.}04$ and $0\overset{''}{.}025$, respectively. Both images clearly show point-like and extended sources.

galaxy with a detection threshold of 2. We used revised photometric zeropoints for ACS/WFC (26.416 for $F606W$ and 25.529 for $F814W$) and WFC3/UVIS (25.81 for $F555W$ and 24.67 for $F814W$), provided by STScI [3][4]. Aperture correction values to the aperture radii of $0\farcs5$ (for ACS/WFC) or $0\farcs4$ (for WFC3/UVIS) were calculated by checking the curve of growth for bright isolated stars. Derived values are -0.162, -0.157 for $F606W$, $F814W$ on ACS/WFC and -0.139, -0.229 for $F555W$, $F814W$ on WFC3/UVIS with an uncertainty of 0.02. Additional aperture corrections up to the infinite aperture radius were also applied. Corresponding values derived from the enclosed energy curves provided by STScI[5] [6] are : $-0.095, -0.098$ for $F606W$, $F814W$ on ACS/WFC and $-0.102, -0.107$ for $F555W$, $F814W$ on WFC3/UVIS, respectively. Finally, ACS magnitudes were converted to standard Johnson-Cousins magnitudes using the photometric transformation equations listed in Sirianni et al. (2005).

4.2.1 Photometric Transformations

The photometric systems for ACS/WFC and WFC3/UVIS are not the same. There is no TRGB calibration for the WFC3/UVIS system yet. To apply the TRGB calibration, and to facilitate comparisons of the two galaxies in this study and those in our previous studies (Lee & Jang (2012, 2013)), we derived photometric transformations from the WFC3/UVIS system to the ACS/WFC system as follows. We used archival image data for two Milky Way globular clusters, NGC 2419 and 47 Tuc, which were observed using both ACS/WFC and WFC3/UVIS, as listed in Table 4.2 and shown in Figure 4.3. These two globular clusters have been used for the photometric transformation from the ACS/WFC system to the Johnson-Cousin system in Sirianni et al. (2005), Harris et al. (2007a), and Saha et al. (2011). We calibrated raw image data to construct CTE corrected drizzled images and carried

[3]http://www.stsci.edu/hst/acs/analysis/zeropoints/zpt.py
[4]http://www.stsci.edu/hst/wfc3/phot_zp_lbn
[5]http://www.stsci.edu/hst/acs/analysis/apcorr
[6]http://www.stsci.edu/hst/wfc3/uvis_ee_model_smov.dat

Table 4.2. A Summary of *HST* Observations of NGC 2419 and 47 Tuc from the Archive

	NGC 2419		47 Tuc	
	ACS/WFC	WFC3/UVIS	ACS/WFC	WFC3/UVIS
R.A.(2000)	$07^h38^m08.^s27$	$07^h38^m08.^s54$	$00^h22^m38.^s52$	$00^h22^m35.^s92$
Dec(2000)	$38°51'36.''3$	$38°52'40.''6$	$-72°04'01.''1$	$-72°04'05.''3$
Prop ID.	9666	11903	10048, 11677	11903, 11452
Exposure, $F555W$	720s	1,160s	2,139s	1,160s
Exposure, F606W	676s	800s	163,676s	18,376s
Exposure, $F814W$	676s	1,300s	184,242s	3,400s

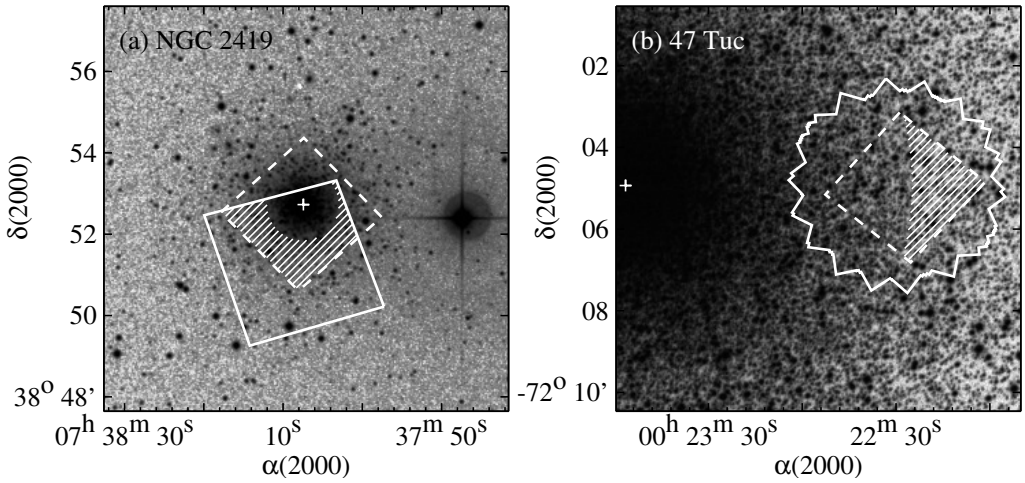

Figure 4.3: Finding charts for ACS/WFC fields (solid square in (a) and polygon in (b)) and WFC3/UVIS fields (dashed-line squares) of NGC 2419 (a) and 47 Tuc (b) overlaid on Digitized Sky Survey images. The center of each star cluster is indicated by a white cross. Only point sources in the hatched region of each cluster ($R > 1'$ for NGC 2419 and $R > 7'$ for 47 Tuc) were used for the photometric transformation.

out PSF photometry as described in Section 2. We then matched the photometric catalogues from ACS/WFC and WFC3/UVIS image data.

Constructed color-magnitude diagrams (CMDs) for resolved stars in NGC 2419 and 47 Tuc are shown in Figure 4.4. To reduce the uncertainty due to the stars in the crowded field, we used only the stars located in relatively low density environments at $R_{NGC2419} \geq 1'$ and $R_{47Tuc} \geq 7'$, indicated by the hatched lines in Figure 4.3. CMDs from ACS/WFC data (open squares) and WFC3/UVIS data (filled squares) look very similar. Stars with $F555W - F814W \gtrsim 0.8$, WFC3/UVIS data show in general redder colors than ACS/WFC data. For blue stars with $F555W - F814W \sim 0.0$, however, WFC3/UVIS data shows slightly bluer color than ACS/WFC data. This trend is seen in both globular clusters. In order to compare the difference quantitatively, we selected bright and non-saturated stars in the shaded regions ($18.5 < F814W_{ACS} < 21.0$ for NGC 2419, and $19.0 < F814W_{ACS} < 21.5$ or $19.5 < F814W_{ACS} < 22.5$ for 47 Tuc) of Figure 4.4 and compared them in Figure 4.5.

Figure 4.5 shows comparisons of magnitudes between the two photometric systems in terms of their colors. $F555W_{ACS} - F814W_{ACS}$ colors range from 0.0 to 2.2, and their mean offsets are ~ -0.04 for $F555W$ and ~ 0.01 for $F814W$. We plot isochrones, as a reference, for the 12 Gyr age and $[Fe/H] = -1.4$, which is a mean metallicity of NGC 2419 and 47 Tuc, provided by Dartmouth group (Dotter et al. 2008). Data points and stellar isochrones are in good agreement, mean offsets are estimated to be ~ 0.01 in both filters. We derive a photometric transformation as follows :

$$F555W_{ACS} = F555W_{WFC3} - (0.0137 \pm 0.0044) - (0.0178 \pm 0.0030)(Color),$$

and

$$F814W_{ACS} = F814W_{WFC3} + (0.0145 \pm 0.0036) - (0.0053 \pm 0.0024)(Color)$$

where $Color = F555W_{ACS} - F814W_{ACS}$.

Note that the amount of correction is very small: 0.05 mag in $F555W$ and smaller than 0.01 mag in $F814W$ for $Color \sim 2.0$.

We applied this photometric transformation to the photometry of NGC 5584. Transformation uncertainties are estimated to be ~ 0.01 mag considering uncertainties of aperture corrections, although the fitting uncertainties are much smaller than 0.01 mag.

We derived the same photometric transformation for $F606W$-band for the future studies.

$F606W_{ACS} = F606W_{WFC3} + (0.0016 \pm 0.0021) - (0.0322 \pm 0.0019)(Color)$,
and
$F814W_{ACS} = F814W_{WFC3} + (0.0156 \pm 0.0023) - (0.0060 \pm 0.0020)(Color)$
where $Color = F606W_{ACS} - F814W_{ACS}$.

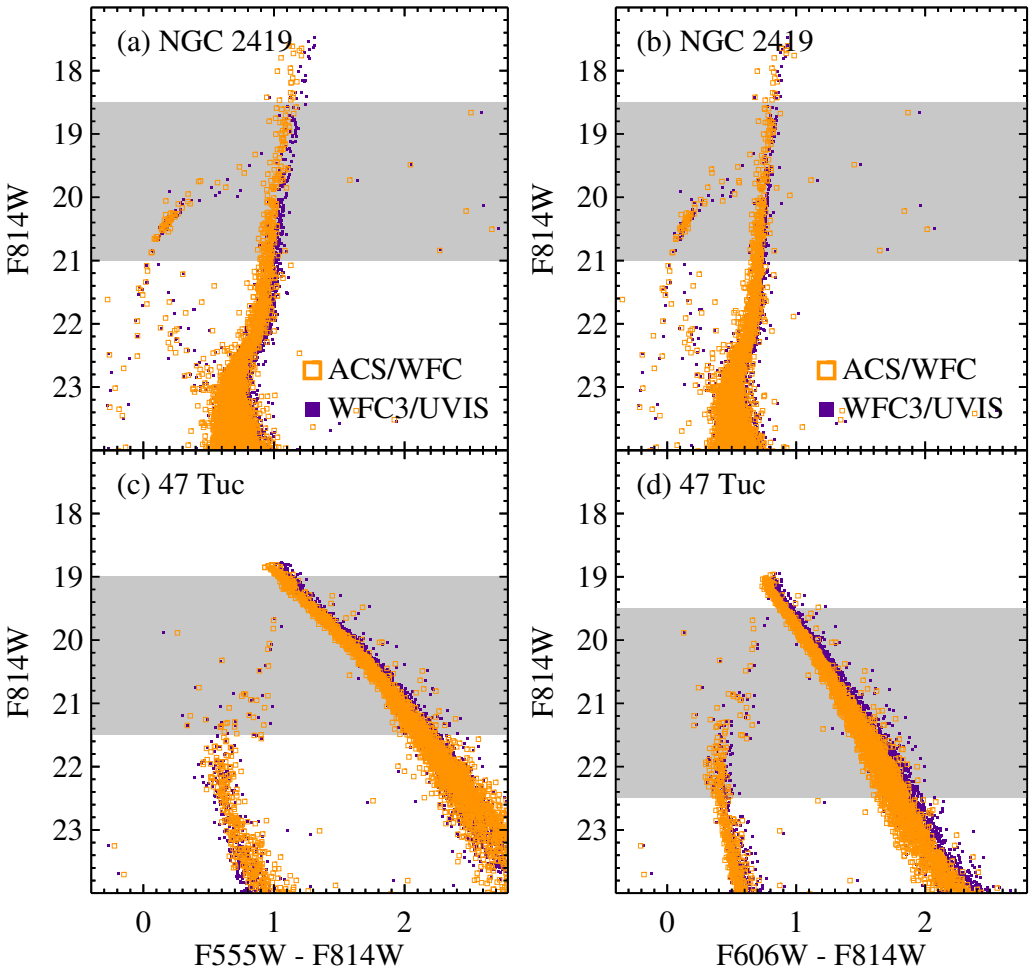

Figure 4.4: Color magnitude diagrams of resolved stars in NGC 2419 (a and b) and 47 Tuc (c and d). Open and filled squares indicate the photometric data from the ACS/WFC and the WFC3/UVIS, respectively. We used bright and non-saturated stars, which are located in the shaded boxes in each panel, for the photometric transformation.

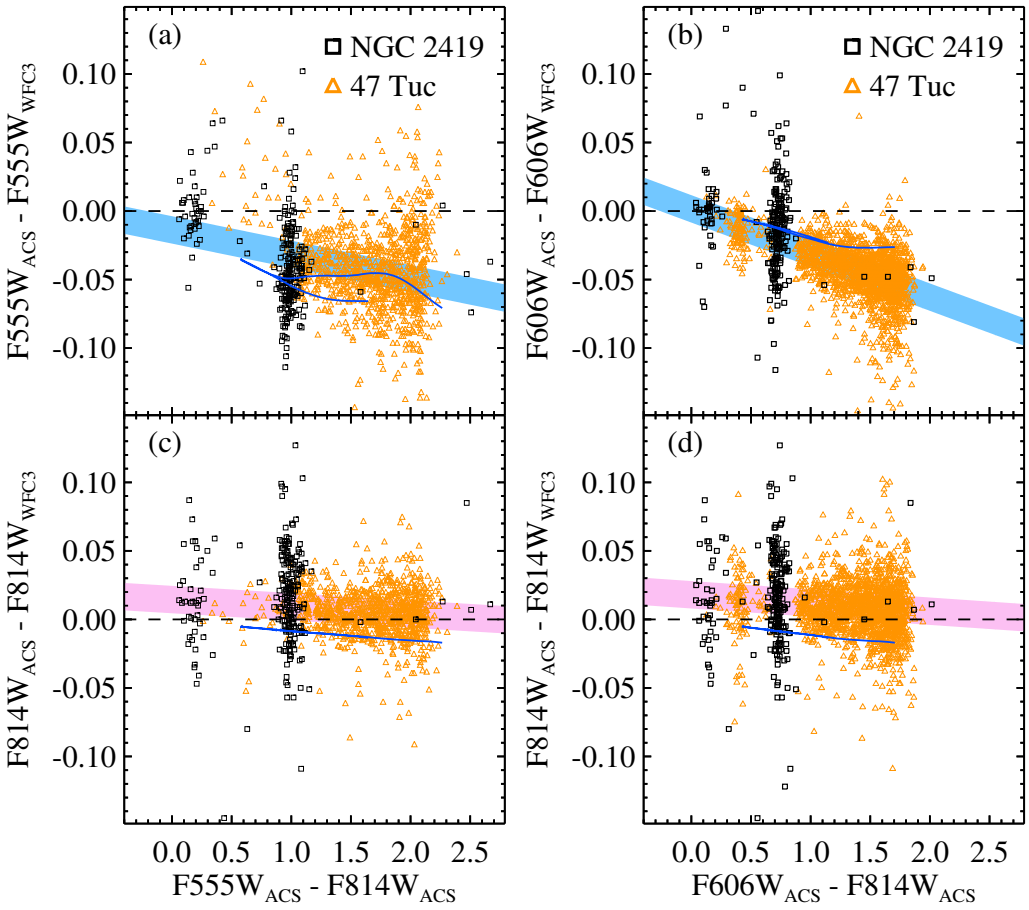

Figure 4.5: ((a) and (c)) Comparison of photometric systems between ACS/WFC and WFC3/UVIS for $F555W$-band, and $F814W$-band in terms of $F555W-F814W$ color in the ACS/WFC system. ((b) and (d)) Same as (a) and (c) but for the (F606W)-band. Open squares and open triangles denote detected stars in NGC 2419 and 47 Tuc, respectively. Solid lines in each panel indicate the stellar isochrones for age=12 Gyr and [Fe/H]= -1.4, which is the mean metallicity of two globular clusters, provided by the Dartmouth group (Dotter et al. 2008). Shaded regions indicate the 1σ uncertainty area of the photometric transformation.

4.2.2 Artificial star test

We checked the photometric completeness and systematic errors of our photometry through the artificial star experiment. To do this, we selected test fields with a size of $0'.5 \times 1'.0$ from the hatched regions in Figure 4.1. Next, we added about 150 and 300 artificial stars into the test fields of NGC 4038/39 and NGC 5584, which correspond to $\sim$ 10% of the total amount of stars detected in each field. These added stars were uniformly distributed throughout the fields and have a magnitude range of $26 \leq I \leq 29$. We set $(V-I) \sim 1.7$ for input artificial stars in order to make them similar to the estimated median $(V-I)$ color at the TRGB magnitude (see Section 3.2). Then, we preformed PSF photometry on the fields in the same way as done on the original images. We then checked recovery rates and photometric systematics. We iterated this process 600 and 300 times for NGC 4038/39 and NGC 5584, respectively, to keep a larger number of artificial stars and to reduce statistical uncertainties. In total, about $100,000$ artificial stars were used for each field in the test.

Figures 4.6 (a) and (d) show the recovery rates for artificial stars as a function of input I-band magnitudes for these two galaxies. About 90% and 70% of stars are expected to be recovered at the TRGB magnitude of NGC 4038/39 ($I_{TRGB} = 27.67 \pm 0.05$) and NGC 5584 ($I_{TRGB} = 27.77 \pm 0.04$). The 50% recovery rates are estimated to be $I \sim 28.3$ for NGC 4038/39 and $I \sim 28.1$ for NGC 5584 . It is noted that, although exposure times of NGC 4038/39 are much shorter than those of NGC 5584, the recovery rates are higher in the same magnitude range. This can be explained as follows. First, the field used in the analysis of NGC 4038/39 is much farther from the center of the host galaxy than that of NGC 5584, so that the expected stellar density is much lower. Second, NGC 4038/39 was observed with ACS/WFC, which has higher sensitivity than the WFC3/UVIS at longer wavelengths of $\sim$ 400 nm. Third, NGC 4038/39 was observed with $F606W$-band, which has a much wider spectral window than the $F555W$-band used for NGC 5584.

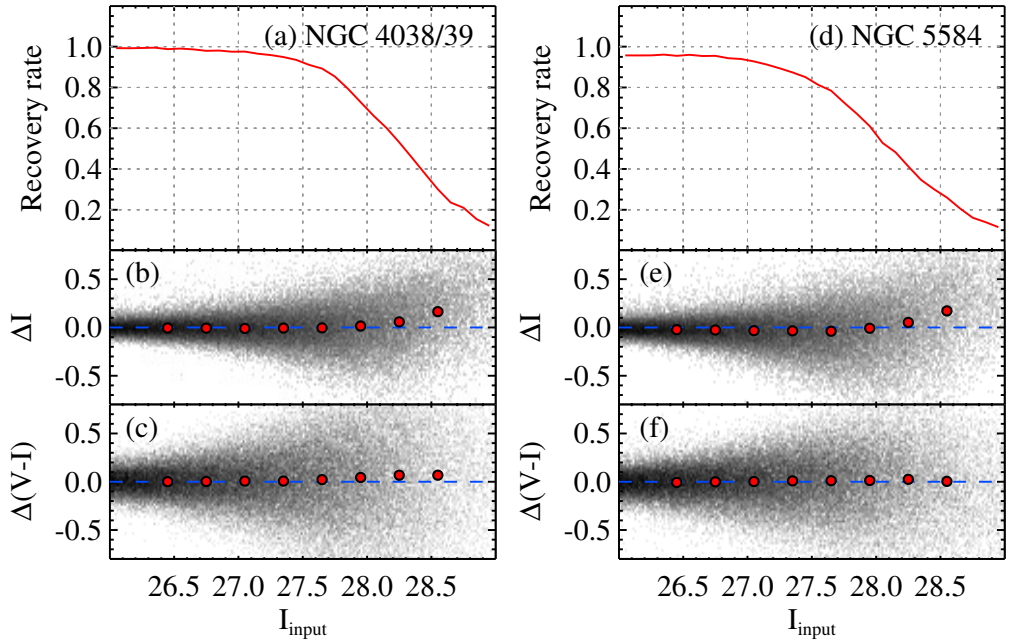

Figure 4.6: (a) Recovery rate of the PSF photometry as a function of I-band magnitude for NGC 4038/39. (b,c) Random and systematic uncertainties of I-band magnitudes (b) and $(V-I)$ colors (c), estimated from artificial star experiments. The differences between input and output magnitudes ($\Delta I = I_{input} - I_{output}$) and colors ($\Delta(V-I) = (V-I)_{input} - (V-I)_{output}$) are shown as density maps, and their median offsets in each magnitude bin are shown as larger circles. ((d), (e) and (f)) Same as (a), (b), and (c) but for NGC 5584.

Figures 4.6 (b), (c), (e) and (f) show random uncertainties and systematic offsets of I-band magnitudes ($\Delta I = I_{input} - I_{output}$) and $V - I$ colors ($\Delta(V - I) = (V - I)_{input} - (V - I)_{output}$) for the two galaxies. Random uncertainties increase gradually, being proportional to the input I-band magnitudes. Systematic offsets are noted. For $I_{input} \gtrsim 28.0$ in (b) and (e), ΔI values are positive. This means that those faint stars are measured slightly brighter than their intrinsic brightness. At the TRGB magnitude of NGC 4038/39 and NGC 5584, such magnitude and color offsets are smaller than 0.02 mag, so we ignored these offsets.

4.3 Results

4.3.1 Color-magnitude Diagrams

The *HST* fields used in this study cover the tidal tail in NGC 4038/39, and the disk and bulge in NGC 5584. Therefore the color-magnitude diagrams of these fields show various populations of stars, such as young main sequence, blue and red super giant, asymptotic giant branch (AGB) and RGB stars. These mixed populations increase uncertainties in determining the TRGB. In order to reduce the contamination due to multiple stellar populations and to sample the RGB population as much as possible, we selected regions with the lowest sky background level, avoiding spiral arms and tidal tails. Chosen regions are marked by the hatched regions in Figure 4.1.

Figure 4.7 show the CMDs of resolved stars in the selected regions of NGC 4038/39 (a), and NGC 5584 (b). We calculated the expected number of galactic foreground stars in each CMD using the TRILEGAL program provided by the Padova group (Girardi et al. 2012). Derived numbers of stars are smaller than ten for both figures, indicating that a contamination by the foreground stars is negligible. We also checked the background galaxy contamination by comparing our CMD with the CMD of the Hubble eXtreme Deep Field (HXDF), where background galaxies are dominated. We used $F606W$ and $F814W$ combined images provided by Illingworth et al. (2013). Total exposure times are 174,400s for $F606W$, and 50,800s

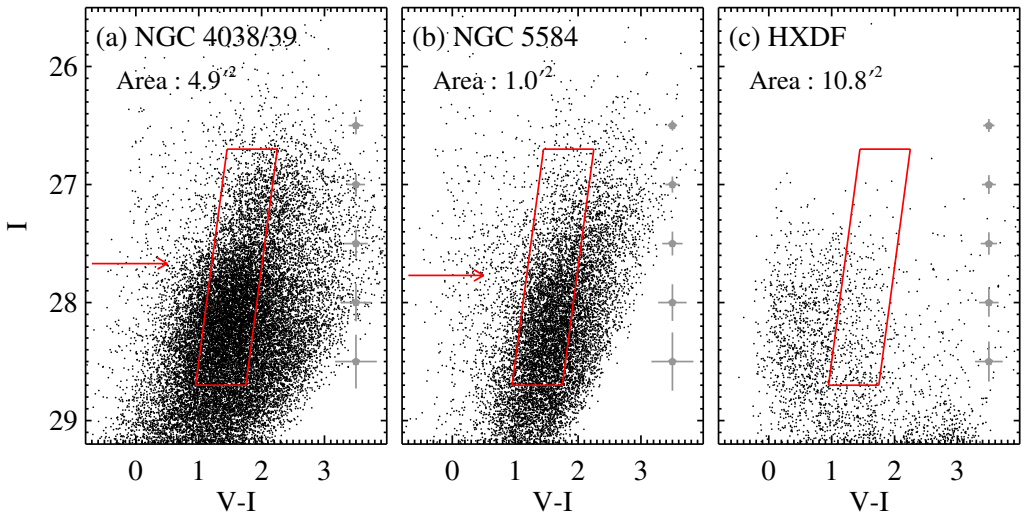

Figure 4.7: Color-magnitude diagrams of resolved stars in the selected regions of NGC 4038/39 (a) and NGC 5584 (b). We also showed the CMD of point sources in the Hubble eXtreme Deep Field (HXDF) as a reference (c). Slanted boxes indicate the boundary of resolved stars used in the TRGB analysis. Estimated TRGB magnitudes are marked by arrows. Crosses with error bars represent mean photometric errors.

for $F814W$. We then carried out the PSF photometry in the same method as for NGC 4038/39 and NGC 5584. Constructed CMD for the point sources in the entire field of HXDF is shown in Figure 4.7 (c). Most of sources are expected to be unresolved background galaxies. We then count the number of sources inside the slanted boxes of each panel, which will be used in the TRGB determination (see next section) : 5247 sources for NGC 4038/39, 4491 sources for NGC 5584, and 318 sources for HXDF. After the correction for the field area differences (4.9 arcmin^2 for NGC 4038/39 field, 1.0 arcmin^2 for NGC 5584 field, and 10.8 arcmin^2 for HXDF), we conclude that the background galaxy contaminations in the CMDs are very small : $\sim 3\%$ for NGC 4038/39 and $\sim 1\%$ for NGC 5584. We ignored this contamination in the following analysis.

The CMDs for NGC 4038/39 and NGC 5584 show clear RGB populations as well as relatively weak main sequence and AGB populations. Both CMDs show a clear number density enrichment of RGB stars at $I \sim 27.7$ for NGC 4038/39, and $I \sim 27.8$ for NGC 5584, which correspond to the TRGB.

4.3.2 Distance Estimation

Our photometry of NGC 4038/39 and NGC 5584 are deep enough to reach more than one magnitude below the TRGB. This enables us to measure distances with the TRGB, a known precise distance indicator (Lee et al. 1993; Freedman & Madore 2010). We derived I-band luminosity functions for resolved stars inside the slanted boxes of Figure 4.7, designed to preferentially select the blue RGB stars.
The use of the blue RGB stars in the analysis has several advantages, as noted in Jang & Lee (2014). First, the TRGB for the bluer RGB stars is less curved than that of the redder RGB stars in the $I-(V-I)$ CMD. Second, the bluer RGB stars have a relatively higher photometric recovery rate than the redder RGB stars. Third, the bluer RGB stars are relatively less affected by the host galaxy reddening.

Figure 4.8 shows derived I-band luminosity functions and corresponding edge-detection responses. We used the logarithmic form of edge-detection algorithm

(Sakai et al. 1996; Méndez et al. 2002), which is described by

$$E(I) = \sqrt{\Phi}[log[\Phi(I + \sigma_I)] - log[\Phi(I - \sigma_I)]]$$

, where $\Phi(I)$ is gaussian-smoothed luminosity function and σ_I is the mean photometric error.

Edge-detection response functions show strong peaks at $I \sim 27.7$ for NGC 4038/39 and $I \sim 27.8$ for NGC 5584, as well as relatively weak peaks at between $I = 26.4$ and 27.0. In a galaxy that contain various stellar populations, the number of AGB stars is much smaller than that of the RGB stars. Therefore, it is expected that the luminosity function of the red giant stars shows a weak jump at the AGB tip, and a much stronger jump at the RGB tip. We determined the prominent peaks to be the TRGB of each galaxy. The relatively weaker peaks in the brighter part of the TRGB are thought to be the tips from intermediate AGB populations or noise. We derive our best estimates of the TRGB magnitudes and their measurement errors from ten thousand simulations of bootstrap resampling. Derived values are $I = 27.67 \pm 0.05$ for NGC 4038/39 and $I = 27.77 \pm 0.04$ for NGC 5584.

We adopted the TRGB calibration suggested by Rizzi et al. (2007), $M_{I,TRGB} = -4.05 + 0.217[(V - I) - 1.6]$, which was also used in our previous studies (Lee & Jang 2012, 2013; Jang & Lee 2014). Median TRGB colors estimated from ~ 200 RGB stars in the ± 0.03 magnitude range of the TRGB are 1.62 ± 0.02 for NGC 4038/39 and 1.66 ± 0.02 for NGC 5584. We adopted foreground extinction values, $E(B - V) = 0.037$ for NGC 4038/39 and $E(B - V) = 0.035$ for NGC 5584 from Schlafly & Finkbeiner (2011). Host galaxy extinctions for the blue RGB stars are expected to be very small, so they are ignored. By combining the TRGB magnitudes, extinction values, and the TRGB calibration, we obtained values of the distance moduli, $(m-M)_0 = 31.67 \pm 0.05$ (random) ± 0.12 (systematic) for NGC 4038/39, and $(m-M)_0 = 31.76 \pm 0.04$ (random) ± 0.12 (systematic) for NGC 5584, as summarized in Table 4.3.

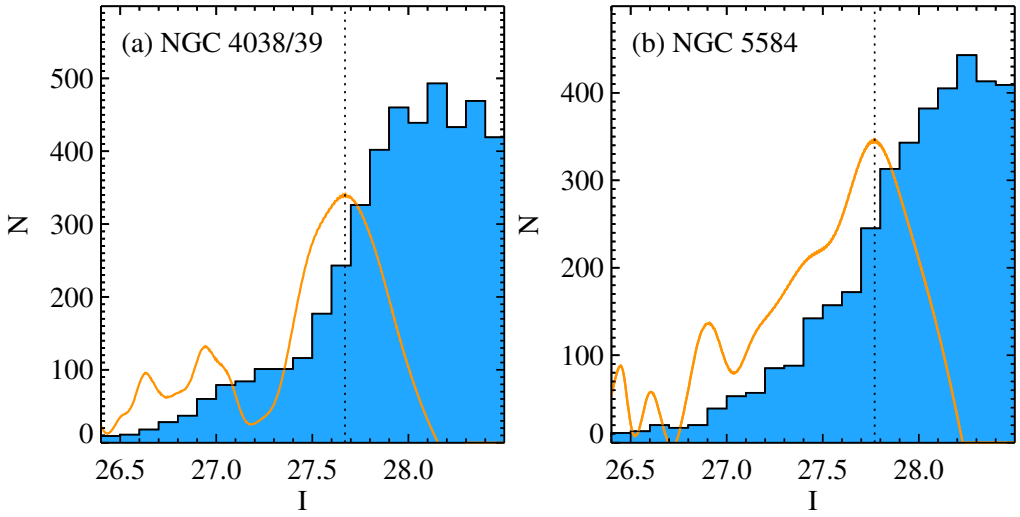

Figure 4.8: *I*-band luminosity functions for the resolved stars in the slanted boxes in Figure 4.7 of NGC 4038/39 (a) and NGC 5584 (b). Edge detection responses and the estimated TRGB magnitudes for each galaxy are shown by solid and dotted lines, respectively.

Table 4.3. A Summary of TRGB Distance Estimates of NGC 4038/39 and NGC 5584

	NGC 4038/39	NGC 5584
TRGB magnitude, I_{TRGB}	27.67 ± 0.05	27.77 ± 0.04
Median TRGB Color, $(V-I)_{TRGB}$	1.62 ± 0.02	1.66 ± 0.02
Galactic extinction, A_I, $E(V-I)$	0.06, 0.05	0.06, 0.05
Intrinsic TRGB magnitude, $I_{0,TRGB}$	27.61 ± 0.05	27.71 ± 0.04
Intrinsic TRGB color, $(V-I)_{0,TRGB}$	1.57 ± 0.02	1.61 ± 0.02
Absolute TRGB magnitude, $M_{I,TRGB}$	-4.06	-4.05
Distance Modulus, $(m-M)_0$	$31.67 \pm 0.05 \pm 0.12^a$	$31.76 \pm 0.04 \pm 0.12^a$
Distance, d	$21.58 \pm 0.50 \pm 1.19^a$ Mpc	$22.49 \pm 0.41 \pm 1.24^a$ Mpc

[a]Systematic errors.

We checked the effect of TRGB color selection to the TRGB distance estimates. We divided the RGBs into four (for NGC 4038/39) and three (for NGC 5584) subregions with different $V-I$ ranges. The TRGB colors of these subregions cover $1.2 < V-I < 2.4$ for NGC 4038/39 and $1.2 < V-I < 2.1$ for NGC 5584, in steps of 0.3 mag. We then derived the TRGB distances for each subregion by applying the same method as done for the blue RGB stars. The TRGB distances for four subregions of NGC 4038/39 show similar values: $(m-M)_0 = 31.60$ to 31.77 with uncertainties of 0.04 to 0.09. A weighted mean of these four estimates is $(m-M)_0 = 31.64 \pm 0.03$, which is in good agreement with the estimate from the blue RGB stars, $(m-M)_0 = 31.67 \pm 0.05$. The three subregions of NGC 5584 also show similar values: $(m-M)_0 = 31.71$ to 31.78 with uncertainties of 0.04 to 0.06. A weighted mean of these estimates is $(m-M)_0 = 31.77 \pm 0.03$, showing an excellent agreement with the estimate from the blue RGB stars, $(m-M)_0 = 31.76 \pm 0.04$. Therefore, we conclude that the TRGB distance estimation depends little on the

color selection of RGB stars.

4.4 Discussion

4.4.1 Comparison with Previous Distance Estimates

Tables 4.4 and 4.5 summarize the distance estimates for each galaxy in this study and in previous studies. Distance estimates for NGC 4038/39 show a large range : $(m-M)_0 = 30.62$ to 31.74. Riess et al. (2011) presented a distance estimate of $(m-M)_0 = 31.66 \pm 0.08$ from the photometry of 35 Cepheid variables. They derived periods of the Cepheid variables from the image data taken with the HST/WFPC2 and apparent magnitudes from the $F160W$ image data taken with the HST/WFC3. Later, Fiorentino et al. (2013) applied their theoretical model to the observational data in Riess et al. (2011), and derived a similar value, $(m-M)_0 = 31.55 \pm 0.06$.

Saviane et al. (2004, 2008) reported relatively short distance estimates based on the TRGB method: $(m-M)_0 = 30.70 \pm 0.25$ from the WFPC2 (Saviane et al. 2004), and $(m-M)_0 = 30.62 \pm 0.17$ from the ACS image data (Saviane et al. 2008). However, Schweizer et al. (2008) reported a much larger value of the TRGB distance, $(m-M)_0 = 31.51 \pm 0.17$ from the same ACS image data as used in Saviane et al. (2008). This ~ 0.9 mag difference comes from the different TRGB magnitudes: $F814W_{0,TRGB} = 26.59 \pm 0.09$ in Saviane et al. (2008) and $T_{RGB} = 27.46 \pm 0.12$ in Schweizer et al. (2008). Schweizer et al. (2008) derived even larger values for the distance moduli: $(m-M)_0 = 31.7 \pm 0.3$ from the peak luminosity of SN Ia, SN 2007sr, and $(m-M)_0 = 31.76 \pm 0.27$ from the systematic recession velocity relative to the Local Group, applying the large scale flow model by Tonry et al. (2000). By considering the distance moduli from three independent methods, Schweizer et al. (2008) suggested to use a conservative value, $D = 22 \pm 3$ Mpc ($(m-M)_0 = 31.7 \pm 0.3$) as the distance to NGC 4038/39.

Our best estimate of the TRGB distance to NGC 4038/39 is $(m-M)_0 = 31.67 \pm 0.05$. It is roughly one mag larger than that found in Saviane et al. (2008). Our

Table 4.4. A Summary of Distance Measurements for NGC 4038/39

ID	References	Method	Distance Modulus	Remarks
1	Amanullah et al. (2010)	SN Ia	30.92 ± 0.36	SALT2, $H_0 = 74.2$ km s^{-1} Mpc^{-1}
2	Schweizer et al. (2008)	SN Ia	31.74 ± 0.27	$H_0 = 72$ km s^{-1} Mpc^{-1}
3	Schweizer et al. (2008)	Recession Velocity	31.76 ± 0.27	$H_0 = 72$ km s^{-1} Mpc^{-1}
4	Riess et al. (2011)	Cepheid	31.66 ± 0.08	# Cepheids = 35
5	Fiorentino et al. (2013)	Cepheid	31.55 ± 0.06	# Cepheids = 32
6	Saviane et al. (2004)	TRGB	30.70 ± 0.25	$I_{TRGB} = 26.5 \pm 0.2$
7	Saviane et al. (2008)	TRGB	30.62 ± 0.17	$F814W_{0,TRGB} = 26.59 \pm 0.09$
8	Schweizer et al. (2008)	TRGB	31.51 ± 0.17	$T_{RGB} = 27.46 \pm 0.12$
9	This Study	TRGB	31.67 ± 0.05	$I_{TRGB} = 27.67 \pm 0.05$

Table 4.5. A Summary of Distance Measurements for NGC 5584

ID	References	Method	Distance Modulus	Remarks
1	Theureau et al. (2007)	TF	31.12 ± 0.40	Mean of J, H, K-band
2	Springob et al. (2009)	TF	31.59 ± 0.49	
3		TF	31.48 ± 0.52	
4	Courtois & Tully (2012)	TF	31.36 ± 0.40	I-band
5	Lagattuta et al. (2013)	TF	30.69 ± 0.69	$H_0 = 100.0$ km s^{-1} Mpc^{-1}
6		TF	31.40 ± 0.69	$H_0 = 72.0$ km s^{-1} Mpc^{-1}
7	Sorce et al. (2012)	TF	31.41 ± 0.42	3.6μm, $(m-M)_{0,LMC} = 18.48$
8	Sorce et al. (2014)	TF	31.28 ± 0.43	3.6μm, $(m-M)_{0,LMC} = 18.48$
9	Brown et al. (2010)	SN Ia	32.30 ± 0.08	MLCS2k2, $R_V = 1.7$, $H_0 = 72.0$ km s^{-1} Mpc^{-1}
10		SN Ia	32.29 ± 0.10	MLCS2k2, $R_V = 3.1$, $H_0 = 72.0$ km s^{-1} Mpc^{-1}
11	Burns et al. (2011)	SN Ia	31.90 ± 0.00	SNooPy, $H_0 = 72.0$ km s^{-1} Mpc^{-1}
12	Amanullah et al. (2010)	SN Ia	31.34 ± 0.37	SALT2, $H_0 = 74.2$ km s^{-1} Mpc^{-1}
13	Riess et al. (2011)	Cepheid	31.72 ± 0.07	# Cepheids = 94
14	Fiorentino et al. (2013)	Cepheid	31.71 ± 0.04	# Cepheids = 78
15	This Study	TRGB	31.76 ± 0.04	$I_{TRGB} = 27.77 \pm 0.04$

estimate is not much different, within errors, from the TRGB distance given by Schweizer et al. (2008) ($(m-M)_0 = 31.51 \pm 0.17$). We investigate any cause for the small difference of 0.16 mag between our best estimate and that of Schweizer et al. (2008). There are three differences in the methods between the two studies. First, Schweizer et al. (2008) used relatively redder RGB stars ($1.6 < (V-I)_0 < 2.6$) than those used in this study. Second they used the entire ACS/WFC field, including tidal tail regions, while we used only the region with low sky values, avoiding tidal tail regions. Third, Schweizer et al. (2008) applied T magnitude ($=I_0 - 0.20[(V-I)_0 - 1.5]$), while we used I magnitude. Using the same T magnitude as used in Schweizer et al. (2008), we derived the TRGB magnitude of $T_{RGB} = 27.47 \pm 0.05$, which is almost the same as the value given by Schweizer et al. (2008) ($T_{RGB} = 27.46 \pm 0.12$). When we used the stars in the lowest sky background regions, avoiding tidal tail regions, as shown in Figure 4.1 (a), we obtained a 0.05 mag fainter value, $T_{RGB} = 27.52 \pm 0.05$. When we used the blue RGB stars ($1.2 \lesssim V-I \lesssim 2.0$, inside the slanted box of Figure 4.7) in the lowest sky background regions, we derive another 0.05 mag fainter value, $T_{RGB} = 27.57 \pm 0.05$. The corresponding distance modulus is $(m-M)_0 = 31.62 \pm 0.05$, which is in agreement with our best estimate, $(m-M)_0 = 31.67 \pm 0.05$, within an uncertainty. Thus, within the 0.16 magnitude difference between our best estimate and that of Schweizer et al. (2008), 0.06 mag comes from field selection, 0.05 mag comes from the TRGB color selection, and 0.05 mag comes from the measurement error. Our estimate is consistent with the Cepheid estimate by Riess et al. (2011) ($(m-M)_0 = 31.66 \pm 0.08$).

Distance estimates for NGC 5584 in the previous studies also show a large range from $(m-M)_0 = 31.12$ to 32.30. Distance estimates using the Tully Fisher relation give a large range ($(m-M)_0 = 31.12 \sim 31.59$) with large uncertainties (Theureau et al. 2007; Springob et al. 2009; Courtois & Tully 2012; Sorce et al. 2012; Lagattuta et al. 2013; Sorce et al. 2014). SN Ia distance estimates show a much larger range from $(m-M)_0 = 31.40$ to 32.30, depending on the selection of the light curve fitting tool, the total to selective extinction ratio (R_V), and the value of the Hubble

Table 4.6. A Summary of Optical Maximum Luminosity Calibration of SNe Ia

Galaxy	SN Ia	Filters	Δ^a	${A_V}^a$	${m_V^0}^a$	Distance Modulus TRGB	M_V^b
NGC 4038/39	SN 2007sr	uBVri	-0.086	0.349	12.404	31.67 ± 0.05	-19.266 ± 0.176
NGC 5584	SN 2007af	uBVri	-0.038	0.346	12.810	31.76 ± 0.04	-18.950 ± 0.171
M101 (NGC 5457)	SN 2011fe	UBVRI	-0.154	0.157	9.955	29.30 ± 0.01	-19.345 ± 0.162
M66 (NGC 3627)	SN 1989B	UBVRI	0.060	1.242	10.591	30.12 ± 0.03	-19.529 ± 0.217
M96 (NGC 3368)	SN 1998bu	UBVRI	-0.021	1.025	10.793	30.15 ± 0.03	-19.357 ± 0.199
Weighted mean of five SNe							-19.266 ± 0.081
Weighted mean of three low-reddened SNe (SN 2007sr, SN 2007af, and SN 2011fe)							-19.192 ± 0.098

[a] Δ, A_V, and m_V^0 denote the luminosity/light-curve shape parameter, the host galaxy extinction, and the corrected apparent peak magnitude described in Jha et al. (2007), respectively.

[b] We added 0.08 mag as an MLCS2k2 fitting uncertainty, 10% of the Milky Way and the host galaxy extinction value as an extinction uncertainty, and 0.14 mag as an intrinsic luminosity dispersion of SNe Ia.

constant. Riess et al. (2011) found 94 cepheid variables from the *HST*/WFC3 image data and derived a distance modulus of $(m - M)_0 = 31.72 \pm 0.07$. Distance modulus derived in this study, the first distance estimate using the TRGB method, is $(m - M)_0 = 31.76 \pm 0.04$. This is in good agreement with the Cepheid estimate by Riess et al. (2011), considering measurement errors. To date, NGC 5584 is the most distant galaxy among the galaxies to which distances were measured using the TRGB method.

4.4.2 The Calibration of SNe Ia and the Hubble Constant

The TRGB distance estimates of SNe Ia host galaxies in this study and our previous studies are very useful in determining the peak luminosity of SNe Ia and the Hubble

constant. M101 (NGC 5457) is a nearby face-on spiral galaxy hosting one SN Ia, SN 2011fe, the nearest low-reddened SNe Ia with modern photometry. It was discovered just 4 hours after its explosion, so complete monitoring observations have been made. Thus, it is an ideal target for the calibration of SNe Ia. Lee & Jang (2012) investigated nine HST/ACS fields around the inner region of M101 and derived a TRGB distance of $(m-M)_0 = 29.30 \pm 0.01$ (random)$\pm$0.12 (systematic).

M66 (NGC 3627) and M96 (NGC 3368) are nearby spiral galaxies in the Leo I group hosting SNe Ia, SN 1989B and SN 1998bu, respectively. The host galaxy extinction values of these two SNe Ia are known to be relatively high ($A_V \gtrsim 1$). However, since they are nearby and their optical light curves from before their maximum magnitudes are available, they are still useful for the calibration of SNe Ia. Lee & Jang (2013) presented new TRGB distances to M66 and M96 based on the deep HST/ACS images : $(m-M)_0 = 30.12 \pm 0.03$(random)$\pm$0.12(systematic) for M66 and $(m-M)_0 = 30.15 \pm 0.03$ (random)$\pm$0.12 (systematic) for M96. We included the TRGB distance estimates for these three galaxies in the luminosity calibration of SNe Ia as well as the two galaxies in this study, NGC 4038/39 and NGC 5584.

We compiled optical light curves of five SNe Ia in the following literature: uBVri photometric data for SN 2007sr and SN 2007af from the Carnegie Supernova Project[7] (u-band) and Hicken et al. (2009) (BVri bands), UBVRI photometric data for SN 2011fe, SN 1989B and SN 1998bu from Pereira et al. (2013), Wells et al. (1994), and Jha et al. (1999), respectively. We added three V-band data points before the pre-maximum of SN 2007sr, given by the All-Sky Automated Survey (ASAS) and Riess et al. (2011). All the photometric data for these five SNe Ia were done with CCD detectors, not photoelectric detectors. Then we ran MLCS2k2 (version 0.07) (Jha et al. 2007) to derive their light curve parameters. We set the total to selective extinction ratio, $R_V = 3.1$ for the Milky Way and $R_V = 2.5$ for SN Ia host galaxies, to be consistent with Riess et al. (2011). We added 0.08 mag as a light curve fit

[7] http://csp.obs.carnegiescience.edu/, (Hamuy et al. 2006)

error, and 10% of the Milky Way and host galaxy extinction values as extinction errors in the error propagation. We also included the intrinsic luminosity dispersion of SNe Ia of 0.14 mag (Jha et al. 2007) in the error calculation.

The values of the parameters derived from the light curve fits are summarized in Table 4.6. Our light curve fit results are consistent with those in Jha et al. (2007) and Riess et al. (2011), within fitting uncertainty. Figure 4.9 shows a comparison of TRGB distance estimates, V-band absolute peak magnitudes, and host galaxy extinction values of the five SNe Ia. Two features are noted. First, the host galaxy extinction values for SN 1989B and SN 1998bu are much larger than those of the other three SNe Ia. Thus the derived light curve parameters from these two SNe may be less reliable, although we corrected for their extinctions. Second, SN 2007af is as bright as those in our previous studies, while SN 2007af is somewhat fainter. The standard deviation for five SNe Ia is 0.21 mag, slightly larger than the luminosity dispersion of the distant SNe Ia, 0.14 mag (Jha et al. 2007). This may be due to small number statistics. Further studies adding more SNe Ia in the luminosity calibration is needed.

A weighted mean value of the V-band absolute peak magnitudes of five SNe is estimated to be $M_V = -19.27 \pm 0.08$. It is 0.15 mag brighter than that of the SH0ES project ($M_V = -19.12$, Riess et al. (2011)) and 0.2 mag fainter than those of the Hubble Key project ($M_V = -19.46$, Freedman et al. (2001)) and the HST key project ($M_V = -19.46$, Sandage et al. (2006)). If we adopt 3 low-reddened SNe (SN 2007sr, SN 2007af, and SN 2011fe), then the absolute peak magnitude would be slightly fainter, $M_V = -19.19 \pm 0.10$, getting closer to the estimate given by Riess et al. (2011).

Riess et al. (2011) presented the relation between the absolute magnitude of SNe Ia and the Hubble constant based on the MLCS2k2 fits of 140 SNe Ia at $0.023 < z < 0.1$:

$$logH_0 = \frac{M_V^0 + 5a_v + 25}{5} \text{ and } a_v = 0.697 \pm 0.002.$$

Using the absolute magnitudes derived in this study to the above equation, we

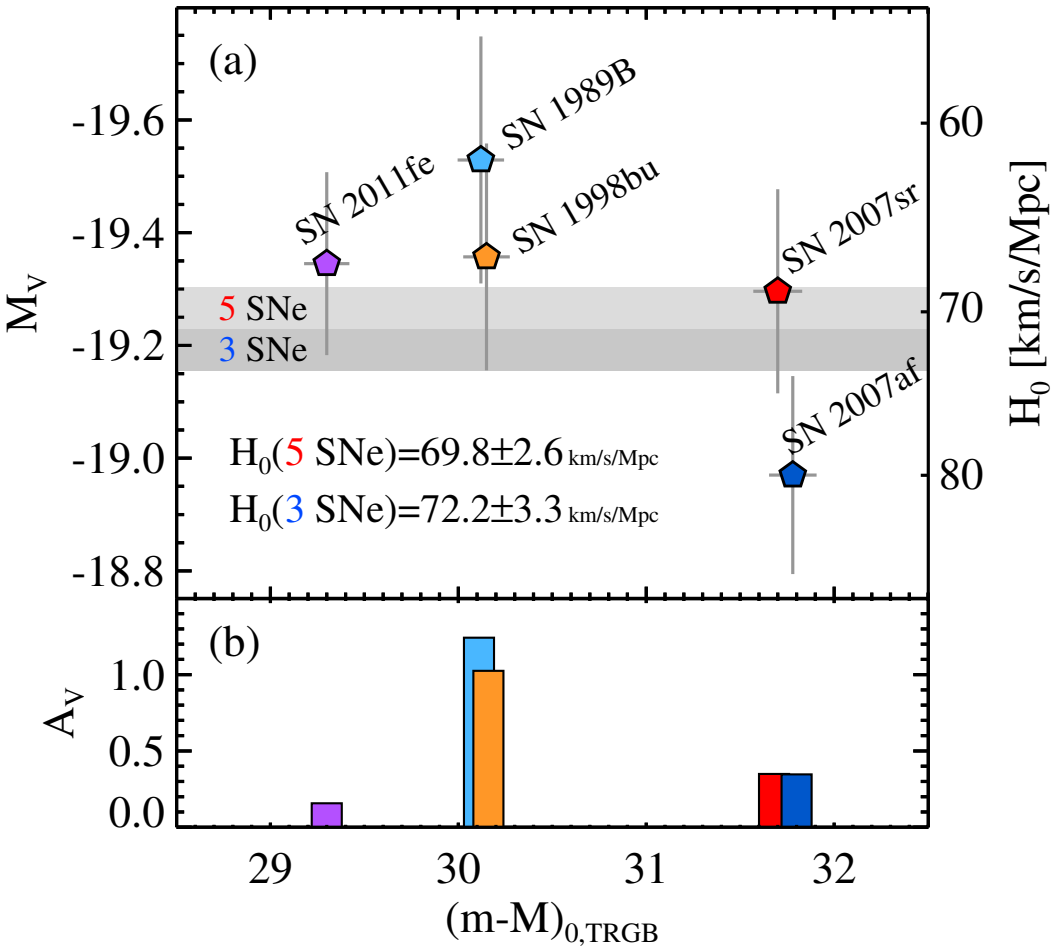

Figure 4.9: (a) Comparison of absolute magnitudes of five SNe Ia with their TRGB distances derived in this study and from our previous studies. Two shaded regions denote the weighted mean of five (upper region) and three (lower region) SNe Ia. (b) Comparison of V-band host galaxy extinction values of SNe Ia and their TRGB distances. Note that the extinction values for SN 1989B and SN 1998bu are much higher than other three SNe Ia.

derived a Hubble constant : $H_0 = 69.8 \pm 2.6$ (random)$\pm$3.9 (systematic) km s^{-1} Mpc^{-1} from the five SNe, and $H_0 = 72.2 \pm 3.3$ (random)$\pm$4.0 (systematic) km s^{-1} Mpc^{-1} from the three low-reddened SNe. Our estimate based on the five SNe is similar to the values from the CMBR analysis, $H_0 \simeq 69$ km s^{-1} Mpc^{-1} (Bennett et al. 2013; Planck Collaboration et al. 2015) and not much different, within the errors, from those of recent Cepheid calibrations of SNe Ia, $H_0 \simeq 74$ km s^{-1} Mpc^{-1} (Riess et al. 2011; Freedman et al. 2012). Our estimate based on the three low-reddened SNe is between the values from the two independent methods.

4.5 Summary

We present the TRGB distance estimates for SN Ia host galaxies NGC 4038/39 and NGC 5584 from the PSF photometry of archival *HST* images. A summary of the main results in this study is as follows.

- We detected RGB stars in the outer region of NGC 4038/39 and NGC 5584 based on the combined archival ACS/WFC and WFC3/UVIS image data.
- We derived photometric transformation between $F555W$ and $F814W$ bands of WFC3/UVIS and that of ACS/WFC, by comparing the photometry of the resolved stars in two Milky Way globular clusters, NGC 2419 and 47 Tuc.
- We found I-band TRGB magnitudes to be at $I_{TRGB} = 27.67 \pm 0.05$ for NGC 4038/39 and $I_{TRGB} = 27.77 \pm 0.04$ for NGC 5584. From these, we derived the TRGB distance estimates of $(m-M)_0 = 31.67 \pm 0.05 \pm 0.12$ for NGC 4038/39 and $(m-M)_0 = 31.76 \pm 0.04 \pm 0.12$ for NGC 5584.
- Based on distance estimates for the two SNe derived in this study and that of the three SNe in our previous studies, we calibrate the V-band peak absolute magnitude of SNe Ia.
- From the mean absolute magnitude of five SNe Ia, the Hubble constant is determined to be $H_0 = 69.8 \pm 2.6 \pm 3.9$ km s^{-1} Mpc^{-1}, which is similar to the

values from the CMBR analysis, $H_0 \simeq 69$ km s^{-1} Mpc^{-1} (Bennett et al. 2013; Planck Collaboration et al. 2015). Our estimate is slightly smaller, but agrees within errors, with the values from the recent calibrations of SNe Ia with the Cepheid variables, $H_0 \simeq 74$ km s^{-1} Mpc^{-1} (Riess et al. 2011; Freedman et al. 2012). If we adopt 3 low-reddened SNe, corresponding the Hubble constant is slightly increased, $H_0 = 72.2 \pm 3.3$ (random)$\pm$4.0 (systematic) km s^{-1} Mpc^{-1}.

This Chapter has been published in *The Astrophysical Journal* as Jang & Lee 2015, v. 807, p. 133.

Chapter 5

The TRGB Distances to SN Ia Host Galaxies. IV. Color Dependence and Zero-Point Calibration

5.1 Introduction

The Tip of the Red Giant Branch (TRGB) represents the brightest part of the Red Giant Branch (RGB) in the color-magnitude diagrams (CMDs) of old stellar systems such as globular clusters and halos in galaxies. It corresponds to the core-He flash point in the evolutionary stages of low mass stars. An implication of the TRGB as a distance indicator was suggested first by Baade (1944). In his pioneering paper introducing the concept of stellar populations I and II, he investigated the red-sensitive plates of three early type stellar systems, M32, NGC 205, and the central region (bulge) of M31, concluding that the brightest stars (RGB stars) in these three systems have similar magnitudes and colors. Sandage (1971) pointed out that photographs of the Local Group galaxies invariably show surrounding red stars,

which have similar absolute magnitudes and colors. Based on the Cepheid distances to three Local Group galaxies (M31, M33 and IC 1613), he derived a mean absolute magnitude of these brightest red stars to be $M_V = -3.0 \pm 0.2$ mag.

Mould et al. (1983, 1984) and Mould & Kristian (1986) carried out CCD photometry of four Local Group galaxies (M31, M33, NGC 147 and NGC 205) and determined the TRGB distances to these galaxies, which are not much different from previous distance estimates to M31 and M33 based on Cepheid variables. They adopted a bolometric magnitude of the TRGB ($M_{\rm bol} \sim -3.5$ mag) given by Frogel et al. (1983). Freedman (1988b) presented CCD photometry of two fields in IC 1613. Color-magnitude diagrams (CMDs) of these fields show a clear RGB population and the TRGB. Adopting the bolometric magnitude the TRGB ($M_{\rm bol} \sim -3.5$ mag), she derived remarkably similar TRGB distances between the two fields, showing only 0.04 mag difference. Moreover, the TRGB distance from her photometry is in excellent agreement with the Cepheid distance to IC 1613 obtained by Freedman (1988a).

A feasibility of the TRGB as a robust distance indicator was established by Lee et al. (1993). They investigated empirical RGB loci of the Milky Way globular clusters (Da Costa & Armandroff 1990) and Yale theoretical stellar isochrones (Green et al. 1987), finding that the I-band magnitude of the TRGB is almost constant with variation smaller than 0.1 mag ($M_{I,\rm TRGB} = -4.0 \pm 0.1$) for low metallicity ([Fe/H]≤ -0.7) or for age older than 3 Gyr. Also, they applied a Sobel kernel for detecting the TRGB from the discontinuity of the I-band luminosity function. They found that a comparison of the TRGB distances to 12 Local Group galaxies with the distances based on Cepheid and RR-Lyrae variables shows a good agreement, showing that the precision of the TRGB is comparable to these primary distance indicators. With the TRGB, distances to more than three hundreds of nearby galaxies have been measured (Freedman & Madore 2010; Dalcanton et al. 2009; Radburn-Smith et al. 2011; Tully et al. 2013; Lee & Jang 2013, 2016).

In comparison with the Cepheid variables, which are a well known primary dis-

tance indicator, the TRGB has several advantages. First, the TRGB method uses Population II RGB stars. It enables to measure distances to both early type galaxies and late type galaxies, while Cepheid variables can be used only for late type galaxies. Second, the TRGB method mainly uses RGB stars in the halo regions, where stellar densities are low and internal extinctions are negligible, while Cepheid variables are located in the star-forming regions where internal extinctions are often significant. Third, the TRGB stars are non-variable stars, so that a single epoch observation is enough to get distances, while Cepheids require many epochs of observations. Fourth, the metallicity dependence of the I-band magnitude of the TRGB is known to be small for low metallicity(Lee et al. 1993; Rizzi et al. 2007; Madore et al. 2009; Bellazzini 2008), while the metallicity effect on the optical luminosity of Cepheids is controversial (Gerke et al. 2011).

On the other hand, the TRGB has a disadvantage that its luminosity is relatively fainter than those of the bright Cepheid variables. The absolute magnitude of the brightest Cepheid variable is estimated to be $M_V \sim -7$ mag, about 4.5 mag brighter than that of the TRGB, $M_V \sim -2.5$ mag. This difference becomes smaller in the longer wavelength: Δmag = 3.9, 3.1, 2.6 and 2.6 mag in I, J, H, and K_s bands, respectively (Macri et al. 2006, 2015, assuming the maximum period of Cepheid variables (P_{max} = 100 days).

Taking advantage of the TRGB, we started a project to improve luminosity calibration of Type Ia supernovae (SNe Ia) by measuring accurate TRGB distances to SN Ia host galaxies. Lee & Jang (2012) (Paper I) presented a TRGB distance to nearby spiral galaxy M101 hosting SN 2011fe. Lee & Jang (2013) (Paper II) determined TRGB distances to M66 and M96 in the Leo I group hosting two SNe Ia, SN 1989B and SN 1998bu. Later, Jang & Lee (2015) (Paper III) obtained TRGB distances to two galaxies, NGC 4038/39 hosting SN 2007sr and NGC 5584 hosting SN 2007af. Combining the TRGB distances and optical light curves of the five SNe Ia, Jang & Lee (2015) derived a value of the Hubble constant, $H_0 = 69.8 \pm 2.6 \pm 3.9$ km s^{-1} Mpc^{-1}. This value is similar to those from the cosmic microwave background

(Bennett et al. 2014; Planck Collaboration et al. 2015) but still agrees with in errors from those of Cepheid calibrated SNe Ia (Riess et al. 2011; Freedman et al. 2012; Riess et al. 2016). In order to make better estimation of H_0, it is needed to reduce both random and systematic uncertainties.

This paper, the fourth paper of our series, is aiming to refine two issues in the TRGB method: a calibration of the color (metallicity) – luminosity relation and a calibration of the zero-point of the TRGB magnitude. Both calibrations are important to reduce the systematic uncertainty of the TRGB distance estimates and of the value of the Hubble constant. Previous color dependence calibrations were based on theoretical stellar models (Salaris & Cassisi 1997; Fusco et al. 2012), or on a small number of stellar systems (Milky Way globular clusters or nearby galaxies) showing a narrow RGB color range (Lee et al. 1993; Bellazzini et al. 2001, 2004; Rizzi et al. 2007; Bellazzini 2008; Madore et al. 2009). These calibrations show a significant discrepancy of the color – luminosity relation ranging from flat to steep (as shown in the Discussion section).

Zero-point calibrations of the TRGB in previous studies were done with theoretical models (Salaris & Cassisi 1997; Fusco et al. 2012) or observational approaches (Lee et al. 1993; Ferrarese et al. 2000; Bellazzini et al. 2001, 2004; Rizzi et al. 2007; Bellazzini 2008; Tammann et al. 2008; Madore et al. 2009). Various distance indicators (RR Lyrae stars, Cepheids, eclipsing binary stars, and horizontal branch stars) have been used for this calibration. However, derived values show a non-negligible scatter with a large uncertainty, as shown in the Discussion section.

This paper is composed of as follows. In Section 2 we describe how we derive color (metallicity) - luminosity relation of the TRGB. Target galaxy selection criteria and data reduction methods will be presented. §3 shows the zero-point calibration of the TRGB based on two distance anchors: NGC 4258 and the LMC. A summary of the revised TRGB calibration including various filter systems is shown in §4. We discuss implications of our results in §5 and summarize primary results in the final section.

5.2 Color Dependence Calibration

5.2.1 Target Selection and Data Reduction

Optimal target galaxies and target fields for the color (metallicity) dependence calibration of the TRGB are expected to satisfy the following criteria: 1) showing a wide color range of the TRGB, covering from the metal poor (blue) RGB stars to the metal rich (red) RGB stars, 2) allowing a high signal to noise detection of RGB stars, 3) showing a dominant old RGB population, and 4) being observed with the same instrument to reduce any chance for increasing instrument-dependent uncertainties (e.g. photometric transformation uncertainties). Considering these selection criteria, we selected 14 fields around 8 nearby galaxies for which *HST*/Advanced Camera for Surveys (*ACS*) images are available in the archive: M105 (E1), NGC 3384 (SB0), M81 (SA(s)AB), NGC 3377 (E5-6), NGC 253 (SAB(s)c), NGC 4258 (SAB(s)bc), NGC 300 (SA(s)d), and NGC 3077 (I0 pec).

These galaxies have various morphological types from elliptical galaxies to spiral and irregular galaxies. Identifications of the *HST* fields in each galaxy are shown in Figure 5.1. These *HST* fields are located from the center to outer regions in the target galaxies. Note that the three fields in NGC 300 are located in the disk. Rizzi et al. (2007) used two *HST*/*ACS* fields in other positions of the NGC 300 disk for their TRGB color calibration. For this reason, we also included disk fields of NGC 300 for which deeper HST/ACS images are available. Table 5.1 lists a summary of *HST*/*ACS* observations of the target galaxies. Exposure times are ranging from 1,515s to 38,500s, long enough to detect resolved red giants. It is noted that NGC 4258 was observed with F555W filter, while other galaxies were observed with F606W filter.

We obtained ACS images of the fields from the *HST* archive and constructed deep master drizzled images, following the procedures described in Jang & Lee (2015). In our previous studies (Lee & Jang 2012, 2013; Jang & Lee 2015), we carried out point spread function (PSF) photometry using DAOPHOT in IRAF

Table 5.1. A Summary of *HST* Observations of the TRGB Calibration Sample

Target	Field	R.A. (J2000.0)	Decl. (J2000.0)	Instrument	Exposure time F555W	F606W	F814W	Prop. ID
M105	F1	10 48 01.53	12 32 28.2	ACS/WFC		9,775s	9,775s	10413
	F2	10 48 00.20	12 32 06.8	ACS/WFC		9,775s	9,775s	10413
NGC 3384	F1	10 48 26.03	12 39 50.6	ACS/WFC		14,575s	14,575s	10413
	F2	10 48 22.38	12 39 08.6	ACS/WFC		9,825s	9,825s	10413
M81	F1	09 54 34.56	69 16 50.9	ACS/WFC		24,232s	29,953s	10915
	F2	09 54 13.96	69 05 42.6	ACS/WFC		5,354s	5,501s	10136
	F3	09 57 01.20	68 55 55.6	ACS/WFC		1,580s	1,595s	10584
NGC 3377	F1	10 47 48.11	13 55 45.2	ACS/WFC		38,500s	22,260s	9811
NGC 253	F1	00 48 19.46	–25 08 47.4	ACS/WFC		2,283s	2,253s	10915
NGC 4258	F1	12 19 18.37	47 20 13.8	ACS/WFC	5,700s		2,600s	9477
NGC 300	F1	00 54 47.98	–37 40 51.6	ACS/WFC		1,515s	1,542s	10915
	F2	00 54 34.70	–37 39 25.4	ACS/WFC		1,515s	1,542s	10915
	F3	00 54 21.37	–37 37 56.3	ACS/WFC		1,515s	1,542s	10915
NGC 3077	F1	10 03 28.41	68 43 52.8	ACS/WFC		1,596s	1,622s	10915

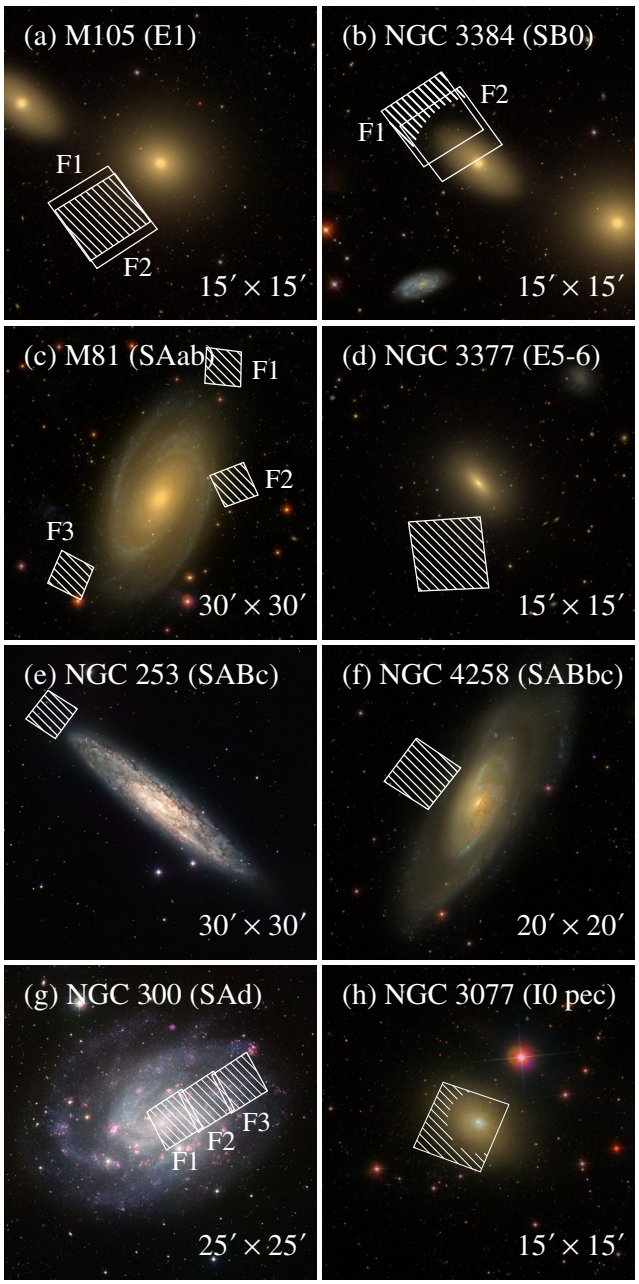

Figure 5.1: Finding charts for eight galaxies used for the color dependence calibration of the TRGB: M105 (a), NGC 3384 (b), M81 (c), NGC 3377 (d), NGC 253 (e), NGC 4258 (f), NGC 300 (g), and NGC 3077 (h). HST/ACS fields used in this study are marked on the color maps of the Sloan Digital Sky Survey (SDSS) or public images provided by the European Southern Observatory (ESO). The regions we used for the TRGB calibration are indicated by the hatched regions.

package (Stetson 1987). We noted, however, that most of the previous and on-going studies for the calibration of SNe Ia (e.g. the Hubble Key Project, the HST key project (Sandage et al. 2006), the SN HST Project (Freedman et al. 2001), the SH0ES Project (Riess et al. 2011), and the Carnegie-Chicago Hubble Program (Beaton et al. 2016)) have been done with the standalone version of DAOPHOT (Stetson 1987). Moreover, the Optical Gravitational Lensing Experiment (OGLE) photometric data of the LMC (Ulaczyk et al. 2012), which we used in the zero-point calibration of the TRGB (see Section 3.2) is also based on the standalone version of DAOPHOT. Thus, we use the standalone version of DAOPHOT in this study, to reduce software dependent uncertainty as much as possible. Our previous results based on IRAF/DAOPHOT will be updated in the upcoming paper (Jang & Lee 2016, in preparation). A single pass sequence (DAOFIND, PHOT, ALLSTAR and ALLFRAME) of PSF photometry was carried out. We used PSF images produced from isolated bright stars in each *ACS* field. We adopted updated photometric zero-points and aperture correction values provided by the STScI webpage[1].

5.2.2 CMDs of Resolved Stars and the TRGB detection

In Figure 5.2 (a, c, e, g, i, k, m, and o), we display CMDs of the resolved stars in the selected regions, marked by hatched regions in Figure 5.1, of each galaxy. The central regions of NGC 3384 ($R \leq 3'$), NGC 300 ($R \leq 0\farcm6$), and NGC 3077 ($R \leq 1\farcm5$) were discarded in the analysis because of serious crowding due to high stellar densities. The most prominent feature in all CMDs is a distinguishable RGB. The width of the RGBs shows a large variation: from narrow RGBs for low mass galaxies (NGC 300 and NGC 3077) to broad RGBs for high mass galaxies (M105 and M81). All CMDs show also a small population of asymptotic giant branch (AGB) stars. The CMD of the disk fields in NGC 300 shows not only a strong old RGB but also the presence of red core helium burning stars with much younger age at $(\mathrm{F606W–F814W})_0 \approx 1.0$.

[1] http://www.stsci.edu/hst/acs/analysis/zeropoints

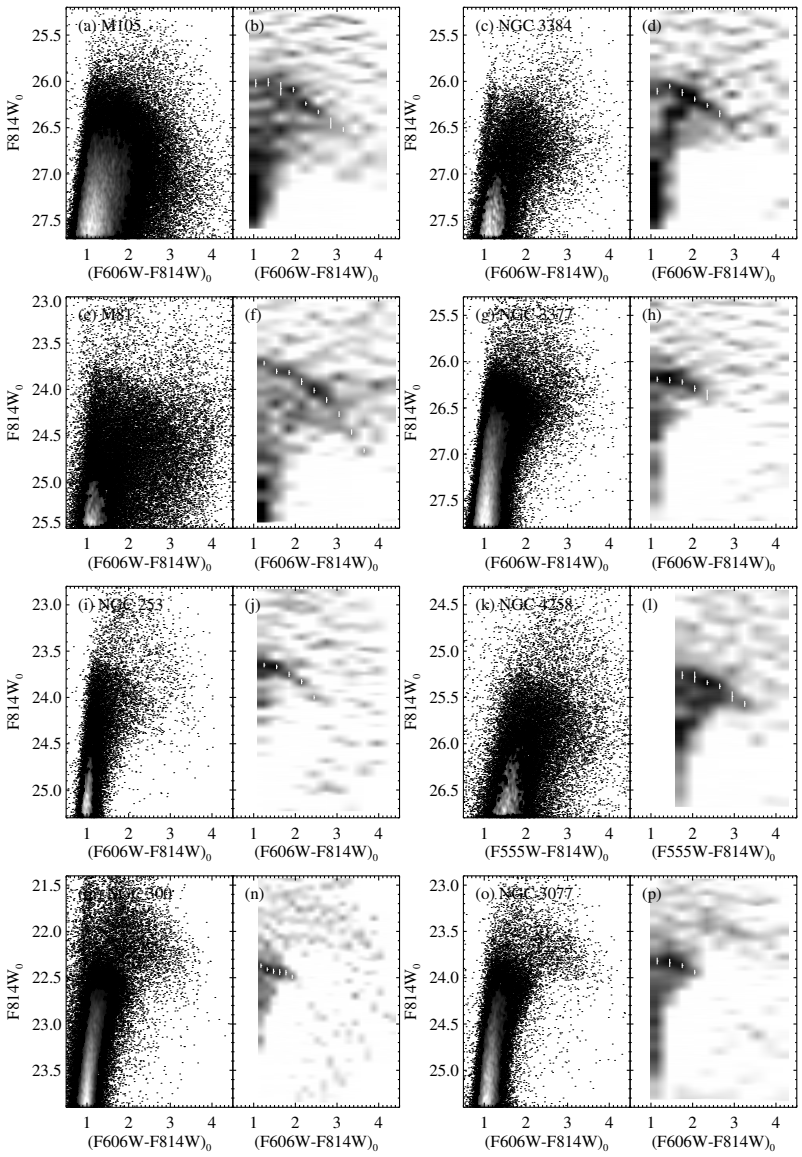

Figure 5.2: (Left windows in each panel) Foreground reddening-corrected CMDs of the resolved stars in eight galaxies used for the color-dependence calibration. High density regions in each CMD are displayed as a density map (Hess diagram). (Right windows in each panel) Maps showing the strength of edge detection responses. We divided the stars in each CMD into subgroups based on their color and applied an edge detection algorithm. Dark and pale regions in each map represent strong and weak edge detection responses, respectively. Estimated TRGB magnitudes and their errors for the subgroups are marked by white vertical lines. Note that $(\mathrm{F555W} - \mathrm{F814W})_0$ colors were used for NGC 4258, while $(\mathrm{F606W} - \mathrm{F814W})_0$ colors were used for the other galaxies.

We detected the TRGB by applying the weighted logarithmic edge-detection algorithm given by Méndez et al. (2002). In order to check the color-magnitude relation of the TRGB, we divided the stars into sub-groups according to their color with a color interval of 0.3 mag. In the case of NGC 300, we used a color interval of 0.15 mag because the CMD of this galaxy contains a much larger number of blue RGB stars. Figure 5.2 (b, d, f, h, j, l, n, and p) shows the TRGB detection results for the target galaxies. Edge detection responses are indicated by grey scale maps: black for strong response (sharp discontinuity in the luminosity function) and white for weak response. The TRGB magnitudes and corresponding measurement uncertainties are determined through ten thousand simulations of bootstrap resampling. Derived values and errors are indicated by white vertical lines in each grey scale map. All eight galaxies show clearly color - magnitude relations of the TRGB: the TRGBs become fainter, as color increases.

Madore et al. (2009) pointed out that at least 400 $\sim$ 500 stars in the one mag interval below the TRGB are needed to detect the TRGB within the Poisson noise of 0.1 mag. Considering this, we set 100 RGB stars in 0.2 mag interval below the TRGB as a criterion for analysis. We chose a narrower range of magnitude, to use photometry with higher completeness. Then we counted the number of RGB stars in each subgroup in each galaxy to check whether they have a sufficient number of RGB stars for precise determination of the TRGB or not. Only the cases satisfying our selection criteria above, as indicated by white vertical lines in Figure 5.2, were used in the following analysis.

5.2.3 Color Transformation between F555W − F814W and F606W − F814W

NGC 4258 is an important galaxy for calibrations of both the color dependence and the zero-point, because it shows a broad range of RGB color and hosts a megamaser, which is useful for geometric distance estimation. NGC 4258 was observed with F555W and F814W filters. However, the other galaxies used for color dependence

calibration were observed with F606W and F814W filters. Therefore, the color transformation between F555W − F814W and F606W − F814W is needed for a direct comparison. Sirianni et al. (2005) provides photometric transformations from ACS to Johnson-Cousins systems. With these relations, F555W − F814W can be converted to $V - I$, and $V - I$ can also be converted to F606W − F814W. This method enables the color transformation between the two ACS colors. However, applying transformation twice would increase a systematic uncertainty.

In Paper III (Jang & Lee 2015), we presented F555W, F606W, and F814W bands photometry of two Milky Way globular clusters, NGC 2419 and 47 Tuc. Using the photometric catalogs of the stars in the two globular clusters obtained from our previous study, we derive a direct color transformation. We selected resolved stars in each globular cluster with the following criteria: $R \geq 1'$ and $18.5 <$ F814W ≤ 21.0 for NGC 2419, and $R \geq 7'$ and $19.5 <$ F814W ≤ 22.0 for 47 Tuc (see Figure 4 of Jang & Lee (2015)). A comparison of two ACS colors from the selected stars is shown in Figure 5.3(a). The F606W − F814W color ranges from 0.0 to 2.8. A large scatter of NGC 2419 stars at F606W − F814W ~ 0.5 is probably due to the RR Lyrae variables. The distribution of stars can be fitted well by two linear relations (solid and dashed lines) with a break at F606W − F814W = 1.5:

$$(\text{F555W} - \text{F814W}) = (1.393 \pm 0.003)(\text{F606W} - \text{F814W}) - (0.004 \pm 0.004) \quad (5.1)$$

for F606W − F814W ≤ 1.5, and

$$(\text{F555W} - \text{F814W}) = (1.148 \pm 0.021)(\text{F606W} - \text{F814W}) + (0.336 \pm 0.035) \quad (5.2)$$

for F606W − F814W > 1.5.

Figure 5.3(b) displays F555W − F814W color difference between the observed stars and the linear relation of the red stars (F606W − F814W > 1.5). We overlay a stellar isochrone for 12 Gyr age, and [Fe/H] $= -1.4$, which is a mean metallicity of the two globular clusters, in the Dartmouth models (Dotter et al. 2008) as a curved line. We also overlay a relation from the transformations given in Sirianni et

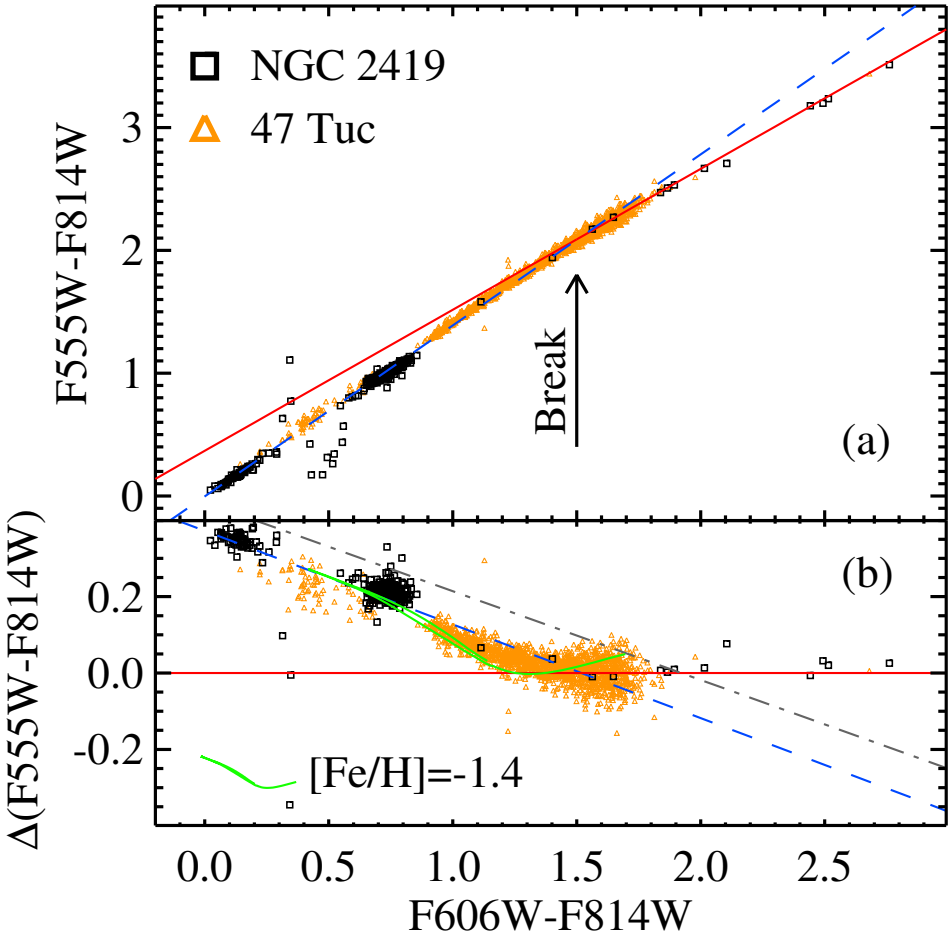

Figure 5.3: (a) Color difference between F606W − F814W and F555W − F814W as a function of F606W − F814W color for the stars in NGC 2419 (open squares) and 47 Tuc (open triangles). Blue dashed lines and red solid lines show double linear fits to the observed colors: the blue stars (F606W − F814W $\leq$ 1.5, dashed line) and the red stars (F606W − F814W $>$ 1.5, solid line). (b) Residual F555W − F814W color after subtraction of the linear fit for the red stars (F606W − F814W $>$ 1.5). The curved line indicates 12 Gyr stellar isochrone for a metallicity of [Fe/H]= −1.4, which is a mean metallicity of the two globular clusters, provided by the Dartmouth group. The gray dot-dashed line represents the color relation expected from the photometric transformations given in Sirianni et al. (2005), which is $\sim$ 0.1 mag redder.

al. (2005) (dot-dashed line). Theoretical model agrees very well with the observed stars. However, the relation from Sirianni et al. (2005) shows a systematic offset of ~ 0.1 mag. We use double linear relations derived in this study in the following analysis.

5.2.4 Deriving Color - Magnitude relation

In Figure 5.4, we plotted the F606W$-$F814W color and F814W magnitude relations of the TRGB stars in eight galaxies. The F555W $-$ F814W color of NGC 4258 was converted to F606W $-$ F814W color using the transformation described in Section 2.3. The TRGB magnitudes show a clear non-linear relation as a function of color. We use an equation as below, keeping quadratic terms for the approximation of the TRGB:

$$\mathrm{F814W_{TRGB}} = \alpha(\mathrm{Color_{TRGB}} - \gamma)^2 + \beta(\mathrm{Color_{TRGB}} - \gamma) + \delta \qquad (5.3)$$

where γ means a fiducial color at [Fe/H] $= -1.6$. In the case of F606W $-$ F814W combination, the value of γ corresponds to 1.1. Coefficients α and β determine the shape of the relation, and δ reflects apparent magnitudes of the TRGB in each galaxy. Thus, values of α and β are the same in all eight galaxies, but that of δ depends on galaxies. We carried out a multi-parameter fitting using the IDL/mpfitexpr to find the values of three coefficients, yielding $\alpha = 0.123 \pm 0.006$, $\beta = 0.042 \pm 0.014$, and $\delta = 22.4 \sim 26.0$. The best fit results are plotted as solid lines in each panel of Figure 5.4. We shifted the TRGB magnitudes and corresponding fit results of each galaxy along the vertical direction, to be consistent with the result from NGC 4258, and plotted them in Figure 5.5(a). All eight galaxies show reasonable agreements. The difference between the data points and the best fit result is shown in Figure 5.5(b). The root mean square of data is estimated to be 0.027 mag. It is similar to the mean measurement uncertainty of the TRGB.

We computed the correction parameters α, β, and γ for several different filter systems as well. The values for F555W $-$ F814W combination in ACS/WFC were

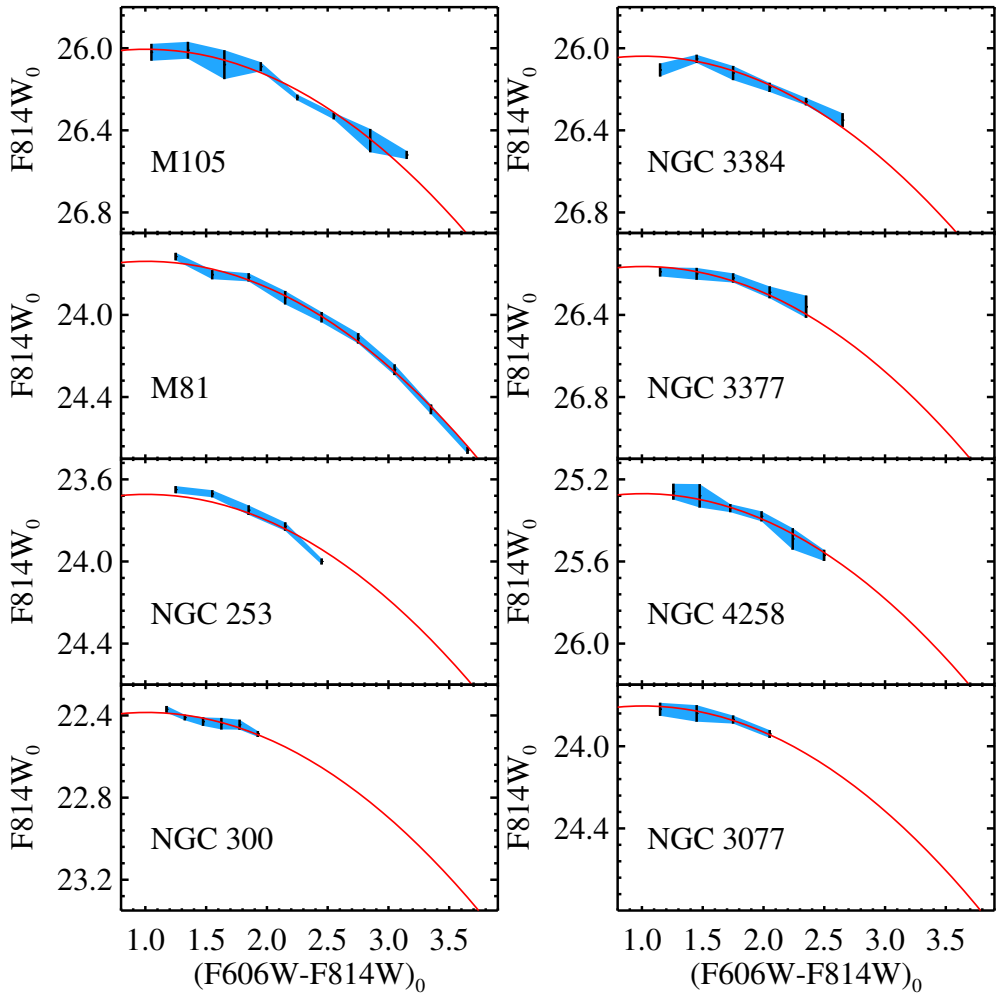

Figure 5.4: F814W$_0$−(F606W−F814W)$_0$ color-magnitude relations of the TRGB for eight galaxies. Blue shaded regions with vertical short lines represent the measured TRGB magnitudes with errors. The best fit results with quadratic equations are shown by the red curved lines.

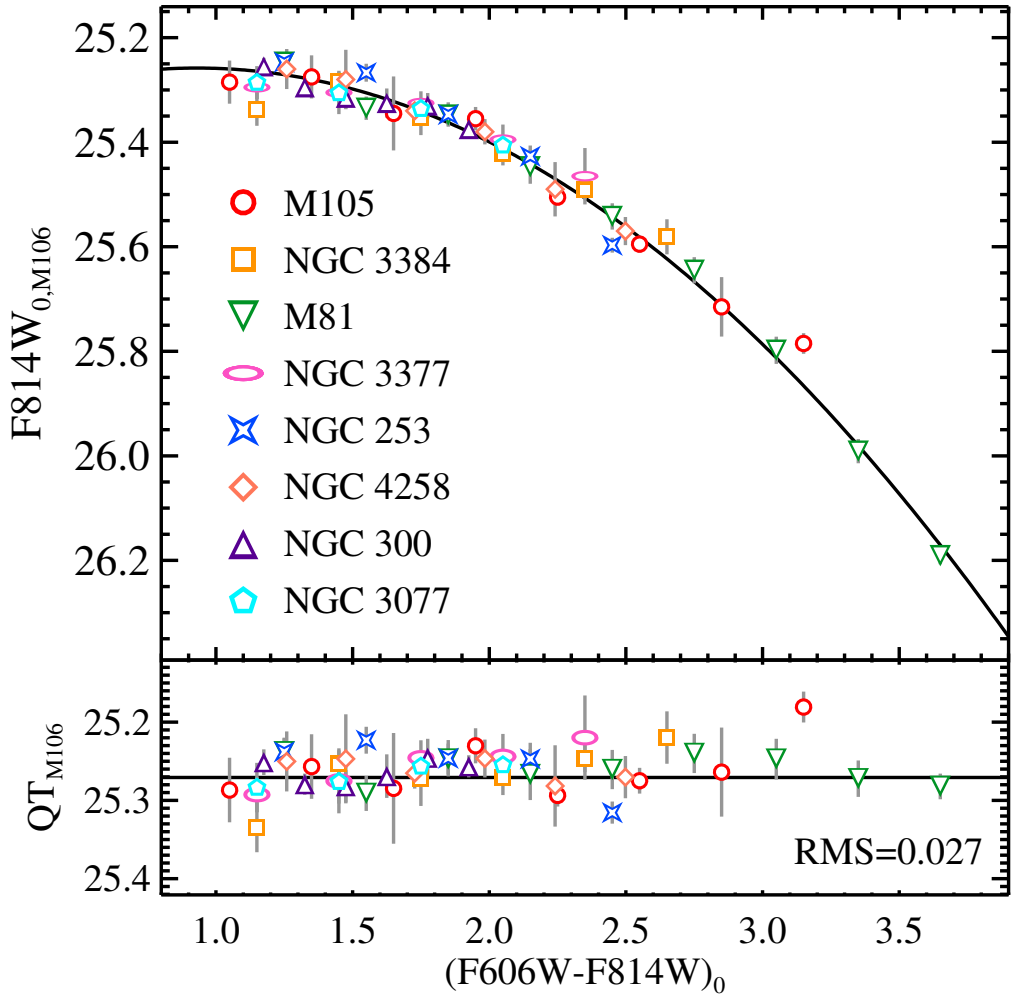

Figure 5.5: (Top) Combined $F814W_0$ magnitudes of the TRGB for eight galaxies as a function of $(F606W - F814W)_0$ color. $F814W_0$ magnitudes of each galaxy were shifted along the vertical direction, to be consistent with the result from NGC 4258. The solid line denotes the best fit result. (Bottom) Residuals between the best fit result and the data. Note that the RMS value for fitting is as small as 0.027 mag.

determined using the color transformation between F555W − F814W and F606W − F814W shown in Section 2.3. The transformation was applied to seven galaxies that were observed with the F606W and F814W filters, excluding NGC 4258. Then we carried out multi-parameter fitting as done for F606W − F814W combination and obtained the values. In the fitting, we fixed $\gamma = 1.6$, which corresponds to [Fe/H] $= -1.6$. Conversion relations described in Sirianni et al. (2005) were used to obtain the parameters in three photometric systems: F555W−F814W and F606W−F814W combinations in WFPC2, and $V - I$ combination in the Johnson-Cousins system. Parameters for F555W−F814W and F606W−F814W combinations in WFC3/UVIS were derived by applying the photometric transformation between ACS/WFC to WFC3/UVIS described in Jang & Lee (2015). Transformation uncertainty, $0.01 \sim 0.02$ mag were added in each calculation. Derived values are summarized in Table 5.3.

We introduce the QT magnitude, a quadratic form of the TRGB magnitude corrected for the color dependence of the F814W (or I) magnitude TRGB, because the TRGB color magnitude relations for eight galaxies are fitted well by a quadratic equation, as in Figure 5.5. The QT is expressed by

$$QT = \mathrm{F814W}_0 - \alpha(\mathrm{Color} - \gamma)^2 - \beta(\mathrm{Color} - \gamma) \tag{5.4}$$

where $\alpha = 0.123 \pm 0.006$, $\beta = 0.042 \pm 0.014$, and $\gamma = 1.1$ in the F606W − F814W filter combination in ACS/WFC.

The TRGB magnitude of the QT system (QT_{RGB}) can be found by applying classical edge detection algorithm (Lee et al. 1993; Sakai et al. 1996; Méndez et al. 2002, etc), and corresponding distance modulus will be :

$$(m - M)_0 = QT_{RGB} + M_{QT,TRGB} \tag{5.5}$$

where $M_{F814W,TRGB}$ is an absolute magnitude of the TRGB in the QT system. The value of $M_{F814W,TRGB}$ will be addressed in the next Section.

5.3 Zero-point Calibration

5.3.1 NGC 4258 as a Distance Anchor

NGC 4258 is known to be a useful distance anchor because it hosts a water megamaser, which can be used as a powerful and precise geometric distance indicator. With monitoring observations of the nuclear water megamaser sources in NGC 4258, several geometric distance estimates were presented: Greenhill et al. (1995); Miyoshi et al. (1995); Herrnstein et al. (1999); Humphreys et al. (2005); Argon et al. (2007); Humphreys et al. (2008, 2013); Riess et al. (2016). Humphreys et al. (2013) reported a distance value of $d = 7.60 \pm 0.17_r \pm 0.15_s$ Mpc ($(m-M)_0 = 29.404 \pm 0.049_r \pm 0.043_s$), where errors with r and s represent random errors and systematic errors, respectively. It is slightly larger than the old value given by Herrnstein et al. (1999) ($d = 7.2 \pm 0.2_r \pm 0.5_s$ Mpc), which is similar to the value used in Riess et al. (2011); Riess et al. (2012) ($d = 7.28 \pm 0.22$ Mpc). Most recently, Riess et al. (2016) provided a similar value with smaller systematic uncertainty, d=7.54 $\pm$ 0.17$_r$ $\pm$ 0.10$_s$ Mpc ($(m-M)_0 = 29.387 \pm 0.049_r \pm 0.029_s$), by applying the Monte Carlo Markov Chain to the same VLBI data as used in Humphreys et al. (2013). We adopted the most recent distance estimate given by Riess et al. (2016) for the zero-point calibration of the TRGB in this study.

Mager et al. (2008) reported a TRGB distance to NGC 4258 based on photometry of the same HST images as used in this study. They carried out PSF photometry using two software tools, DOLPHOT (Dolphin 2000) and DAOPHOT, and derived a TRGB magnitude, $T_{RGB} = 25.24 \pm 0.04$ from DOLPHOT photometry. It is noted that they found $\sim$ 0.04 mag difference in the TRGB magnitude between the two data reduction methods.

We obtained a value for the TRGB magnitude in the QT system for NGC 4258 from photometry of ACS image data that we used for the color dependence calibration (Section 2). We also performed a test similar to the Mager et al. (2008)'s. We performed point source photometry based on five different techniques using dif-

ferent softwares and different image types: 1) DAOPHOT/ALLFRAME run on charge transfer efficiency (CTE) corrected drizzled images (indicated by _drc.fits), 2) IRAF/DAOPHOT run on the same _drc.fits images, 3) DAOPHOT/ALLFRAME run on CTE corrected and flat fielded images (indicated by _flc.fits), 4) DOLPHOT run on the same _flc.fits images, and 5) DOLPHOT run on CTE uncorrected and flat fielded images (indicated by _flt.fits). We used PSF images we derived using isolated bright stars (for DAOPHOT/ALLFRAME and IRAF/DAOPHOT reductions on drizzled images) or provided by the Tiny Tim (for DOLPHOT reductions). In the case of DAOPHOT/ALLFRAME photometry on individual _flc.fits images, we used PSF images constructed from the ACS images of 47 Tuc (Proposal IDs = 10737 for F555W and 10101 for F814W filters), because the number of bright stars in a single _flc.fits image of NGC 4258 is only a few. A single pass sequence of DAOFIND-PHOT-ALLSTAR/ALLFRAME routines was applied for the IRAF/DAOPHOT and ALLFRAME reductions. DOLPHOT reductions were done using the parameter set recommended by the DOLPHOT/ACS User's guide (version 2.0). We set the ACSuseCTE = 0 (CTE uncorrection mode) for _flc.fits and 1 (CTE correction mode) for _flt.fits in DOLPHOT reductions.

Figure 5.6 displays the magnitude differences between the results of the ALLFRAME (flc) reduction and those of other reductions. Comparisons of F555W band magnitudes (left panels) show small offsets. Mean offsets for the bright stars with F555W $\lesssim$ 27.0 are smaller than 0.05 mag. At the TRGB level, F555W $\sim$ 27.8 mag, mean offsets are estimated to be –0.004, –0.009, 0.045, and 0.060 mag for the IRAF/DAOPHOT (drc), ALLFRAME (flc), DOLPHOT (flc), and DOLPHOT (flt), respectively. Thus, three DAOPHOT reductions (ALLFRAME (drc), IRAF/DAOPHOT (drc), and ALLFRAME (flc)) agree well within 0.01 mag, but DOLPHOT reductions show $\sim$ 0.05 mag differences. Faint stars with F555W $\gtrsim$ 28.0 mag yield larger offsets, which increase as a function of magnitude. The origin of these magnitude differences is unclear. Although non-negligible offsets are detected at the faint levels ($F555W \gtrsim 28.0$), most of the RGB stars we used in

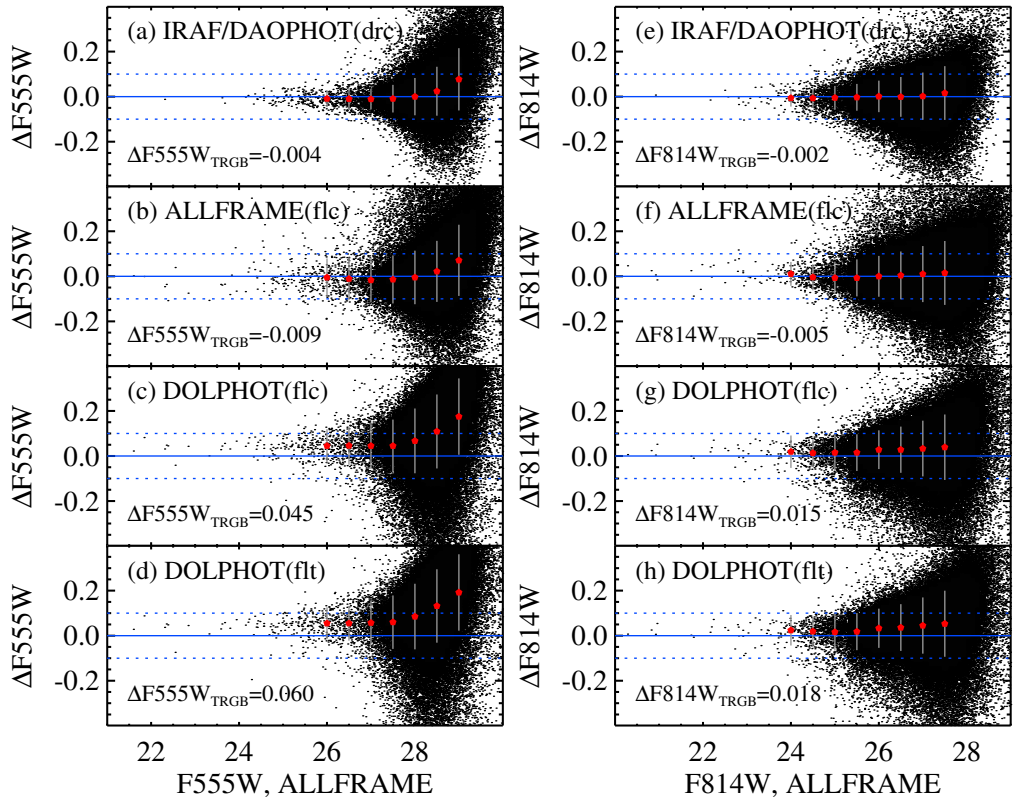

Figure 5.6: (a-d) Comparisons of PSF magnitudes in F555W band between ALLFRAME on drc reduction and IRAF/DAOPHOT on drc (a), ALLFRAME on flc (b), DOLPHOT on flc (c), and DOLPHOT on flt (d) reductions of NGC 4258. Red dots and error bars represent the mean magnitude offset and its standard deviation, respectively. Mean magnitude offsets at the TRGB level (F555W $\sim$ 28.0) are labeled in each panel. (e-h) Same as (a-d), except for F814W band. Note the mean magnitude offsets at the TRGB level (F814W $\sim$ 25.3) are very small, ΔF814W $\lesssim$ 0.02 mag.

the TRGB detection of NGC 4258 are brighter than F555W $\sim$ 28.0, where mean offsets are small enough. Moreover, $F555W$ band magnitudes are only used in the estimation of the TRGB color, which affects little in the QT magnitude estimation. Comparisons of F814W band magnitudes show much better agreements. All five reductions agree well within 0.02 mag from the bright to the faint magnitude range ($21.0 \lesssim$ F814W $\lesssim 27.5$ mag).

In Figure 5.7 we compare $QT - (\mathrm{F555W} - \mathrm{F814W})_0$ CMDs from five different reductions. All five CMDs show strong and sharp edge detection responses at $QT \sim 27.3$, which represents clearly a TRGB. They show also weaker and broader response peaks at $QT \sim 26.7$, which are far from being the TRGBs. ALLFRAME reductions (drc and flc) show sharper responses at $QT \sim 27.3$ than that of IRAF/DAOPHOT (drc). DOLPHOT reductions show two peaks at $QT \sim 27.3$ and 27.4. We selected a stronger one, at $QT \sim 27.3$ as the TRGB. Precise TRGB magnitudes and uncertainties are obtained using the bootstrap method as done in Jang & Lee (2015): $QT = 25.272 \pm 0.014, 25.284 \pm 0.033, 25.289 \pm 0.015, 25.260 \pm 0.014, 25.258 \pm 0.019$ mag for ALLFRAME(drc), IRAF/DAOPHOT (drc), ALLFRAME (flc), DOLPHOT (flc), and DOLPHOT(flt), respectively. These estimations yield a mean of $QT = 25.273$ mag, median of $QT = 25.272$ mag, and standard deviation of 0.014 mag, which is very small. Thus our TRGB estimation is robust. Software-dependent uncertainties in the TRGB detection are estimated to be smaller than 0.02 mag.

We used the TRGB magnitude from the ALLFRAME (drc) reduction, $QT = 25.272 \pm 0.014$, for the zero-point calibration of the TRGB. From this value and the distance modulus given by Riess et al. (2016), we obtain $M_{\mathrm{F814W,TRGB}} = QT_{RGB} - (m - M)_0 = 25.272 - 29.387 = -4.115$ mag with an uncertainty of 0.060 mag. Its uncertainty, 0.060 mag, is obtained from the quadratic sum of individual uncertainties: extinction correction error (0.003 mag, 10% of F814W band extinction), TRGB detection error (0.014 mag), photometric zero-point error (0.015 mag), and NGC 4258 distance error (0.057 mag). Thus the systematic uncertainty is dominated by the NGC 4258 distance error.

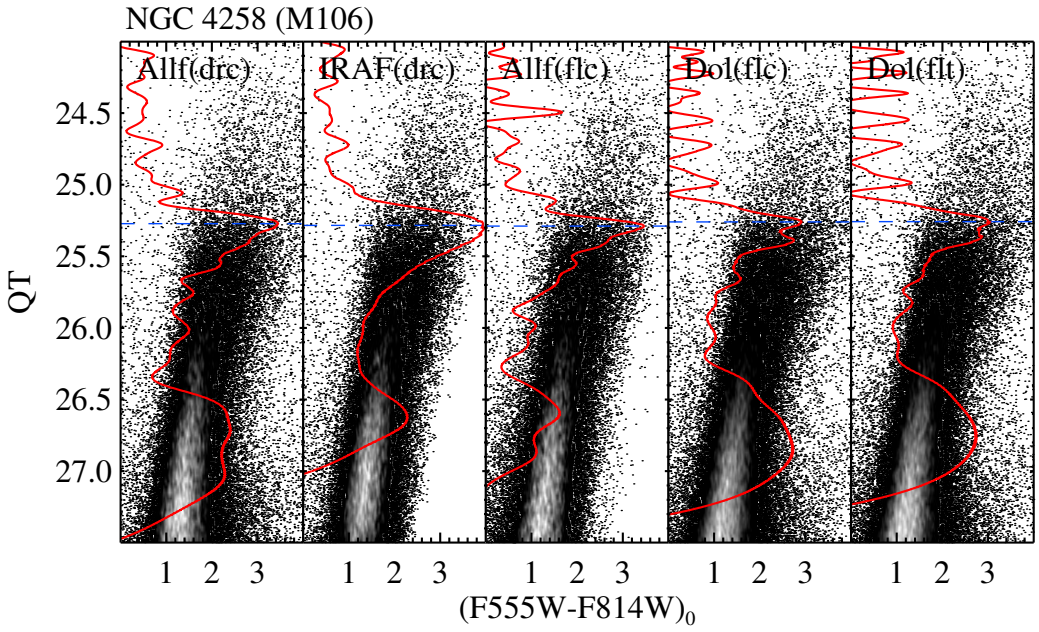

Figure 5.7: $QT - (\mathrm{F555W} - \mathrm{F814W})_0$ CMDs of NGC 4258 from five different reduction methods : ALLFRAME on drc, IRAF/DAOPHOT on drc, ALLFRAME on flc, DOLPHOT on flc, and DOLPHOT on flt (from left to right). Edge detection responses are shown by the solid lines. Note that the estimated TRGB magnitudes agree very well.

5.3.2 The Large Magellanic Cloud as a Distance Anchor

The LMC has been often used as a distance anchor for extragalactic distance indicators (Freedman & Madore 2010; de Grijs et al. 2014). Its distance has long been controversial from $(m-M)_0 = 18.1$ to 18.8, and it appeared to settle down with a value of $(m-M)_0 \sim 18.50 \pm 0.10$, after the results of the Hubble Key Project (Freedman et al. 2001) were published. However, it has been suspected that the tight correlation of the LMC distance estimates might have been affected by the publication bias or the bandwagon effect (Schaefer 2008; de Grijs et al. 2014). This problem can be resolved with more accurate distance estimates for the LMC in the future.

Recently Freedman et al. (2012) presented an updated distance estimate, $(m-M)_0 = 18.477 \pm 0.011_r \pm 0.033_s$, accurate to 1.7%, from the analysis of Spitzer $3.6\mu m$ photometry for 10 Cepheids in the Milky Way and 80 Cepheids in the LMC. On the other hand, Pietrzyński et al. (2013) analyzed eight eclipsing binary stars using the OGLE photometry, and yielded a distance value with a total uncertainty of 2.2%: $(m-M)_0 = 18.494 \pm 0.008_r \pm 0.048_s$ ($d = 49.97 \pm 0.19_r \pm 0.11_s$ kpc). These two recent estimates agree very well. We adopted the distance estimate by Pietrzyński et al. (2013) for the zero-point calibration of the TRGB, because we use the OGLE photometry of the LMC for the analysis of the TRGB in this study as follows.

We measured the TRGB magnitude of the LMC using the VI photometric catalog from the OGLE-III shallow survey (Ulaczyk et al. 2012). This catalog was made using the same telescope and the same CCD camera as used for the analysis of Pietrzyński et al. (2013). It offers benefits that any instrument-dependent uncertainties, which are hard to measure, can be ruled out in the zero point calibration of the TRGB. Figure 5.8 shows identifications of eight eclipsing binary stars used in Pietrzyński et al. (2013) (starlets) overlayed on a spatial number density map of bright RGB stars ($1.2 < V-I \leq 2.0$ and $14.4 < I \leq 16.0$) in the OGLE-III catalog. All eight binary stars are located on the western side from the LMC center (white cross). It is known that the distance measurement can be affected by

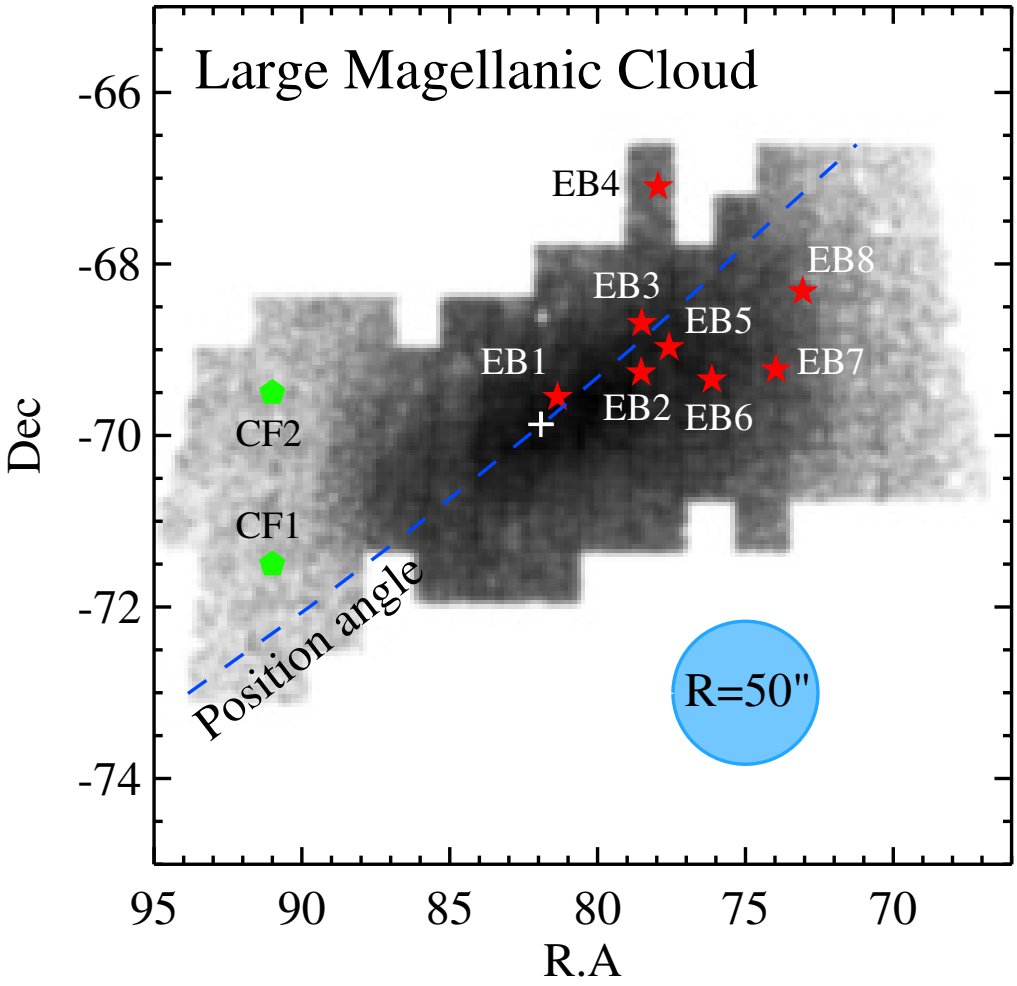

Figure 5.8: Identification of eight eclipsing binary stars (starlets) used in Pietrzyński et al. (2013), overlayed on a number density map of RGB stars in the LMC. Two control fields used in this study are marked by green pentagons. We investigated the TRGB magnitude of the LMC using the stars at $R \leq 50''$ region of each eclipsing binary star and each control field.

the geometry and the depth of the LMC. For this reason, Pietrzyński et al. (2013) applied additional geometry correction to their distance estimation. However, they concluded that the effect of this correction to the distance measurement is negligible. For the analysis of the TRGB for the LMC we selected eight fields located around the eclipsing binary stars used in Pietrzyński et al. (2013), and used the stars at $R \leq 50''$ region around each eclipsing binary star. We investigated also two additional fields, control field 1 and 2 (pentagons), covering the eastern side of the LMC as a reference.

In Figure 5.9, we plotted the extinction corrected $QT - (V-I)_0$ CMDs of eight fields around eclipsing binary stars (a-h) and two control fields (i, j). The extinction correction was done using the extinction map of the LMC given by Haschke et al. (2011), who estimated the extinction values from the mean color of red clump stars in the OGLE-III photometry. It is noted that we used the same extinction map as applied in Pietrzyński et al. (2013). All ten CMDs show various populations of stars including young main sequence stars (a vertical feature at $(V-I)_0 \sim 0.2$), blue and red helium burning stars (vertical and slanted features at $(V-I)_0 \sim 0.1$ and 1.2, respectively), old RGB stars (a dominant broad slanted feature at $(V-I)_0 \sim 1.8$) and AGB stars (a broad slanted feature above the RGB) in the LMC. The Milky Way foreground stars are also seen (vertical feature at $(V-I)_0 \sim 0.7$). We measured the TRGB using the stars located in the shaded regions in Figure 5.9, which were designed to avoid young stellar populations and to sample RGB stars as many as possible. We plotted the edge detection responses as curved lines in each panel. All ten CMDs show strong peaks at $QT \sim 14.48$. We obtained quantitative values of the TRGB magnitudes and corresponding errors from the bootstrap resampling of ten thousand simulations and summarized the values in Table 5.2.

Figure 5.10 shows a comparison of the TRGB magnitudes of eight eclipsing binary fields (starlets) and two control fields (pentagons) in the LMC. We corrected geometric distortion of the LMC by assuming the LMC disk with an inclination angle of 28° and a position angle of 128°, as assumed in Pietrzyński et al. (2013).

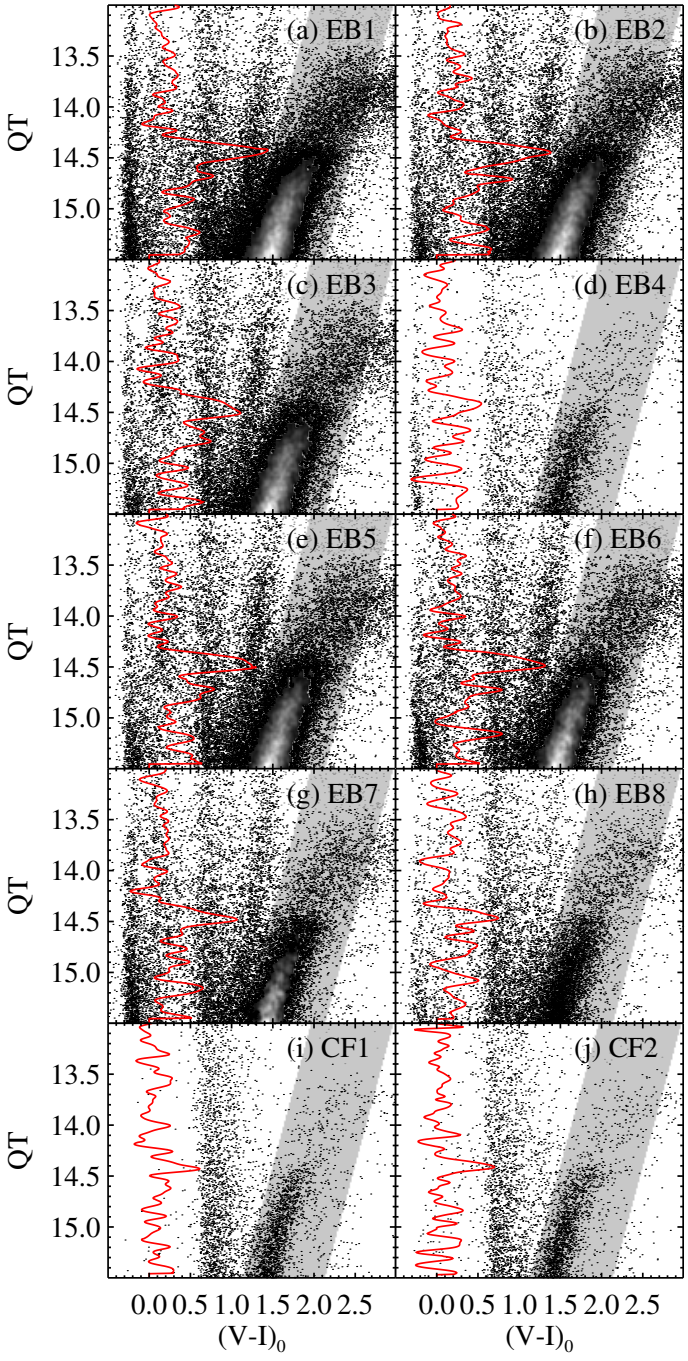

Figure 5.9: $QT - (V - I)_0$ CMDs of resolved stars in $R \leq 50''$ regions of eclipsing binary stars (a-h) and control fields (i-j). Shaded regions indicate the area we used to sample the RGB stars for the TRGB analysis. Edge detection responses are shown by the solid lines.

Table 5.2. A Summary of the TRGB Magnitudes of the LMC

Field	R.A.	Decl	QT (Measured)	QT (Distortion corrected)
EB1	05 25 25.550	-69 33 04.39	14.425 ± 0.014	14.429 ± 0.014
EB2	05 14 05.952	-69 15 56.83	14.445 ± 0.011	14.441 ± 0.011
EB3	05 14 01.908	-68 41 18.41	14.505 ± 0.010	14.501 ± 0.010
EB4	05 11 49.458	-67 05 45.19	14.415 ± 0.020	14.441 ± 0.020
EB5	05 10 19.650	-68 58 12.00	14.485 ± 0.012	14.481 ± 0.012
EB6	05 04 32.882	-69 20 50.99	14.485 ± 0.012	14.469 ± 0.012
EB7	04 55 51.491	-69 13 47.99	14.475 ± 0.010	14.451 ± 0.010
EB8	04 52 15.280	-68 19 10.30	14.465 ± 0.010	14.450 ± 0.010
CF1	06 04 00.000	-71 30 00.00	14.428 ± 0.009	14.443 ± 0.009
CF2	06 04 00.000	-69 30 00.00	14.411 ± 0.013	14.458 ± 0.013
Weighted mean of EB1-8 and CF1-2			14.459 ± 0.004 (0.033)[a]	14.458 ± 0.004 (0.022)
Weighted mean of CF1-2			14.423 ± 0.007 (0.012)	14.448 ± 0.007 (0.011)
Weighted mean of EB1-8			14.470 ± 0.004 (0.032)	14.461 ± 0.004 (0.024)

[a]Standard deviation.

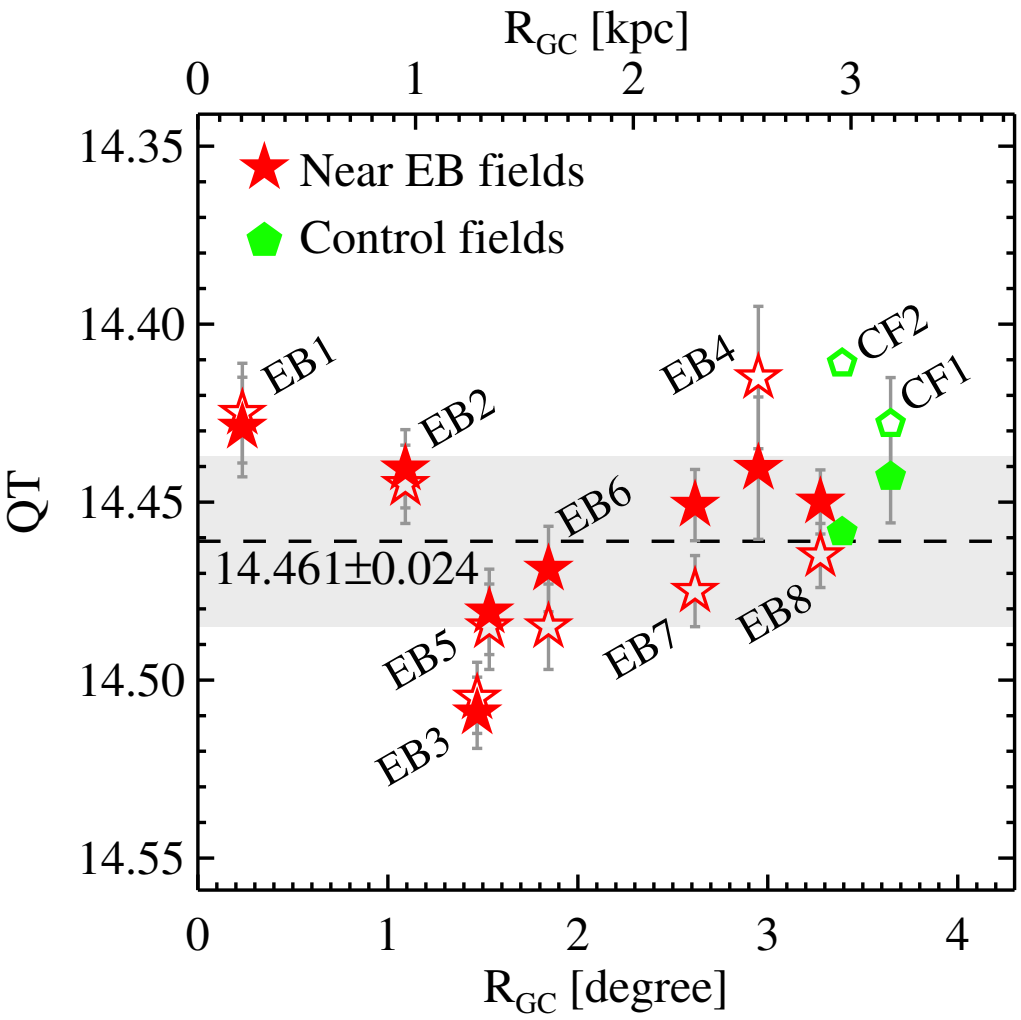

Figure 5.10: Comparison of the TRGB magnitudes from the fields around eclipsing binary stars (starlets) and from the control fields (pentagons) vs. galactocentric radius of the LMC. The open and filled symbols denote the TRGB magnitudes before and after geometric distortion correction, respectively. The mean TRGB magnitude of eight eclipsing binary fields, corrected for the geometric distortion (filled stars), is estimated to be $QT = 14.461 \pm 0.004$ with a standard deviation of 0.024 mag (dashed line with shades).

We plotted the TRGB magnitudes before and after correction of geometric distortion in Figure 5.10 by open and filled symbols. The TRGB magnitudes are ranging from $QT \approx 14.41$ to 14.51 mag. A weighted mean value of the TRGB magnitudes of all ten fields is $QT = 14.459 \pm 0.004$ mag with a standard deviation of 0.033 mag. Similar values of $QT = 14.470 \pm 0.004$ mag and $QT = 14.423 \pm 0.007$ mag are derived from the eight eclipsing binary fields and two control fields, respectively. Distortion correction contributes a very small change to the TRGB magnitudes: 0.001 mag for all ten fields, 0.025 mag for two control fields, and 0.009 mag for eight eclipsing binary fields. Thus geometric distortion of the LMC is not significant in the TRGB magnitude estimation in this study.

We adopted the distortion corrected mean TRGB magnitude of eight eclipsing binary fields, $QT = 14.461$ mag, as a mean value for TRGB magnitude of the LMC. A conservative error, 0.024 mag, which is a standard deviation of these fields, is adopted as the measurement error. Finally we obtain $M_{I,TRGB} = QT_{RGB} - (m - M)_0 = 14.461 - 18.494 = -4.033$ mag with an uncertainty of 0.063 mag. Quoted uncertainty, 0.063 mag, is derived in the same way as done for the zero point calibration using NGC 4258: extinction correction error (0.011 mag), TRGB detection error (0.024 mag), photometric zero-point error (0.03 mag), and the LMC distance error (0.049 mag).

5.4 Summary of the Revised TRGB Calibration

In Table 5.3, we summarize the revised TRGB calibration in various photometric systems. Color dependence correction terms (α, β, and γ) in these photometric systems were determined by applying the photometric transformation as described in Section 2. The same method was applied to obtain the zero-point values in each photometric system. The zero-points from NGC 4258 and the LMC show a systematic offset of ~ 0.1 mag. A weighted mean of the zero-points from NGC 4258 and the LMC yields $M_{I,TRGB} = -4.074 \pm 0.046$ in the I-band. This value is similar

to the values given in previous calibrations, $M_{I,TRGB} = -4.05 \pm 0.12$ (Bellazzini et al. 2001, 2004; Rizzi et al. 2007; Madore et al. 2009), but its quoted error is 2.6 times smaller.

Table 5.3. A Summary of the TRGB Calibrations in This Study

System	*Color*	α	β	γ	Zero-point		
		$QT = I_0 - \alpha(Color - \gamma)^2 - \beta(Color - \gamma)$			NGC 4258	LMC	NGC 4258 + LMC
ACS/WFC	$(\mathrm{F606W} - \mathrm{F814W})_0$	0.123 ± 0.006	0.042 ± 0.014	1.1	-4.119 ± 0.060	-4.031 ± 0.070	-4.082 ± 0.046
ACS/WFC	$(\mathrm{F555W} - \mathrm{F814W})_0$	0.093 ± 0.005	0.024 ± 0.013	1.6	-4.115 ± 0.060	-4.027 ± 0.070	-4.078 ± 0.046
J.C.	$(V - I)_0$	0.073 ± 0.004	0.047 ± 0.010	1.5	-4.121 ± 0.067	-4.033 ± 0.063	-4.074 ± 0.046
WFC3/UVIS	$(\mathrm{F606W} - \mathrm{F814W})_0$	0.119 ± 0.006	0.033 ± 0.015	1.1	-4.129 ± 0.061	-4.041 ± 0.071	-4.092 ± 0.047
WFC3/UVIS	$(\mathrm{F555W} - \mathrm{F814W})_0$	0.091 ± 0.004	0.021 ± 0.012	1.6	-4.124 ± 0.061	-4.036 ± 0.071	-4.087 ± 0.047
WFPC2	$(\mathrm{F606W} - \mathrm{F814W})_0$	0.142 ± 0.007	0.051 ± 0.016	1.0	-4.090 ± 0.121	-4.002 ± 0.126	-4.048 ± 0.115
WFPC2	$(\mathrm{F555W} - \mathrm{F814W})_0$	0.099 ± 0.005	0.020 ± 0.012	1.5	-4.112 ± 0.062	-4.024 ± 0.072	-4.075 ± 0.049

5.5 Discussion

5.5.1 Comparison with Previous TRGB Calibrations

There have been several studies of the TRGB calibration including both color-magnitude dependence and zero-point calibrations as summarized in Table 5.4. Da Costa & Armandroff (1990) provided the bolometric magnitude and bolometric correction of the TRGB as a function of metallicity and color, based on VI photometry of six globular clusters in the Milky Way. With these relations, Lee et al. (1993) estimated the absolute I-band magnitude of the TRGB, $M_{I,TRGB} = -4.0 \pm 0.1$ mag, for metal poor stellar systems ([Fe/H] < -0.7). Salaris & Cassisi (1997) derived a TRGB calibration having quadratic terms of metallicity from their theoretical stellar models. Absolute I-band magnitude of the TRGB at the fiducial metallicity, [M/H] $= -1.2$, is estimated to be -4.16 mag, slightly brighter than that of Lee et al. (1993). This discrepancy is coming from the different estimation of the TRGB bolometric luminosity (Ferrarese et al. 2000). Ferrarese et al. (2000) calibrated the TRGB luminosity from the Cepheid distance estimations of nine galaxies in the Local Group. Absolute I-band magnitudes of the TRGB, -3.99 and -4.06 mag with an uncertainty of ~ 0.15 mag, were derived depending on the adoption of metallicity dependence of Cepheid variables ($\gamma = \delta(m - M)_0/\delta$[O/H] $= 0.00$ and –0.24, respectively).

Later Bellazzini et al. (2001, 2004) and Bellazzini (2008) presented another set of the TRGB calibration based on the larger sample of the Milky Way globular clusters: $M_{\rm bol,TRGB} = -0.12$[Fe/H] $- 3.76$ and $M_{\rm I,TRGB} = 0.14$[Fe/H]$^2 + 0.48$[Fe/H] $- 3.66$. Bellazzini et al. (2001) also presented another calibration based on ω Centauri for which a direct distance estimate based on one eclipsing binary star (Thompson et al. 2001) is available. Adopting a metallicity of [Fe/H]$= -1.7$ for ω Centauri, they derived $M_{\rm I,TRGB} = -4.04 \pm 0.12$ where the error is dominated by the distance measurement error for ω Centauri. This error has been used a value for the systematic error for the TRGB calibration (Mager et al. 2008; Conn et al. 2011; Shappee &

Table 5.4. A List of the Previous and Revised TRGB Calibrations

Reference	Calibration	Zero-point $M_{I,TRGB}$	Note
Lee et al. (1993)	-4.0 ± 0.1	-4.0 ± 0.1	MW GCs
Salaris & Cassisi (1997)	$-3.732 + 0.588[\mathrm{M/H}] + 0.193[\mathrm{M/H}]^2$	-4.16	$-2.35 \leq [\mathrm{M/H}] \leq -0.57$
Ferrarese et al. (2000)	$-4.06 \pm 0.07 \pm 0.13$	$-4.06 \pm 0.07 \pm 0.13$	Cepheids, $\gamma = 0.00$
Ferrarese et al. (2000)	$-3.99 \pm 0.07 \pm 0.13$	$-3.99 \pm 0.07 \pm 0.13$	Cepheids, $\gamma = -0.24$
Bellazzini et al. (2001)	$-3.66 + 0.48[\mathrm{Fe/H}] + 0.14[\mathrm{Fe/H}]^2$	-4.07 ± 0.12	[Fe/H] $= -1.6$, E.B, ω Cen
Bellazzini et al. (2004)	$-3.629 + 0.679[\mathrm{M/H}] + 0.258[\mathrm{M/H}]^2$	-4.07 ± 0.12	[M/H] $= -1.2$, E.B, ω Cen
Rizzi et al. (2007)	$-4.05 + 0.217[(V-I)_0 - 1.6]$	-4.07	Six galaxies
Bellazzini (2008)	$-3.939 - 0.194(V-I)_0 + 0.080(V-I)_0^2$	-4.05	
Tammann et al. (2008)	$-4.05 \pm 0.02 \pm 0.10$	$-4.05 \pm 0.02 \pm 0.10$	RR Lyrae, LMC scale
Madore et al. (2009)	$-4.05 + 0.2[(V-I)_0 - 1.5]$	-4.05	T magnitude
Fusco et al. (2012)	$-3.63 - 0.40Col^a + 0.08Col^2$	-4.13 ± 0.01	F814W, model
This study	$-4.074 + 0.073((V-I)_0 - 1.5)^2 + 0.047((V-I)_0 - 1.5)$	-4.074 ± 0.046	NGC 4258 and the LMC

[a]Col $= (\mathrm{F475W} - \mathrm{F814W})_0$.

Stanek 2011; Lee & Jang 2012, 2013; Jang & Lee 2014, 2015; Lee & Jang 2016). This value of the calibration is consistent with that from the quadratic calibration for [Fe/H] $= -1.7$ in this study, $M_{\rm I,TRGB} = -4.07$.

On the other hand Rizzi et al. (2007) provided a linear color dependence of the TRGB from the analysis of HST photometry data for six nearby galaxies: $M_{I,TRGB} = -4.05 + 0.217[(V-I)_0 - 1.6]$. They constrained the zero-point by using five Local Group galaxies, whose distances are obtained from the horizontal branch stars. Adopting the calibration of the horizontal branch stars given by Carretta et al. (2000), they derived a zero-point value, -4.05 ± 0.02 mag at a fiducial color, $(V-I)_0 = 1.6$ (corresponding to [Fe/H] $= -1.5$). The systematic error of this value is mainly due to the uncertainty in the mean absolute magnitude of the horizontal branch stars, which is ~ 0.1 mag (Carretta et al. 2000).

Tammann et al. (2008) compiled the data for 24 galaxies that have estimates for both the TRGB magnitudes and the RR Lyrae distances in the literature, and derived an absolute magnitude of the TRGB, $M_{I,TRGB} = -4.05$ mag with a mean error of 0.02 mag. The systematic error of this value is mainly due to the uncertainty in the mean magnitude of the RR Lyrae, which is ~ 0.1 mag (Popowski & Gould 1998a,b).

Madore et al. (2009) described a novel approach for robust determination of the TRGB magnitude by introducing a new magnitude system, T magnitude, which is a color (metallicity) corrected I-band magnitude: $T = I_0 - \beta((V-I)_0 - 1.5)$. They adopted a value for the slope, $\beta = 0.20 \pm 0.05$ for $1.5 < (V-I)_0 < 3.0$, from a linear approximation of the color-luminosity relation given by Bellazzini et al. (2001, 2004). They showed that the T magnitude works well in the case of NGC 4258 (Mager et al. 2008; Madore et al. 2009).

Recently Fusco et al. (2012) carried out a TRGB calibration with the BaSTI stellar models (Pietrinferni et al. 2004, 2006), updating the conductive opacity evaluations provided by Cassisi et al. (2007). They presented variations of the TRGB magnitude as a function of metallicity and F475W $-$ F814W color in their Fig-

ure 4. At the fiducial metallicity ([Fe/H]= -1.6), their calibration yields a value, $M_{\rm F814W,TRGB} = -4.13$, which is slightly brighter than other calibrations.

In Figure 5.11, we compare our TRGB calibration with the previous ones in the $M_I - (V-I)_0$ domain. In the figure we set line lengths to be consistent with the color range used for each TRGB calibration. In the upper axis of the figure we also marked the metallicity values of the TRGB using the relation between $(V-I)_0$ and [Fe/H] for [Fe/H]< -0.7, given by Bellazzini et al. (2001) ($(V-I)_{0,TRGB} = 0.581[{\rm Fe/H}]^2 + 2.742[{\rm Fe/H}] + 4.013$). Several important features are seen in this figure. First, the revised TRGB calibration derived in this study (red line) covers a much wider color range, $1.2 \lesssim (V-I)_0 \lesssim 4.3$, than other calibrations. Second, our TRGB calibration shows a color-magnitude relation that is relatively flat at the blue end and steep at the red color range. Some of the previous calibrations adopted either a flat relation (Lee et al. 1993; Ferrarese et al. 2000; Tammann et al. 2008) or color-dependent relations (Madore et al. 2009; Rizzi et al. 2007; Salaris & Cassisi 1997). Third, the color dependence at the color range of $2.0 \lesssim (V-I)_0 \lesssim 3.0$ derived in this study is similar to the results given by Salaris & Cassisi (1997), Madore et al. (2009), Rizzi et al. (2007), and Bellazzini (2008). Fourth, our calibration shows excellent agreement with the calibration given by Bellazzini et al. (2001) in the color range of $(V-I)_0 \leq 2.5$, except for ~ 0.03 mag zero-point offset. It is encouraging that the color magnitude relation of the TRGB from simple stellar populations in the Milky Way galaxy and those from nearby galaxies with multiple stellar populations show good agreement. Fifth, our calibration shows an absolute magnitude of the TRGB, $M_I = -4.074 \pm 0.046$, at a fiducial color, $(V-I)_0 = 1.5$. It agrees well with the values from all of the previous calibrations within uncertainties.

Figure 5.12 shows the propagation of the zero-point uncertainties in the previous calibration based on ω Centauri (circles, Bellazzini et al. (2001)) and the revised calibrations based on NGC 4258 and the LMC in this study (triangles and squares). We consider four sources of uncertainties: extinction, TRGB detection, photometric zero-point, and distance anchor uncertainties. We calculated cumulative errors of

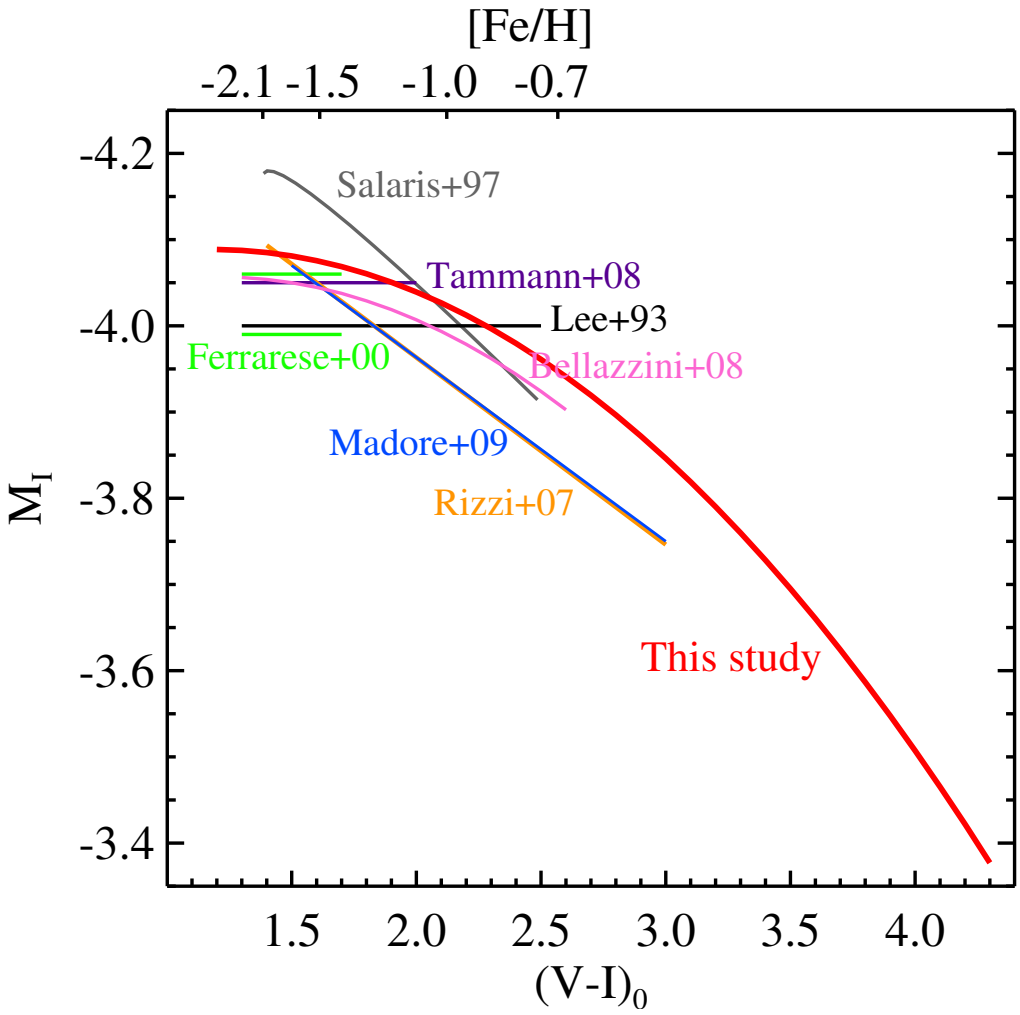

Figure 5.11: Comparison of the TRGB calibrations in $M_I - (V-I)_0$ domain in this study and the previous studies (Lee et al. 1993; Salaris & Cassisi 1997; Ferrarese et al. 2000; Rizzi et al. 2007; Bellazzini 2008; Tammann et al. 2008; Madore et al. 2009).

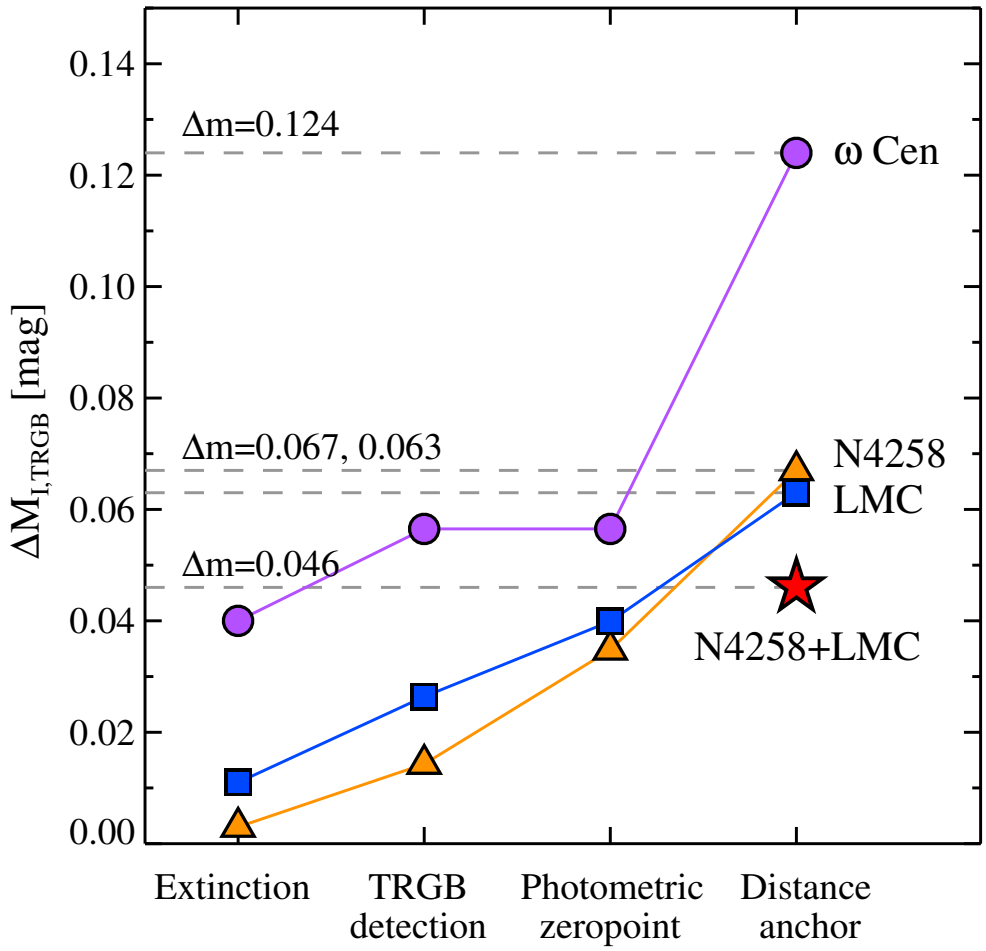

Figure 5.12: Propagation of uncertainties in the zero-point calibration of the TRGB. Note that the previous calibration based on ω Centauri gives a zero-point uncertainty of 0.124 mag (Bellazzini et al. 2001, 2004). When NGC 4258 and LMC are used as a distance anchor, uncertainties are estimated to be 0.067 and 0.063 mag, respectively. Combining these two anchors (NGC 4258 and LMC) provides the most accurate calibration with an uncertainty of 0.046 mag (red starlet), 62% smaller than the value given by Bellazzini et al. (2001, 2004).

each source (a quadratic sum of uncertainties including all the previous sources), according to this order. Bellazzini et al. (2001, 2004) presented a luminosity calibration of the TRGB based on the distance to ω Centauri, and derived a total uncertainty, 0.124 mag from the quadratic sum of three uncertainties: 0.04, 0.04, and 0.11 mag for extinction, TRGB detection, and distance anchor uncertainties, respectively. They did not provide any uncertainty for the photometric zero-point. On the other hand, the revised TRGB calibration in this study yields total systematic uncertainty of 0.060 mag from NGC 4258 and 0.063 mag from the LMC as described in Section 3. A weighted mean of these two calibrations gives systematic uncertainty of 0.046 mag, which is about one third of the uncertainty given by Bellazzini et al. (2001, 2004). This value represents the systematic error of the revised TRGB calibration in this study.

5.5.2 Comparison with Stellar Isochrones

In Figure 5.13 we compare the empirical calibration of the TRGB (solid line with shaded region) derived in this study with the TRGB from three theoretical stellar models: Dartmouth (Dotter et al. 2008) (dashed line), BasTI (Pietrinferni et al. 2004, 2006) (dot-dashed line) , and Padova (Girardi et al. 2000; Marigo et al. 2008) (solid line). We set age of 12 Gyr and metallicity range of [M/H] = –2.2 to +0.2 for stellar models. A fixed alpha element abundance, $[\alpha/Fe] = +0.2$, was adopted for the Dartmouth model.

A few notable features are seen in this figure. First, the blue color range ($(\mathrm{F606W} - \mathrm{F814W})_0 \lesssim 1.6$) of the empirical calibration shows a good agreement with those of the Dartmouth and Padova models. In the case of the BasTI model, however, it shows 0.05 $\sim$ 0.10 mag systematic offset and is steeper than those of other calibrations. Second, all four calibrations show a good agreement at $(\mathrm{F606W} - \mathrm{F814W})_0 \sim 2.0$, which corresponds to [M/H]~ -0.5. Third, a significant dispersion is seen at the red color range ($(\mathrm{F606W} - \mathrm{F814W})_0 \gtrsim 2.7$). The BasTI model gives relatively bright TRGB luminosity and a shallower color dependence. Dartmouth

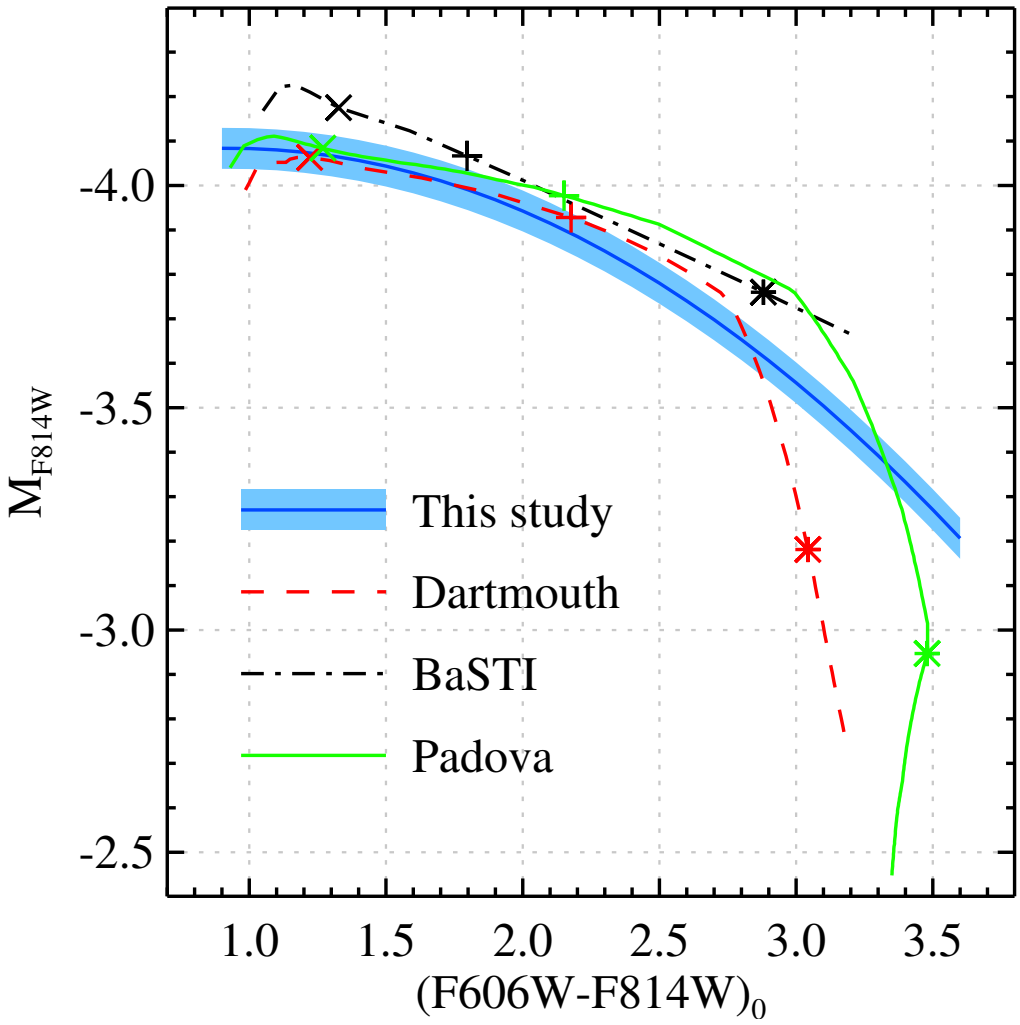

Figure 5.13: Comparison of the revised TRGB calibration (blue solid line with shaded region) with the TRGB from 12 Gyr stellar models: Dartmouth (Dotter et al. 2008) (red dashed line), BasTI (Pietrinferni et al. 2004, 2006) (black dot-dashed line), and Padova (Girardi et al. 2000; Marigo et al. 2008) (green solid line). Cross, plus, and asterisk symbols in each stellar model indicate [M/H]$= -1.0, -0.5$, and 0.0, respectively. The shaded region indicates a zero-point uncertainty, 0.046 mag, in this study.

and Padova models show much steeper than others. Our empirical calibration of the TRGB will be very useful for improving the modelling of stellar evolution in the future.

5.5.3 Implications on the Distance Scale and the Hubble Constant

We obtained the zero-point of the TRGB, $M_{I,TRGB} = -4.121 \pm 0.067$ from NGC 4258 and $M_{I,TRGB} = -4.033 \pm 0.063$ from the LMC. The zero-point difference is $\Delta M_{I,TRGB} = -0.088 \pm 0.092$. Thus, the two zero-point values agree within an uncertainty. From the TRGB magnitudes of NGC 4258 and the LMC, the distance modulus difference between two galaxies is obtained, $\Delta(m-M)_0 = 10.805 \pm 0.045$. It is slightly smaller than, but still agree within an uncertainty with the value from the Cepheid variables, $\Delta(m-M)_0 = 10.88 \pm 0.04_r \pm 0.05_s$ (Macri et al. 2006). If we adopt the TRGB zero-point from the LMC, the TRGB distance to NGC 4258 is estimated to be $(m-M)_0 = 29.299 \pm 0.021_r \pm 0.070_s$, consistent with the old megamaser distance to NGC 4258, $(m-M)_0 = 29.29 \pm 0.049_r \pm 0.043_s$ (Herrnstein et al. 1999), and slightly smaller than, but agrees within the errors with the updated megamaser distance, $(m-M)_0 = 29.404 \pm 0.049_r \pm 0.043_s$ (Humphreys et al. 2013) and $(m-M)_0 = 29.387 \pm 0.049_r \pm 0.029_s$ (Riess et al. 2016).

The revised TRGB calibration derived in this study enables to determine more precise TRGB distances to nearby galaxies and a corresponding value of the Hubble constant. There have been several studies to determine the Hubble constant based on the TRGB (Ferrarese et al. 2000; Mould & Sakai 2009a,b; Tammann et al. 2008; Hislop et al. 2011; Lee & Jang 2012; Tammann & Reindl 2013; Lee & Jang 2013; Jang & Lee 2015). Most of these studies were based on the zero-point of the TRGB, $M_I = -4.00 \sim -4.05$ mag with a systematic uncertainty of $0.10 \sim 0.12$ mag. The revised TRGB calibration combined with both NGC 4258 and LMC anchors yields a TRGB zero-point of $M_I = -4.074 \pm 0.046$ mag, slightly brighter and much more accurate than those of previous calibrations. Thus, the value of the Hubble constant derived in the previous studies can be slightly decreased if the revised

TRGB calibration is used.

Our previous studies, Lee & Jang (2012, 2013) and Jang & Lee (2015), presented a value of the Hubble constant, $H_0 = 69.8 \pm 2.6$(random) ± 3.9(systematic) km s^{-1} Mpc^{-1} and $H_0 = 72.2 \pm 3.3$(random) ± 4.0(systematic) km s^{-1} Mpc^{-1} based on five and three TRGB calibrated SNe Ia. In these studies we used the old TRGB calibration given by Rizzi et al. (2007) and the systematic error of 0.12 mag given by Bellazzini et al. (2001). If we apply the revised TRGB calibration including the QT magnitude and updated zero-point ($M_{I,TRGB} = -4.074 \pm 0.046$ mag), then the value of H_0 would be decreased by ~ 1 km s^{-1} Mpc^{-1} and the systematic uncertainty would be decreased by a factor of 2.6. A detailed analysis of the TRGB distances to eight SN Ia host galaxies and the Hubble constant based on this new calibration will be presented in our upcoming paper (Jang&Lee 2016, in preparation).

5.6 Summary and Conclusion

The TRGB has been used as a reliable distance indicator for resolved stellar systems. However, its calibration needs to be improved to derive more precise distances to nearby galaxies and corresponding value of the Hubble constant. We present a revised TRGB calibration including the color dependence and zero-point calibrations, accurate to 0.046 mag (2.3% of distance). Primary results are as follows.

- We obtained deep photometry of the resolved stars in eight nearby galaxies from the archival HST/ACS images. By applying quantitative TRGB detections on F814W $-$ (F606W $-$ F814W)$_0$ CMDs, we derived color-luminosity relation of the TRGB, which is described by a quadratic equation.

- From the photometry of two nearby globular clusters (NGC 2419 and 47 Tuc), we derived color transformation between F555W $-$ F814W and F606W $-$ F814W in ACS/WFC system.

- The zero-point of the TRGB was determined from the photometry of two

nearby galaxies, NGC 4258 and the LMC, to which geometric distances are known.

- We carried out PSF photometry using five different reduction methods on the HST/ACS field of NGC 4258 and compared the results. We found that output magnitudes agree well within 0.06 mag at the TRGB magnitude level. Especially, F814W band photometry shows excellent agreement within 0.02 mag, regardless of reduction methods.
- We provide the revised TRGB calibration in several filter systems including Johnson-Cousins, ACS/WFC, WFC3/UVIS, and WFPC2, as listed in Table 5.3.

This Chapter has been submitted to *The Astrophysical Journal* as Jang & Lee 2016. 133.

Chapter 6

The TRGB Distances to SN Ia Host Galaxies. V. NGC 3021, NGC 3370 and NGC 1309

6.1 Introduction

Measuring the value of the Hubble constant (H_0) is a fundamental step in extragalactic astronomy and cosmology. A tremendous work has been conducted over the past few decades to accurately determine the value of the Hubble constant. However, the estimated values have been controversial until recently. In the 20th century, two groups led by Allan Sandage and Gerard de Vaucouleurs, respectively, measured the value of the Hubble constant to be between H_0= 50 and 100 km s^{-1} Mpc^{-1}(de Vaucouleurs & Peters 1981; de Vaucouleurs 1993; Sandage & Tammann 1974a,b,c,d, 1975a,b, 1976; van den Bergh 1960a,b, 1975, 1994). This was known as "the factor of two controversy". Although it is not clear that this large discrepancy of H_0 originated from a purely scientific result or from a publication bias, the value of H_0 has settled down to a value between the two, $H_0 \sim 70$ km s^{-1} Mpc^{-1}, with the advent of the *Hubble Space Telescope* (HST).

The Hubble Key Project played a key role for the calibration of H_0 (Freedman et al. 2001). They improved the luminosity of SNe Ia with the HST and yielded a value of $H_0 = 71 \pm 2(\text{random}) \pm 6(\text{systematic})$ km s^{-1} Mpc^{-1}. A few years later, however, the SN HST project presented a somewhat lower value, $H_0 = 62.3 \pm 1.3(\text{random}) \pm 5.0(\text{systematic})$ km s^{-1} Mpc^{-1} (Sandage et al. 2006) from nearly the same HST imaging data as used in the Hubble Key Project. The level of difference is $\sim 1.5\sigma$. Recent estimations by the Supernovae and H0 for the Equation of State (SH0ES) and the Carnegie Hubble Program provided more precise values: $H_0 = 73.8 \pm 2.4$ km s^{-1} Mpc^{-1} (Riess et al. 2011), $H_0 = 73.02 \pm 1.79$ km s^{-1} Mpc^{-1} (Riess et al. 2016), and $H_0 = 74.3 \pm 2.1$ km s^{-1} Mpc^{-1} (Freedman et al. 2012), respectively. These three estimations that are based on Cepheid calibrated SNe Ia agree remarkably well.

However, the value of H_0 is still considered to be controversial. Recent analysis of the cosmic microwave background radiation (CMBR) with a flat ΛCDM cosmology by WMAP and PLANCK groups yielded values of H_0 with remarkably small uncertainties: $H_0 = 69.3 \pm 0.8$ km s^{-1} Mpc^{-1} from WMAP9 (Bennett et al. 2013) and $H_0 = 67.8 \pm 0.9$ km s^{-1} Mpc^{-1} from PLANCK (Planck Collaboration et al. 2015), which are lower than the values based on Cepheid calibrated SNe. Moreover, recent studies of the baryon acoustic oscillation (BAO) combined with SNe Ia data yielded a value similar to those from the CMBR analysis, $H_0 = 67.3 \pm 1.1$ km s^{-1} Mpc^{-1} (Aubourg et al. 2015). These three estimations agree well. However, these values are $2 \sim 3\sigma$ smaller than those from Cepheid calibrated SNe Ia. Note that CMBR and BAO are inverse distance ladders, while Cepheids and SN Ia are classical distance ladders. This discrepancy between the results based on the inverse distance ladder method and the classical distance latter method is now one of the critical issues in modern cosmology. It is needed to check systematics of both the classical and inverse distance ladder methods in order to understand what may cause this discrepancy.

We have been working to improve the measurement of H_0 by measuring the accurate luminosity of SN Ia based on the Tip of the Red Giant Branch (TRGB),

as part of the program, the TRGB distances to SN host galaxies in the Universe (TIPSNU). The TRGB is known as a precise population II distance indicator (Lee et al. 1993; Freedman & Madore 2010; Jang & Lee 2016; Beaton et al. 2016). Lee & Jang (2012, 2013) (Papers I and II) determined the TRGB distances to three SNe Ia host galaxies: M101, M66, and M96 hosting SN 2011fe, SN 1989B, and SN 1998bu, respectively. In Paper III, Jang & Lee (2015) derived the TRGB distances to two additional SN Ia host galaxies: NGC 4038/39 and NGC 5584 hosting SN 2007sr and SN 2007af, respectively. By combining the TRGB distances to five SN Ia host galaxies with optical light curves for five SNe Ia in these galaxies, we obtained a value of the Hubble constant, $H_0 = 69.8 \pm 2.6$(random) $\pm$ 3.9(systematic) km s^{-1} Mpc^{-1}. In Paper VI, Jang & Lee (2016) presented a revised calibration of the TRGB with a systematic uncertainty of 0.046 mag, much smaller than those of the previous calibrations ($\sim$ 0.12 mag). This calibration used, as a distance anchor, NGC 4248 and the LMC to which geometric distances are known with high precision (Humphreys et al. 2013; Riess et al. 2016; Pietrzyński et al. 2013).

In this paper we present the TRGB distances to three additional galaxies hosting three SNe Ia: NGC 3021 (SA(rs)bc:) hosting SN 1995al, NGC 3370 (SA(s)c) hosting SN 1994ae, and NGC 1309 (SA(s)bc:) hosting SN 2002fk. Spectroscopic observations confirmed that three SNe are normal SNe Ia (Riess et al. 2009a). Light curves of these SNe Ia were obtained with modern CCD detectors, covering their maximum luminosity epochs. Moreover, the internal extinctions for these SNe are estimated to be small ($A_V \lesssim 0.5$ mag) (Riess et al. 2009a). Thus, these three SNe Ia are excellent targets for the luminosity calibration of SN Ia. Riess et al. (2005, 2009b) carried out deep HST observations for these galaxies to derive Cepheid distances to these galaxies. By combining optical light curves of Cepheid variables with their F160W band luminosities, they determined distances: $(m-M)_0 = 32.498 \pm 0.091$ for NGC 3021, $(m-M)_0 = 32.071 \pm 0.050$ for NGC 3370, and $(m-M)_0 = 32.524 \pm 0.056$ for NGC 1309 (Riess et al. 2016). However, there are no published studies for the TRGB distances to these galaxies.

The outline of this paper is as follows. In Section 2 we describe data and data reduction method. Section 3 presents the Color-Magnitude Diagrams (CMDs) and luminosity functions (LFs) of the resolved stars in three galaxies. These will be used to estimate the TRGB distances. In §4 we present updated TRGB distances to five SN Ia host galaxies included in our previous studies and compare our results with those from the SH0ES project (Riess et al. 2011; Riess et al. 2016). We also derive the absolute magnitude of SNe and the value of the Hubble constant. Primary results are summarized in the final section.

6.2 Data and Data Reduction

Table 6.1 lists basic information of archival HST images of the three SN Ia host galaxies we used for the TRGB analysis. These galaxies were observed using the same instrument, the Advanced Camera for Surveys (ACS), with a primary aim to detect Cepheid variables (PID=9651, 10497). These ACS fields cover halos as well as bulges and disks of the target galaxies, as shown in Figure 6.1. We constructed master drizzled images of each field from individual images as described in Jang & Lee (2015). We set final_pixfrac=0.7 and final_scale=0$''$.03/pixel in the drizzling, to secure better angular resolution than those of drizzled images from the default setting (final_pixfrac=1.0 and final_scale=0$''$.05/pixel). Total exposure times of each field are $\sim$ 61,500s for F555W band and 24,000s for F814W band. Figure 6.2 shows $10'' \times 10''$ sections of combined F814W band images we made for an outer region in each galaxy. Resolved stars are clearly seen in each field, and most of the faint resolved stars are old red giant stars.

Instrumental magnitudes were derived from the standard sequence, FIND–PHOT–ALLSTAR–ALLFRAME in the DAOPHOT package (Stetson 1987). PSF images were constructed using 30 $\sim$ 60 bright isolated stars in the images. Standard calibration of instrumental magnitudes on the HST Vega magnitude system was done using the information provided by the STScI. Detailed reduction methods can be

Table 6.1. A Summary of *HST* Observations of SNe Ia Calibration Sample

Target	R.A. (J2000.0)	Decl. (J2000.0)	Instrument	Exposure time F555W	Exposure time F814W	Prop. ID
NGC 3021	09 51 00.71	33 33 23.9	ACS/WFC	61,760s	24,000s	10497
NGC 3370	10 47 06.91	17 16 40.0	ACS/WFC	61,240s	24,000s	9651
NGC 1309	03 22 05.31	–15 23 47.8	ACS/WFC	61,760s	24,000s	10497

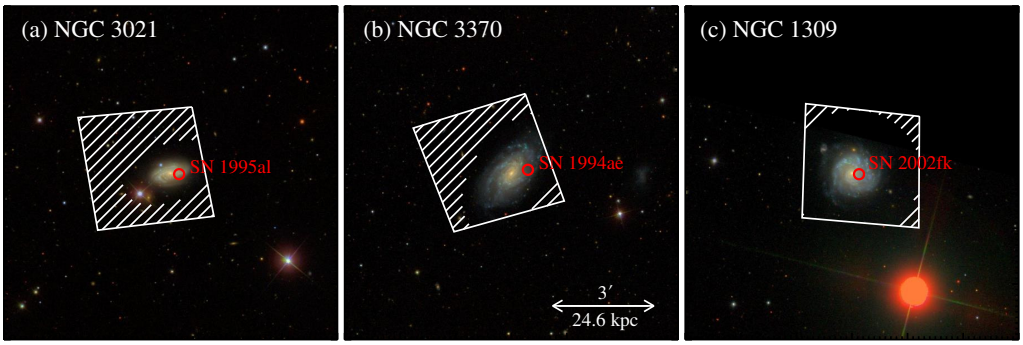

Figure 6.1: Identification of HST/ACS fields of NGC 3022, NGC 3370, and NGC 1309 used in this study overlayed on the $10' \times 10'$ color maps provided by the Sloan Digital Sky Survey. Locations of the SNe Ia are marked by open circles.

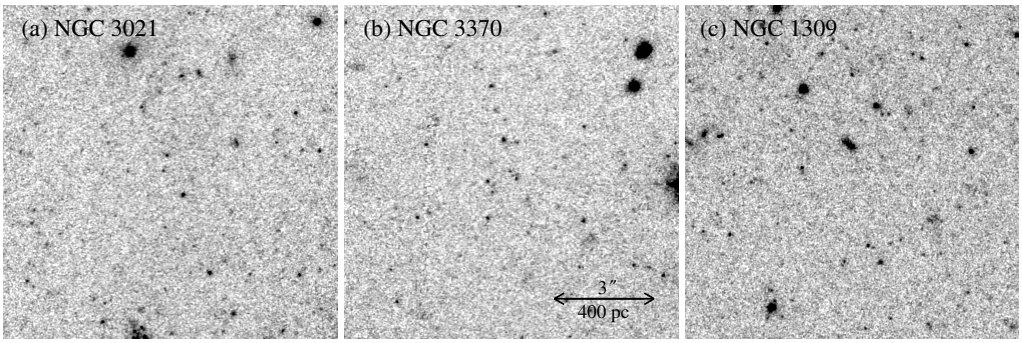

Figure 6.2: $10'' \times 10''$ thumbnails of $F814W$ band drizzled images showing the halo regions of NGC 3021 (a), NGC 3370 (b), and NGC 1309 (c). Most of the resolved point sources are old red giants in each galaxy.

found in our previous papers (Jang & Lee 2015, 2016).

6.3 Results

6.3.1 CMDs of Resolved Stars

The HST fields for the target galaxies cover not only the disk but also the halo of each galaxy. In order to sample old RGB stars as many as possible, we selected resolved stars in the outer regions of the target galaxies, as shown by the hatched regions in Figure 6.1.

We plotted the CMDs of the resolved stars in the selected regions of the target galaxies in Figure 6.3. Figure 6.3(a-c) show F814W – (F555W – F814W) CMDs of the resolved stars in the halos of NGC 3021 (a), NGC 3370 (b), and NGC 1309 (c). All three CMDs show a prominent RGB population.

It is expected that some of the point sources detected in the images of the target galaxies are unresolved background galaxies. In order to estimate the background galaxy contamination in the CMDs, we investigated the CMD of the Hubble eXtreme Deep Field (HXDF), which is dominated by background galaxies, as shown in Lee &

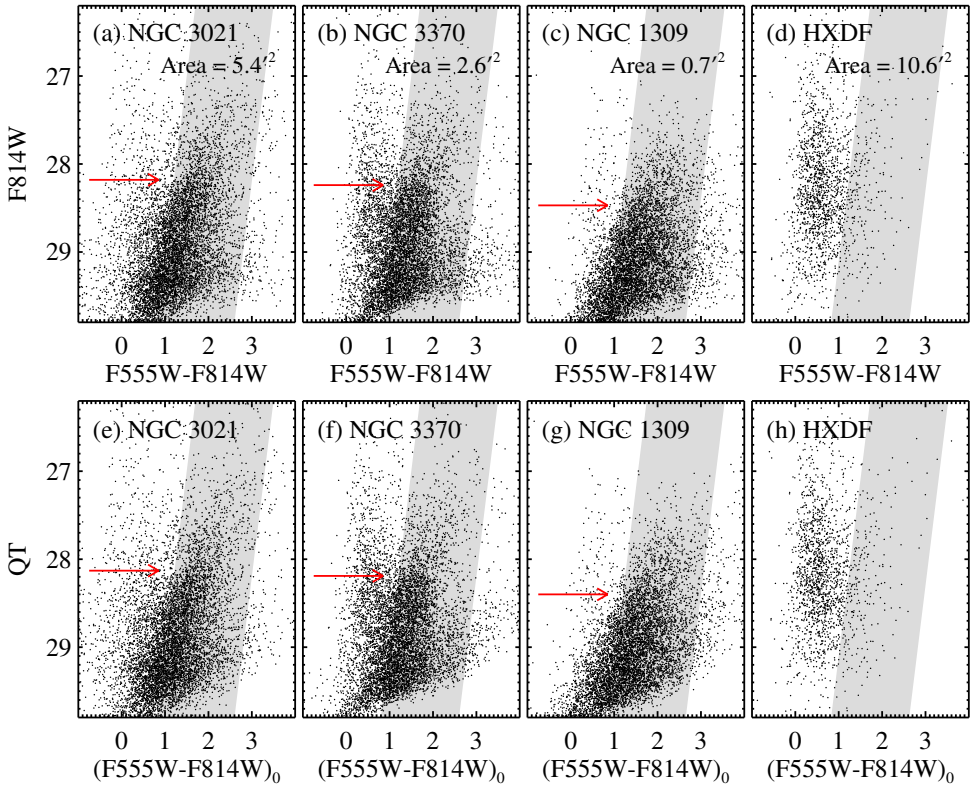

Figure 6.3: ((a),(b), and (c)) $F814W - (F555W - F814W)$ CMDs of the resolved stars in the halo regions of NGC 3021 (a), NGC 3370 (b), and NGC 1309 (c). We also display a CMD of the point sources in the Hubble eXtreme Deep Field (HXDF) in (d) as a reference. ((e), (f), (g) and (h)) Same as (a), (b), (c) and (d), except for the QT magnitude with the extinction corrected color, $(F555W - F814W)_0$. The shaded region in each panel denotes the RGB stars used for the TRGB analysis. Estimated TRGB magnitudes are marked by red arrows.

Jang (2016). We used combined F606W and F814W images for the HXDF provided by the XDF project (Illingworth et al. 2013). Then we carried out PSF photometry using the same procedure as done for the target galaxies. We applied the color transformation from F606W – F814W to F555W – F814W using the transformation described in Jang & Lee (2016), to be consistent with the CMDs of the target galaxies.

Figure 6.3(d) represents the CMD of the point sources in the HXDF. This CMD shows a significant vertical structure in the blue side of the shaded region (the RGB), while only a small number of sources are seen in the shaded region. This vertical structure represents mainly blue faint background galaxies. The area of this field is 10.6 arcmin^2, much larger than those of the selected regions for the target galaxies (5.4 arcmin^2, 2.6 arcmin^2 and 0.7 arcmin^2 for NGC 3021, NGC 3370, and NGC 1309, respectively). We counted the numbers of bright point sources with F814W $\leq$ 29 located in the shaded regions, which were chosen to select the RGB population, obtaining 2370, 2269, 2468, and 227 sources for NGC 3021, NGC 3370, NGC 1309, and the HXDF, respectively. Considering the field area ratios, we estimated the fractions of the background galaxies for the target galaxies: 4.7% for NGC 3021, 2.5% for NGC 3370, and 0.6% for NGC 1309. Thus, background galaxy contamination in the shaded regions of the target galaxies is negligible. We ignored the background galaxy contamination in the following TRGB analysis.

Jang & Lee (2016) introduced the QT magnitude, a color (metallicity) corrected RGB magnitude, for the more accurate TRGB calibration. The QT magnitude is defined as $QT = \mathrm{F814W}_0 - 0.093(Color - 1.6)^2 - 0.024(Color - 1.6)$, where $Color =$ (F555W – F814W)$_0$ for the ACS/WFC. We plotted QT magnitude versus (F555W–F814W)$_0$ diagrams of the resolved point sources in Figure 6.3(e-h). Foreground reddenings are known to be very small: $E(B-V) = 0.012$, 0.028, 0.035, and 0.007 for NGC 3021, NGC 3370, NGC 1309 and the HXDF, respectively (Schlafly & Finkbeiner 2011, NASA/IPAC Extragalactic Database). Internal reddenings of the selected outer regions are expected to be negligible so that these are assumed to be

zero in this study.

6.3.2 Distance Estimation

We determined the distances to the target galaxies using the TRGB method (Lee et al. 1993; Madore & Freedman 1995). Figure 6.4 displays F814W (a, b, and c) and QT (d, e, and f) LFs of the RGB stars in the outer regions of the target galaxies, which were selected using the shaded regions in the CMDs. The LFs for all three galaxies show an abrupt increment at $F814W \simeq QT = 28.2 \sim 28.5$ mag, which corresponds to the TRGB. We applied an edge detection algorithm for the quantitative TRGB detection. We used a weighted logarithmic edge detector (Méndez et al. 2002) described as $E(I) = \sqrt{\phi}[log[\phi(I+\sigma_I)] - log[\phi(I-\sigma_I)]]$, where $\phi(I)$ is a Gaussian-smoothed LFand σ_I is the mean photometric uncertainty. Output edge detection responses are shown as curved lines in Figure 6.4. Mean TRGB magnitudes and corresponding uncertainties were measured using the bootstrap method as done for our previous studies (Lee & Jang 2012, 2013; Jang & Lee 2015). Measured TRGB values are: F814W= $28.190 \pm 0.056, 28.252 \pm 0.060$ and 28.495 ± 0.056 mag for NGC 3021, NGC 3370, and NGC 1309, respectively. Similarly, $QT = 28.152 \pm 0.046$ mag for NGC 3021, 28.208 ± 0.061 mag for NGC 3370, and 28.398 ± 0.048 mag for NGC 1309 were obtained.

Distance moduli to target galaxies were derived by applying the TRGB calibration for F814W band magnitude given by Rizzi et al. (2007): $M_{F814W,TRGB} = -4.06+0.15[(F555W-F814W)_0-1.74]$. We estimated the median TRGB colors corrected for the foreground reddenings: $(F555W-F814W)_0 = 1.74\pm0.02, 1.73\pm0.02$, and 1.84 ± 0.03 mag for NGC 3021, NGC 3370, and NGC 1309, respectively. Combining the F814W-band apparent and absolute magnitudes, we obtain distance moduli: $(m-M)_0 = 32.232 \pm 0.056$ for NGC 3021, 32.272 ± 0.060 for NGC 3370, and 32.488 ± 0.056 for NGC 1309. Systematic uncertainties are estimated to be 0.12 mag (Bellazzini et al. 2001).

We also derive more accurate distance moduli using the revised TRGB calibra-

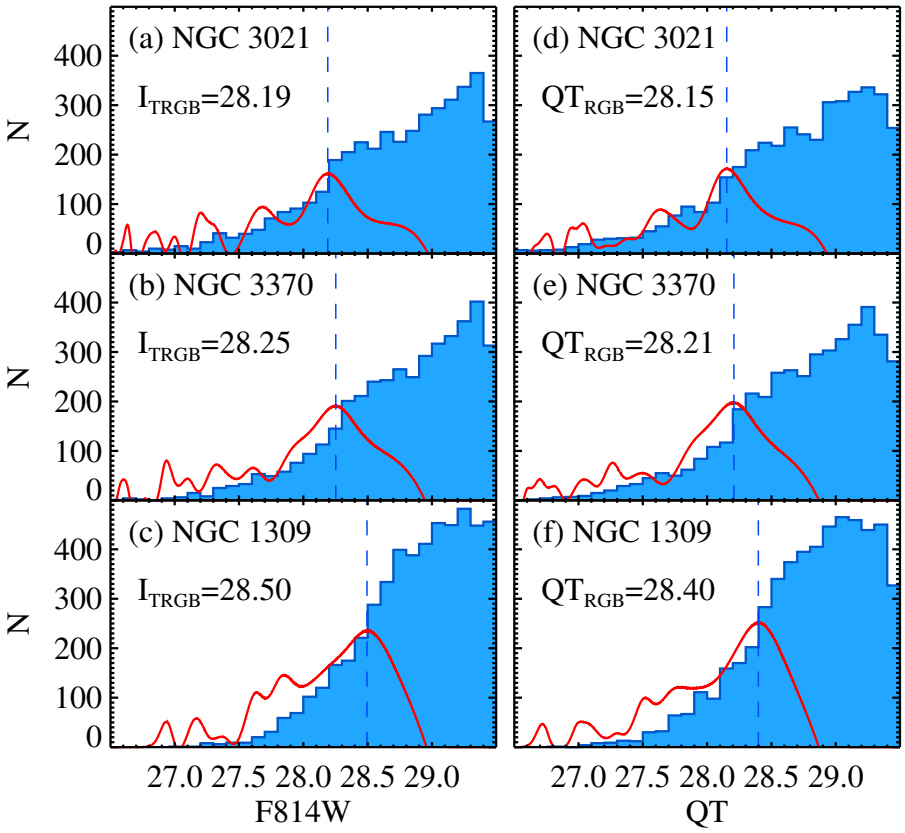

Figure 6.4: ((a), (b), and (c)) LFs (histograms) and edge detection responses (curved lines) of the RGB stars in NGC 3021 (a), NGC 3370 (b), and NGC 1309 (c). Estimated TRGB magnitudes are marked in each panel. ((d), (e), and (f)) Same as (a), (b), and (c), except for the QT magnitude.

tion introduced by Jang & Lee (2016). Jang & Lee (2016) presented a revised TRGB calibration, using NGC 4258 and the LMC as a distance anchor (Humphreys et al. 2013; Riess et al. 2016; Pietrzyński et al. 2013). Under the photometic system used in this study, F555W and F814W band combination of ACS/WFC, the absolute magnitude of the TRGB is $M_{QT,TRGB} = -4.115 \pm 0.060$ mag for the NGC 4258 scale, and $M_{QT,TRGB} = -4.027 \pm 0.070$ mag for the LMC scale. A weighted mean of these two is $M_{QT,TRGB} = -4.078 \pm 0.046$ mag. If we adopt this value, we obtain $(m - M)_0 = 32.229 \pm 0.046$ for NGC 3021, $(m - M)_0 = 32.285 \pm 0.052$ for NGC 3370, and $(m - M)_0 = 32.475 \pm 0.048$ for NGC 1309. Systematic uncertainties are estimated to be 0.046 mag. Table 6.2 lists a summary of distance estimates based on the revised TRGB calibration for the target galaxies in this study. We also included five other galaxies that were covered in our previous studies (Lee & Jang 2012, 2013; Jang & Lee 2015).

6.4 Discussion

6.4.1 Updating the TRGB Distances in Our Previous Studies

In Paper I (Lee & Jang 2012), II (Lee & Jang 2013), and III (Jang & Lee 2015), we presented the TRGB distances to five SN Ia host galaxies: M101 (Paper I), M66 and M96 (Paper II), and NGC 4038/39 and NGC 5584 (Paper III). These results were based on the old TRGB calibration (Rizzi et al. 2007). We update these results using the revised TRGB calibration introduced in Paper IV (Jang & Lee 2016). We carried out PSF photometry on drizzled images (indicated by _drc.fits) of the five galaxies using DAOPHOT/ALLFRAME (Stetson 1987, 1994). We used the same HST data set as analyzed in our previous studies, except for M101. In the case of M101 we used new HST/ACS data of a halo field (centered at (α, δ)=($14^h03^m47.21^s, 54°14'25\farcs6$)) released recently (PID=13364). Exposure times are 1100 s for F606W and 1400 s for F814W, longer than those used in Paper I (F555W = 720s $\sim$ 1080s and F814W = 720s $\sim$ 1080s).

Table 6.2. A Summary of the TRGB Distance Estimates

Target	Region	QT	$(m-M)_0^c$ NGC 4258 scale	$(m-M)_0^d$ LMC scale	$(m-M)_0^e$ NGC 4258 + LMC
M101	Entire field	25.086 ± 0.034	29.205 ± 0.034	29.117 ± 0.034	29.168 ± 0.034
M66	$R_{GC} \geq 4'.3^a$	26.097 ± 0.030	30.212 ± 0.030	30.124 ± 0.030	30.175 ± 0.030
M96	$R_{GC} \geq 3'.5^a$	26.103 ± 0.065	30.218 ± 0.065	30.130 ± 0.065	30.181 ± 0.065
NGC 4038/39	Lowest sky[b]	27.627 ± 0.035	31.746 ± 0.035	31.658 ± 0.035	31.709 ± 0.035
NGC 5584	Lowest sky[b]	27.681 ± 0.042	31.804 ± 0.042	31.717 ± 0.042	31.768 ± 0.042
NGC 3021	$SMA \geq 1'.5$	28.152 ± 0.046	32.267 ± 0.046	32.179 ± 0.046	32.229 ± 0.046
NGC 3370	$SMA \geq 2'.0$	28.208 ± 0.052	32.323 ± 0.052	32.235 ± 0.052	32.285 ± 0.052
NGC 1309	$SMA \geq 2'.0$	28.398 ± 0.048	32.513 ± 0.048	32.425 ± 0.048	32.475 ± 0.048

[a]Hatched regions shown in Figure 3.1 of Chapter 3

[b]Hatched regions shown in Figure 4.1 of Chapter 4

[c]Systematic uncertainties are estimated to be 0.060 mag

[d]Systematic uncertainties are estimated to be 0.070 mag

[e]Systematic uncertainties are estimated to be 0.046 mag

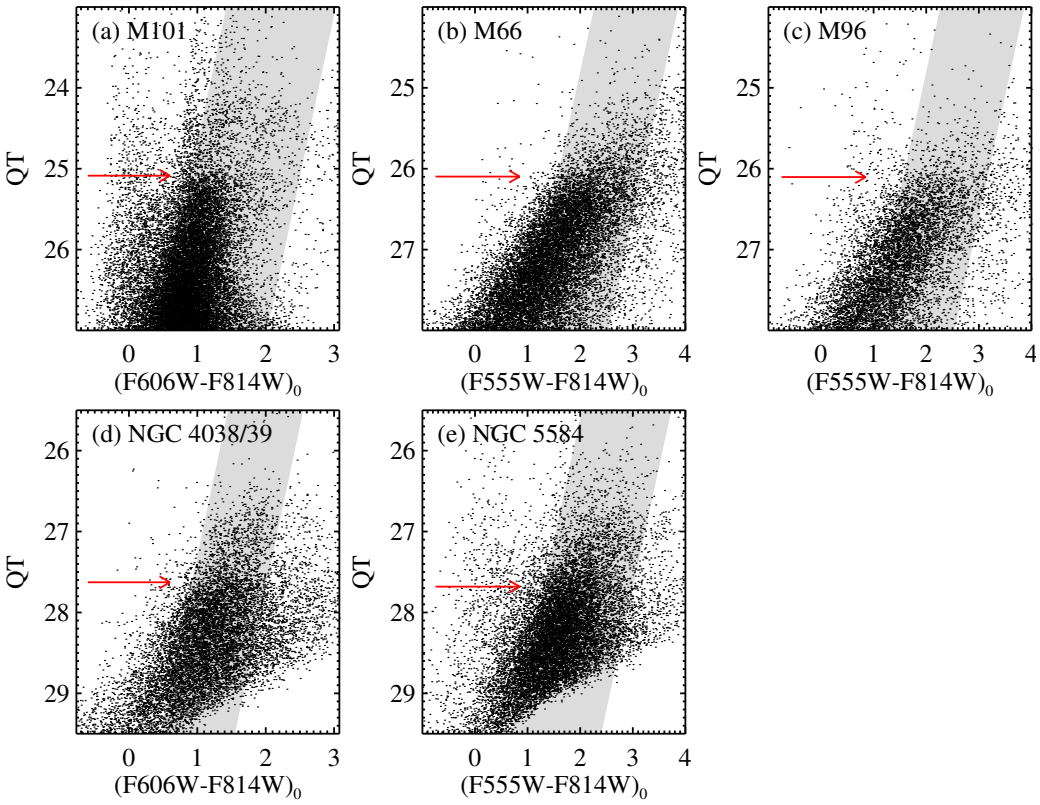

Figure 6.5: CMDs of resolved stars in five SN Ia host galaxies. We used foreground extinction corrected colors and the QT magnitudes in the plots. The shaded region in each panel represents the selection criteria for RGB stars. Estimated TRGB magnitudes are marked by red arrows.

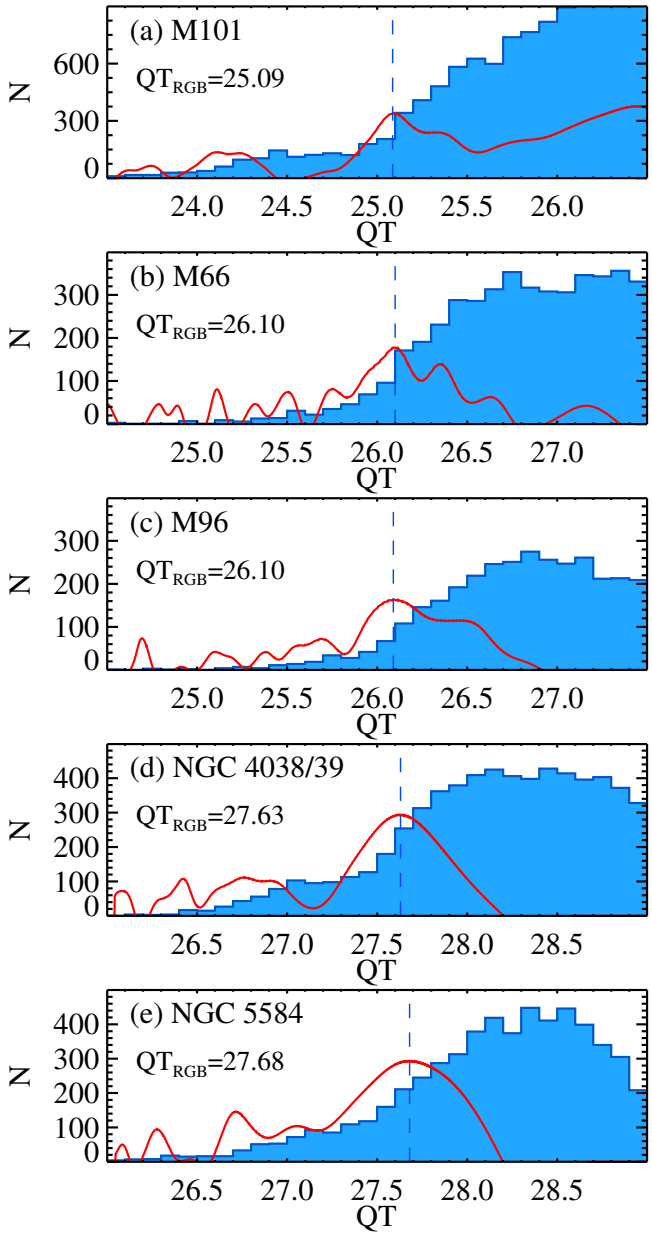

Figure 6.6: *QT* magnitude luminosity functions of RGB stars in the outer regions of five SN Ia host galaxies. Edge detection responses and estimated TRGB magnitudes are indicated by solid and dashed lines, respectively.

Figure 6.5 displays the CMDs with QT magnitudes of the resolved stars in the outer regions of M101, M66, M96, NGC 4038/39 and NGC 5584. All the CMDs show dominant RGB populations, as well as asymptotic giant branch and young main sequence populations. Most of the stars are located in the shaded regions that cover the RGBs. We selected the stars in the shaded regions of Figure 6.3, producing a sample of RGB stars in each galaxy. Then we plotted their LFs and corresponding edge detection responses in Figure 6.4. The LFs of these galaxies show sudden jumps at $QT \sim 25.1$ (M101), 26.1 (M66 and M96), and 27.7 (NGC 4038/39 and NGC 5584), corresponding to the TRGBs. Mean TRGB magnitudes and corresponding errors were measured using the bootstrap method as done for the three galaxies described in Section 6.3.2. Derived values of the TRGB magnitudes are: $QT_{\rm RGB} = 25.086 \pm 0.034$ for M101, 26.097 ± 0.030 for M66, 26.103 ± 0.065 for M96, 27.627 ± 0.035 for NGC 4038/39, and 27.681 ± 0.042 for NGC 5584. Here all errors are random errors. The TRGB distances to these galaxies were obtained by applying the TRGB calibration given in Jang & Lee (2016). A summary of the TRGB distances of these five galaxies is included in Table 6.2.

The values of the TRGB distances to these galaxies based on the new calibrations show excellent agreement ($\Delta(m-M)_0 \lesssim 0.05$) with those in our previous papers, except for M101. In the case of M101, the new estimate of the distance modulus, $(m-M)_0 = 29.168 \pm 0.034$, is 0.132 shorter than the value in Lee & Jang (2012), $(m-M)_0 = 29.30 \pm 0.01$. Main causes for this difference can be explained as follows. First is the difference in the values of the aperture correction for photometry. We adopted a value of 0.098 mag provided by the STScI in this study, whereas Lee & Jang (2012) used an aperture correction of 0.04 mag, which was derived from the data of M101. The latter value of aperture correction based on a small number of bright stars in M101 was an underestimation. Second is the difference in the images of M101 used for analysis. We used the images corrected for charge transfer efficiency in this study, while Lee & Jang (2012) used the images without this correction that were the only available images at that time.

6.4.2 Comparison with the SH0ES Project

The SH0ES project has been working on the calibration of SN Ia to measure an accurate value of the Hubble constant as well as other cosmological parameters (Riess et al. 2005, 2009a,b; Riess et al. 2011; Riess et al. 2016). They used Cepheid variables, a Population I indicator, for deriving distances to SN Ia host galaxies. Riess et al. (2011); Riess et al. (2016) considered four nearby distance anchors for the calibration of Cepheids: NGC 4258, the LMC, the Milky Way, and M31. They provided Cepheid distance estimates to SN Ia host galaxies based on three anchors (NGC 4258, the LMC, and the Milky Way) in Table 3 of Riess et al. (2011) and in Table 5 of Riess et al. (2016). Among eighteen and eight SN Ia host galaxies used in Riess et al. (2016) and Riess et al. (2011), six (M101, NGC 4038/39, NGC 5584, NGC 3021, NGC 3370, and NGC 1309) and five galaxies (the above excluding M101), respectively, are common with those in this study. Thus, we compare distance estimates of these galaxies derived in this study with those in Riess et al. (2011); Riess et al. (2016), summarizing the results in Table 6.3.

Figure 6.7(a) displays a comparison of the TRGB distance estimates to SN Ia host galaxies derived in this study with Cepheid distance estimates to 6 galaxies in Riess et al. (2016) (circles) and 5 galaxies in Riess et al. (2011) (pentagons). Differences of distance estimates, $\Delta(m-M)_0 = (m-M)_{0,\mathrm{TRGB}} - (m-M)_{0,\mathrm{Cepheids}}$, are shown in Figure 6.7(b). Riess et al. (2011) adopted a megamaser distance to NGC 4258 of $(m-M)_0 = 29.31 \pm 0.05$, which is slightly smaller than the value used in Riess et al. (2016) and this study, $(m-M)_0 = 29.387 \pm 0.057$. Riess et al. (2016) improved slightly the estimate of NGC 4258 distance given by Humphreys et al. (2013), and presented an updated value. However, the distance values in Table 3 of Riess et al. (2011) and Table 5 of Riess et al. (2016) are based on the combination of three anchors (NGC 4258, the LMC, and the MW) so the effect of the change for NGC 4258 alone is not as large as 0.077 mag. Riess et al. (2016) presented a comparison of their results with those in Riess et al. (2011) for the seven common galaxies (except for NGC 4038/39): the mean difference ($\Delta(m-M)_0$ = Riess et al.

Table 6.3. A Comparison of Distance Estimates to SN Ia Host Galaxies

Target	This study[a] (TRGB)	R11[b] (Cepheids)	R16[b] (Cepheids)	This study – R11	This study – R16
M101	29.168 ± 0.034	...	29.135 ± 0.045	...	0.033 ± 0.074
NGC 4038/39	31.709 ± 0.035	31.66 ± 0.08	31.290 ± 0.112	0.049 ± 0.100	0.419 ± 0.132
NGC 5584	31.768 ± 0.042	31.72 ± 0.07	31.786 ± 0.046	0.048 ± 0.095	-0.018 ± 0.079
NGC 3021	32.229 ± 0.046	32.27 ± 0.08	32.498 ± 0.090	-0.041 ± 0.104	-0.269 ± 0.113
NGC 3370	32.285 ± 0.052	32.13 ± 0.07	32.072 ± 0.049	0.155 ± 0.100	0.213 ± 0.087
NGC 1309	32.475 ± 0.048	32.59 ± 0.09	32.523 ± 0.055	-0.115 ± 0.112	-0.048 ± 0.088
Weighted mean of all				0.027 ± 0.045[c]	0.038 ± 0.037[d]
Weighted mean of all excluding NGC 4038/39				0.021 ± 0.051[e]	0.006 ± 0.038[f]

[a]Based on two distance anchors: NGC 4258 and the LMC.

[b]Based on three distance anchors: NGC 4258, the LMC, and the Milky Way. R11 and R16 denote Riess et al. (2011) and Riess et al. (2016), respectively.

[c]Standard deviation of 0.103 mag.

[d]Standard deviation of 0.237 mag.

[e]Standard deviation of 0.116 mag.

[f]Standard deviation of 0.142 mag.

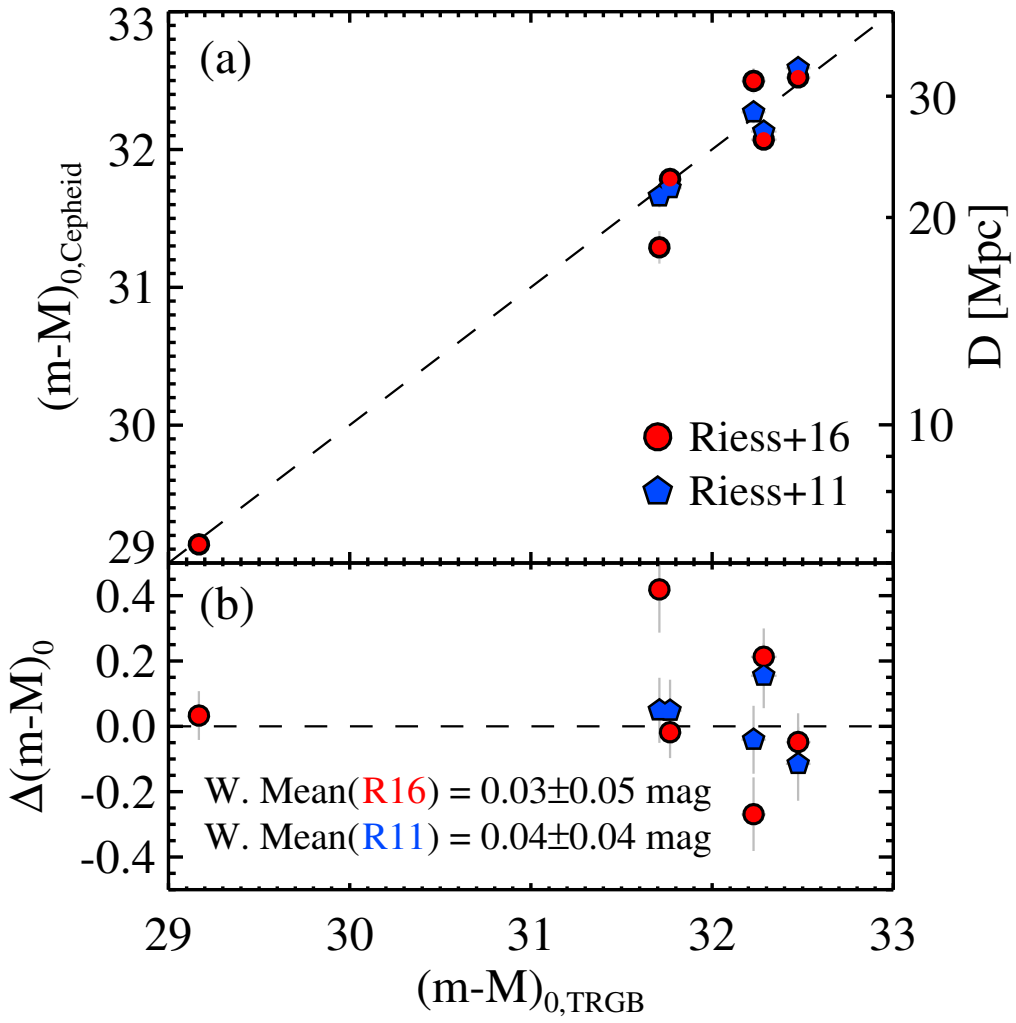

Figure 6.7: (a) Comparison of distance estimates to SN Ia host galaxies derived in this study based on the TRGB with previous studies based on Cepheids: Riess et al. (2016) (circles) and Riess et al. (2011) (pentagons). (b) Differences ($\Delta(m-M)_0 = (m-M)_{0,TRGB} - (m-M)_{0,Cepheids}$) between this study and the previous studies. A weighed mean of each study is labeled.

(2016) minus Riess et al. (2011)) is 0.01 mag with a dispersion of 0.12 mag. They noted, however, that the distance difference for NGC 4038/39 (antennae galaxies) hosting SN 2007sr is as large as $\Delta(m-M)_0 = -0.37$. This large difference is due to removing ten Cepheids with ultra-long period (ULP, $P > 100$ days) in the sample of Cepheids for NGC 4038/39 during the new analysis of Riess et al. (2016).

The TRGB distance estimates in this study and the Cepheid distance estimates in Riess et al. (2011) and Riess et al. (2016) show in general good agreement. One outlier seen at $\Delta(m-M)_0 = 0.419 \pm 0.132$ of Figure 6.7(b) is NGC 4038/39. A weighted mean of distance difference for the five galaxies between this study and Riess et al. (2011) is very small: $\Delta(m-M)_0 = 0.027 \pm 0.045$ mag. A comparison with Riess et al. (2016) for the six overlapping galaxies yields a similar offset, $\Delta(m-M)_0 = 0.038 \pm 0.037$ mag. If we exclude NGC 4038/39 in the comparison, the mean difference between this study and Riess et al. (2016) becomes nearly zero, $\Delta(m-M)_0 = 0.006 \pm 0.038$ mag.

In summary, our TRGB distance estimates are in good agreement with the Cepheid distance estimates in Riess et al. (2011); Riess et al. (2016). A better agreement is seen with those in Riess et al. (2016), if we exclude NGC 4038/39.

6.4.3 A Distance Discrepancy for NGC 4038/39

The significant difference ($\Delta(m-M)_0$(TRGB − Cepheid) $= 0.419 \pm 0.132$) for NGC 4038/39 between the TRGB distance in this study and the Cepheid distance in Riess et al. (2016) is an interesting issue, deserving to investigate any cause for this discrepancy. NGC 4038/39 is a pair of interacting galaxies, showing clear features of strong star formation. However, the CMD of the resolved stars derived from deep HST images of a region outside arms in NGC 4038/39 shows a prominent RGB as well as a weaker AGB. Photometry of the RGB stars reaches about 1.5 mag below the TRGB so that the detection of the TRGB is considered to be solid (Jang & Lee 2015). The TRGB distance for NGC 4038/39 in this study and Jang & Lee (2015) is consistent with the previous estimate based on the TRGB by Schweizer et al.

(2008), $(m-M)_0 = 31.51 \pm 0.17$. Thus the TRGB distance estimate for this galaxy in this study is considered to be reliable.

On the other hand, two recent studies based on the same data of Cepheids, Riess et al. (2011) and Riess et al. (2016), showed a large discrepancy. The reason for this difference is related with the presence of ULP Cepheids in the Cepheid sample for NGC 4038/39. ULP Cepheids have longer periods ($P > 80$ days) and brighter ($-6 > M_V > -8$) than classical Cepheids. They are often found in star-forming late type galaxies with low-metallicity and their period-luminosity relation is not as well-known as classical Cepheids (Bird et al. 2009; Fiorentino et al. 2012, 2013).

Riess et al. (2016) excluded 10 ULP Cepheids from the sample of Cepheids for NGC 4038/39 used in Riess et al. (2011) for distance estimation, because the phase coverage of these Cepheids is very sparse and because the period-luminosity relation of ULP Cepheids is not as reliable as that of normal Cepheids. From the Cepheid sample without ULP Cepheids, Riess et al. (2016) obtained a distance modulus for NGC 4038/39, 0.37 mag smaller than the value derived from the full sample of Cepheids that was used in Riess et al. (2011). Fiorentino et al. (2013) applied a theoretical scenario for classical Cepheids to the same sample of Cepheids (including ULP Cepheids) in the galaxies as used in Riess et al. (2011). They derived a distance to NGC 4038/39 from the full sample of Cepheids, $(m-M)_0 = 31.55 \pm 0.06$, which is consistent with the value in Riess et al. (2011), but about 0.3 larger than the value given by Riess et al. (2016). NGC 4038/39 shows the largest fraction of ULP Cepheids in the sample of SN Ia host galaxies used by Riess et al. (2011); Riess et al. (2016), which must be strongly related with active star formation activity. Considering that most of the Cepheids in Cepheid distance anchors are classical Cepheids, it appears to be conservative to use only classical Cepheids in the case of NGC 4038/39. However, it is difficult to understand the large difference between this value and the TRGB distance. A further study is needed to investigate the effect of the ULP Cepheids in Cepheid distance estimation (Fiorentino et al. 2012).

6.4.4 The Calibration of SNe Ia and the Hubble Constant

With the TRGB distances to SN Ia host galaxies derived in this study, we calibrate the absolute peak luminosity of SNe Ia and estimate the value of the Hubble constant. Optical light curves of eight SNe Ia were obtained from various literature: $UBVRI$ photometric data for SN 2011fe from Pereira et al. (2013), for SN 1989B from Wells et al. (1994), for SN 1998bu from Jha et al. (1999), for SN 1995al from Riess et al. (2009a), $BVRI$ photometric data for SN 1994ae and SN 2002fk from Riess et al. (2009a), and $uBVri$ photometric data for SN 2007sr and SN 2007af from the Carnegie Supernova Program (Hamuy et al. 2006) (u) and Hicken et al. (2009) (BVri). We also compiled three V-band observations at the pre-maximum of SN 2007sr provided by the All-Sky Automated Survey (ASAS) (Pojmanski 1997) and Riess et al. (2011). All eight SNe Ia were observed with CCD detectors, so that detector dependent uncertainties are estimated to be smaller than those from photographic or photoelectric detectors.

We derived light curve parameters of each SN Ia using the MLCS2K2 code (version 0.07) (Jha et al. 2007). We set total to selective extinction ratio, $R_V = 3.1$ for the Milky Way and R_V=2.5 for the SN Ia host galaxies, to be consistent with the values used in Riess et al. (2011); Riess et al. (2016). The derived values of the parameters, A_V and $m_V^0 + 5a_V$ (where $a_V = 0.697 \pm 0.002$ (Riess et al. 2011)), are listed in Table 6.4. We also listed the $m_V^0 + 5a_V$ values from Jha et al. (2007) and Riess et al. (2011) in column six of Table 6.4. The values of $m_V^0 + 5a_v$ derived in this study agree well with those from Jha et al. (2007) and Riess et al. (2011), showing a mean difference of 0.004 mag. Absolute maximum magnitudes of eight SNe Ia, corrected to the fiducial color and luminosity, were also derived from the m_V^0 values and the TRGB distances derived in this study, as listed in the column nine of Table 6.3. Quoted uncertainties are quadratic sums of the TRGB distance errors, extinction errors (10% of the Milky Way and the host galaxy extinction values), and the luminosity dispersion of SNe Ia, 0.14 mag (Jha et al. 2007).

Figure 6.8 displays distributions of V-band absolute maximum magnitudes (M_V^0)

Table 6.4. A Summary of Optical Luminosity Calibration of SNe Ia

Galaxy	SN Ia	Filters	A_V	$m_V^0 + 5a_V$ This study	$m_V^0 + 5a_V$ Literature	$m_B^0 + 5a_B$ From R16	$(m-M)_0$ TRGB	M_V^0 R11 calibration	M_B^0 R16 calibration
M101	SN 2011fe	UBVRI	0.157	13.400	...	13.310	29.168 ± 0.034	-19.263 ± 0.145	-19.422 ± 0.122
M66	SN 1989B	UBVRI	1.242	14.076	14.021[a]	...	30.175 ± 0.030	-19.584 ± 0.190	...
M96	SN 1998bu	UBVRI	1.025	14.278	14.263[a]	...	30.181 ± 0.065	-19.388 ± 0.185	...
N4038/39	SN 2007sr	uBVri	0.349	15.889	15.901[b]	15.795	31.709 ± 0.035	-19.305 ± 0.148	-19.478 ± 0.119
N5584	SN 2007af	uBVri	0.346	16.295	16.274[b]	16.264	31.768 ± 0.042	-18.958 ± 0.150	-19.068 ± 0.122
N3021	SN 1995al	BVRI	0.213	16.630	16.699[b]	16.526	32.229 ± 0.046	-19.084 ± 0.149	-19.267 ± 0.126
N3370	SN 1994ae	UBVRI	0.045	16.556	16.545[b]	16.474	32.285 ± 0.051	-19.214 ± 0.149	-19.375 ± 0.126
N1309	SN 2002fk	BVRI	0.072	16.774	16.768[b]	16.755	32.475 ± 0.048	-19.186 ± 0.148	-19.284 ± 0.126
Weighted mean of eight SNe								-19.224 ± 0.055	...
Weighted mean of six low-reddened SNe								-19.170 ± 0.061	-19.318 ± 0.050

[a]Note. A_V denotes V-band host galaxy extinction derived from the light curve fitting with the MLCS2k2 code. m_V^0 and m_B^0 indicate the corrected apparent peak magnitude of SN Ia in V and B-band, respectively. a_V ($= 0.697 \pm 0.002$) and a_B ($= 0.7127 \pm 0.0017$) denote the V and B-band intercepts of the SN Ia Hubble diagram.

[a]Derived from Jha et al. (2007)

[b]Derived from Riess et al. (2011)

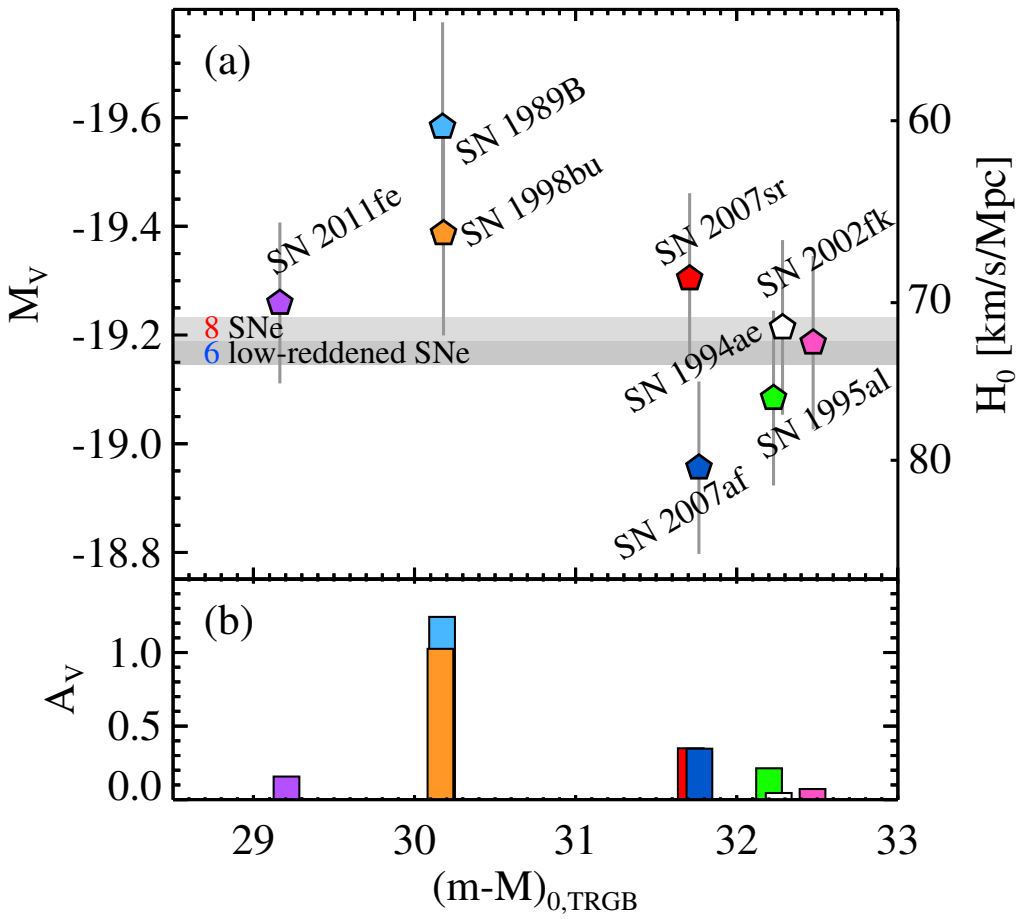

Figure 6.8: (a) Comparison of absolute peak magnitudes of eight SNe Ia with their TRGB distances derived in this study. Two shaded regions indicate weighted means of eight SNe Ia (upper region) and six low-reddened SNe Ia (lower region). (b) A comparison of V-band host galaxy extinction values (A_V) with the TRGB distances. Note that two SNe, SN 1989B in M66 and SN 1998bu in M96, show significantly higher extinctions than those of other six SNe.

and host galaxy extinction values (A_V) of SNe Ia as a function of the TRGB distances derived in this study. Absolute magnitudes of SNe Ia range from $M_V^0 = -18.958$ (SN 2007af) to -19.584 (SN 1989B). Host galaxy extinction values are estimated to be small, except for two SNe. SN 1989B and SN 1998bu show significantly higher extinction values ($A_V > 1.0$) than those of other SNe ($A_V < 0.4$). Thus derived absolute magnitudes for these two highly reddened SNe are probably less reliable than the others, although we corrected for their extinctions. The standard deviation of all eight SNe and six low-reddened SNe are 0.190 mag and 0.128 mag, respectively. The former is slightly larger than the intrinsic luminosity dispersion of SNe Ia derived from a large sample of SNe, 0.14 mag (Jha et al. 2007) and 0.128 mag (Riess et al. 2016). On the other hand, the value for the six low-reddened SNe is similar to the intrinsic luminosity dispersion of SNe.

A weighted mean of the absolute peak magnitude of eight SNe is $M_V^0 = -19.224\pm$ 0.055 mag. It is 0.104 mag brighter than that from the SH0ES project (Riess et al. 2011; Riess et al. 2016) ($M_V^0 = -19.12$ mag). If we use six low-reddened SNe, then a weighted mean of the absolute peak magnitude would be slightly fainter, $M_V^0 = -19.170 \pm 0.061$, getting closer to the estimate by Riess et al. (2011); Riess et al. (2016). Riess et al. (2016) provided SALT-II fits of nineteen SNe Ia including the six low-reddened SNe used in this study. They did not included two highly reddened SNe, SN 1989B and SN 1998bu. The values of $m_B^0 + 5a_B$ provided by Riess et al. (2016) are listed in column seven of Table 6.4. The B-band absolute magnitudes of SNe Ia (M_B^0) were derived from the m_B^0 values in Riess et al. (2016) and the TRGB distance estimates in this study, as listed in the last column of Table 6.4. A weighted mean of the B-band absolute magnitudes of the six SNe is $M_B^0 = -19.318 \pm 0.050$ mag. It is 0.066 mag brighter than that given in Riess et al. (2016), $M_B^0 = -19.25$ mag.

Riess et al. (2011); Riess et al. (2016) presented an equation deriving the value of H_0 from the absolute magnitude of SNe Ia:

$$logH_0 = \frac{M_x^0 + 5a_x + 25}{5}$$

where M_x^0 is an absolute magnitude of SNe Ia and a_x is an intercept of the SN Ia Hubble diagram in band-x.

Riess et al. (2011) presented a value of a_V ($= 0.697 \pm 0.00201$) that was determined from the MLCS2k2 fits of 140 SNe Ia at $0.023 < z < 0.10$. Combining the above equation with the V-band absolute magnitudes of SN Ia derived in this study, we derive a value of the Hubble constant: $H_0 = 71.15 \pm 1.80$(random) $\pm$ 1.51(systematic) km s^{-1} Mpc^{-1}from the eight SNe, and $H_0 = 72.95 \pm 2.03$(random) $\pm$ 1.55(systematic) km s^{-1} Mpc^{-1}from the six low-reddened SNe.

Riess et al. (2016) provided an updated value, $a_B = 0.7127 \pm 0.0017$ from the SALT-II fits of 233 SNe at $0.023 < z < 0.15$. If we use this value and the sample of six low-reddened SNe, we obtain our best estimate of the Hubble constant, which is accurate to 3.23% ($\pm$2.29 km s^{-1} Mpc^{-1}) including the systematics: $H_0 = 70.45 \pm 1.67$(random) $\pm$ 1.56(systematic) km s^{-1} Mpc^{-1}. Riess et al. (2016) presents also a value of the Hubble constant, when only two distance anchors (NGC 4258 and the LMC) are used for Cepheid distances: $H_0 = 71.61 \pm 1.78$ km s^{-1} Mpc^{-1}. Thus, our best estimate is consistent with this value. This shows that the TRGB and the Cepheid produce distance results consistent with each other, as long as the same distance anchors are used.

In Figure 6.9, we compare recent values of the Hubble Constant based on the TRGB calibration of SN Ia in this study including Lee & Jang (2012, 2013); Jang & Lee (2015), the Cepheid calibration of SN Ia (Freedman et al. 2001; Sandage et al. 2006; Riess et al. 2009b; Riess et al. 2011; Freedman et al. 2012; Riess et al. 2016), and the WMAP and PLANCK CMBR results. Our best estimate is between the values from the Cepheid calibrated SNe Ia based on all four distance anchors and those from the CMB analysis. The levels of differences between our best estimate and the values from other studies are: 1.24σ with Planck Collaboration et al. (2015) (PLANCK), 0.59σ with Bennett et al. (2013) (WMAP9), 1.03σ with Riess et al. (2016) (SH0ES), 1.38σ with Riess et al. (2011) (SH0ES), and 1.59σ

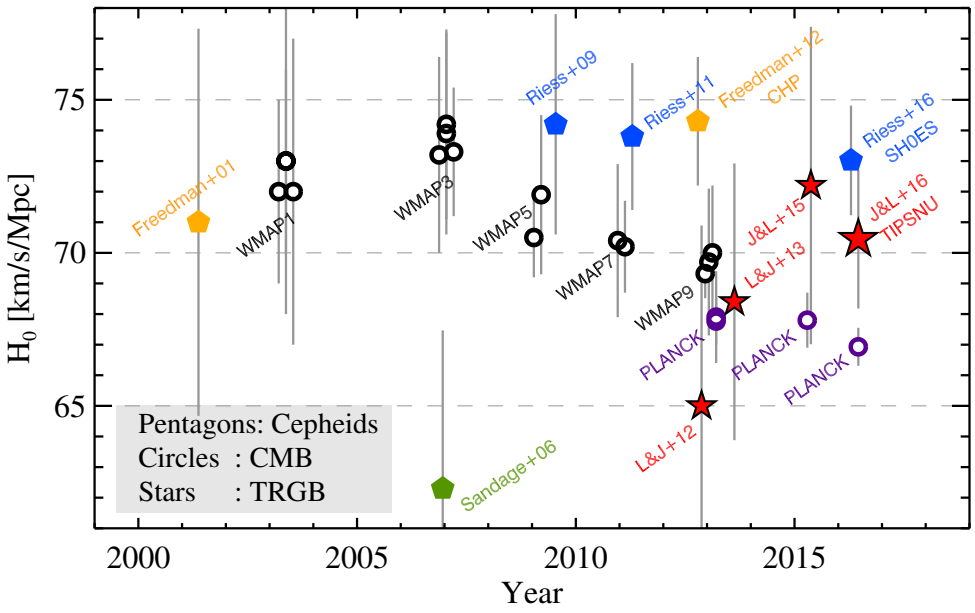

Figure 6.9: Comparison of recent values of the Hubble Constant based on the TRGB calibration of SN Ia (starlets), the Cepheid calibration of SN Ia (pentagons), and the WMAP and PLANCK CMBR results (circles). Note that our best TRGB estimate in this study is between the 2016 Cepheid value and the 2015 Planck value.

with Freedman et al. (2012) (CHP-I). Thus, our estimate agrees, within 1.6σ, with the recent estimations based on Cepheid calibrated SNe Ia and the CMB analysis. The Cepheid calibrated results in Riess et al. (2016) heighten the Hubble tension. On the other hand our TRGB calibrated results are comfortably located between the Cepheid results and the CMB results, lowering the Hubble tension.

In this study we used two distance anchors, NGC 4258 and the LMC, while recent Cepheid studies (Riess et al. 2011; Riess et al. 2016) utilized two more anchors, the Milky Way Cepheids with parallaxes and M31 for which geometric distances of two DEBs are known (Ribas et al. 2005; Vilardell et al. 2010) ($(m-M)_0 = 24.36 \pm 0.08$). Note that the two anchors used in this study favor a slightly lower value of the Hubble Constant, than the other two anchors, the Milky Way and M31: $H_0 = 72.2 \pm 2.51$ for NGC 4258, $H_0 = 72.04 \pm 2.67$ for the LMC, $H_0 = 76.18 \pm 2.37$ for the Milky Way, and $H_0 = 74.50 \pm 3.27$ for M31 km s^{-1} Mpc^{-1}(Riess et al. 2016). Thus it is important to understand any causes for this difference and to reduce this difference in the future. We are planning to investigate M31 as another anchor for the TRGB in the near future. When GAIA astrometry of the Milky Way stars is available, a number of TRGB stars in the Milky Way can be used for absolute calibration of the TRGB magnitudes so they can serve as a distance anchor for the TRGB (de Bruijne et al. 2014; Beaton et al. 2016).

6.5 Summary

Using deep photometry of the resolved stars in the HST images, we determine TRGB distances to three SN Ia host galaxies: NGC 3021 hosting SN 1995al, NGC 3370 hosting SN 1994ae, and NGC 1309 hosting SN 2002fk. We combine these results with those in our previous studies and calibrate the luminosity of SN Ia. Then we estimate the value of the Hubble Constant using the SN Ia with the TRGB calibration. Primary results are as follows.

- We find a significant number of old RGB stars in the halo regions of the three

galaxies, presenting their CMDs.

- Applying the revised TRGB calibration introduced by Jang & Lee (2016) (Paper IV) we measured the TRGB magnitudes, obtaining $QT_{\rm RGB}$=28.152 ± 0.046 for NGC 3021, 28.208 ± 0.052 for NGC 3370 and 28.398 ± 0.048 for NGC 1309. From these we derive TRGB distances: $(m-M)_0 = 32.229 \pm 0.046$ for NGC 3021, 32.285 ± 0.052 for NGC 3370, and 32.475 ± 0.048 for NGC 1309.

- We updated our previous distance estimates to five SN Ia host galaxies (M101, M66, M96, NGC 4038/39 and NGC 5584), as listed in Table 6.4, applying the revised TRGB calibration.

- We compared our TRGB distance estimates with the Cepheid distance estimates presented in Riess et al. (2011) and Riess et al. (2016), obtaining $\Delta(m-M)_0(\mathrm{TRGB}-\mathrm{Cepheid}) = 0.027 \pm 0.045$ mag for five common galaxies in Riess et al. (2011), 0.038 ± 0.037 mag for six common galaxies in Riess et al. (2016), and 0.006 ± 0.038 mag for five galaxies (excluding NGC 4038/39) in Riess et al. (2016).

- From the mean absolute peak magnitude of the six low-reddened SNe Ia and the recent SN Ia calibration in Riess et al. (2016), we derive our best estimate of the Hubble constant: $H_0 = 70.45 \pm 1.67(\mathrm{random}) \pm 1.56(\mathrm{systematic})$ km s^{-1} Mpc^{-1}. This estimate is between the values from the Cepheid calibrated SNe Ia (Riess et al. 2011; Freedman et al. 2012; Riess et al. 2016) and those from the CMB analysis (Bennett et al. 2013; Planck Collaboration et al. 2015). This alleviates the Hubble tension between the Cepheid results and CMB results.

This Chapter has been submitted to *The Astrophysical Journal* as Jang & Lee 2016.

Chapter 7

Summary and Conclusion

In this thesis, We focused on the calibration of SNe Ia and the Hubble constant based on the TRGB. We present the TRGB distance estimates to eight SN Ia host galaxies. from the photometry of archival HST images (Chapter 2, 3, 4, and 6). We also provide a revised TRGB calibration accurate to 2.3% of distance (Chapter 5).

In Chapter 2, we present a new determination of the distance to M101, host of the SN 2011fe, using the TRGB method from the F555W and F814W images of nine fields within this galaxy in the HST archive. Primary results are as follows.

- CMDs of arm-free regions in all HST/ACS fields show a prominent RGB.
- We measured the I-band magnitude of the TRGB, obtaining a mean value of $I_{TRGB} = 25.28 \pm 0.01$ with a standard deviation of 0.02 mag. From this we derive a weighted mean value of distance modulus $(m - M)_0 = 29.30 \pm 0.01$(random) mag with a systematic uncertainty of 0.12 mag (corresponding to 7.24 ± 0.03(random) ± 0.40(systematic) Mpc).
- With this distance value we derive the optical and NIR absolute maximum magnitudes of SN 2011fe (at the maximum of each band and at the B-band maximum time). Absolute magnitudes of SN 2011fe are ~ 0.2 mag brighter in the optical band and much more in the NIR than the recent calibrations of

SN Ia in the literature.

- From the optical magnitude of SN 2011fe and our distance measurement for M101 we obtain a value of the Hubble constant, $H_0 = 65.0 \pm 0.5$(random) $\pm$ 5.7(systematic) km s^{-1} Mpc^{-1}.

In Chapter 3, we present VI photometry of resolved stars in two spiral galaxies m66 and M96 that host SNe Ia in the Leo I group, derived from HST/ACS F555W and F814W images. Then we estimate the distances to these two galaxies applying the TRGB method to this photometry. We summarize main results in the following.

- Most of the resolved stars in the selected regions of M66 and M96 are red giants, allowing us to determine the distances to these galaxies.

- The I-band magnitudes of the TRGB are found to be $I_{TRGB} = 26.20 \pm 0.03$ for M66 and 26.21 ± 0.03 for M96. These TRGB magnitudes yield distance modulus $(m - M)_0 = 30.12 \pm 0.03$(random) $\pm$ 0.12(systematic) for M66 and $(m - M)_0 = 30.15 \pm 0.03$(random) $\pm$ 0.12(systematic) for M66. These result shows that M66 and M96 are the members of the same group.

- Combining the results for SN 1989B and Sn 1998bu with those for SN 2011fe in M101 based on the same method given in Chapter 2, we obtain an estimate of the Hubble constant, $H_0 = 68.4 \pm 2.6$(random) $\pm$ 3.7(systematic) km s^{-1} Mpc^{-1}.

Chapter 4 presents the TRGB distances to two additional SN Ia host galaxies, NGC 4039/39 and 5584 from the PSF photometry of archival HST images. A summary of main results is as follows.

- We detected RGB stars in the outer regions of NGC 4038/39 and NGC 5584 based on the combined archival ACS/WFC and WFC3/UVIS image data.

- We derived photometric transformation between F555W and F814W bands of WFC3/UVIS and that of ACS/WFC, by comparing the photometry of the resolved stars in two galactic globular clusters, NGC 2419 and 47 Tuc.

- We found I-band TRGB magnitudes to be at $I_{TRGB} = 27.67 \pm 0.05$ for NGC 4038/39 and $I_{TRGB} = 27.77 \pm 0.04$ for NGC 5584. From these, we derived the TRGB distance estimates of $(m-M)_0 = 31.67 \pm 0.05$(random) $\pm$ 0.12(systematic) for NGC 4038.39 and $(m-M)_0 = 31.76 \pm 0.04$(random) $\pm$ 0.12(systematic) for NGC 5584.

- based on distance estimates for the two SNe in this study and those of the three SNe in our previous studies, we calibrated the V-band peak absolute magnitudes of SNe Ia.

- From the mean absolute magnitudes of five SNe Ia, the Hubble constant is determined to be $H_0 = 69.8 \pm 2.6$(random) $\pm$ 3.9(systematic) km s^{-1} Mpc^{-1}, which is similar to the values from the CMBR analysis, $H_0 = 69$ km s^{-1} Mpc^{-1}(Bennett et al. 2013; Planck Collaboration et al. 2015). Our estimate is slightly smaller, but agrees within errors with the values from the recent calibrations of SNE Ia with the Cepheid variables, $H_0 = 74$ km s^{-1} Mpc^{-1}(Riess et al. 2011; Freedman et al. 2012). If we adopt three low-reddened SNe, corresponding the Hubble constant is slightly increased, $H_0 = 72.2 \pm 3.3$(random) $\pm$ 4.0(systematic) km s^{-1} Mpc^{-1}.

In Chapter 5, we present a revised TRGB calibration including the color dependence and zero-point calibrations, accurate to 0.046 mag (2.3% of distance). Primary results are as follows.

- We obtained deep VI photometry of the resolved stars in eight nearby galaxies from the archival *HST/ACS* images. By applying quantitative TRGB detections on F814W $-$ (F606W $-$ F814W)$_0$ CMDs, we derived color-luminosity relation of the TRGB, which is described by a quadratic equation.

- From the photometry of two nearby globular clusters (NGC 2419 and 47 Tuc), we derived color transformation between F555W − F814W and F606W − F814W in ACS/WFC system.

- The zero-point of the TRGB was determined from the photometry of two nearby galaxies, NGC 4258 and the LMC, to which geometric distances are known. A weighed mean of two zero-points is $M_{I,TRGB} = -4.078 \pm 0.046$ mag.

- We carried out PSF photometry using five different reduction methods on the HST/ACS field of NGC 4258 and compared the results. We fount that output magnitudes agree well within 0.06 mag at the TRGB magnitude level. Especially, F814W band photometry shows excellent agreement within 0.02 mag, regardless of reduction methods.

- We provide the revised TRGB calibration in several filter systems including Johnson-Cousins, ACS/WFC, WFC3/UVIS and WFPC2.

In Chapter 6, we determine TRGB distances to three SN Ia host galaxies: NGC 3021 hosting SN 1995al, NGC 3370 hosting SN 1994ae, and NGC 1309 hosting SN 2002fk. Primary results are as follows.

- We find a significant number of old RGB stars in the halo regions of the three galaxies, presenting their CMDs.

- Applying the revised TRGB calibration introduced in Chapter 5, we measured the TRGB magnitudes, obtaining $QT_{RGB} = 28.152 \pm 0.046$ for NGC 3021, 28.208 ± 0.052 for NGC 3370 and 28.398 ± 0.048 for NGC 1309. From these we derive TRGB distances: $(m - M)_0 = 32.229 \pm 0.046$ for NGC 3021, 32.285 ± 0.052 for NGC 3370 and 32.475 ± 0.048 for NGC 1309.

- We updated our previous distance estimates to five SN Ia host galaxies (M101, M66, M96, NGC 4038/39 and NGC 5584), applying the revised TRGB calibration.

- We compared our TRGB distances estimates with the Cepheid distance estimates presented in Riess et al. (2011) and Riess et al. (2016), obtaining $\Delta(m-M)_0 = 0.004 \pm 0.048$ mag for five common galaxies in Riess et al. (2011), and 0.046 ± 0.041 mag for five galaxies (excluding NGC 4038/39) in-Riess et al. (2016).

- From the mean absolute peak magnitude of the six low-reddened SNe Ia and the recent Sn Ia calibration in Riess et al. (2016), we derive our best estimate of the Hubble constant: $H_0 = 70.45 \pm 1.67(\text{random}) \pm 1.56(\text{systematic})$ km s^{-1} Mpc^{-1}. This estimate is between the values from the Cepheid calibrated SNe Ia (Riess et al. 2011; Freedman et al. 2012; Riess et al. 2016) and those from the CMB analysis (Bennett et al. 2013; Planck Collaboration et al. 2015). This alleviates the Hubble tension between the Cepheid results and CMB results.

Figure 7.1 displays a distribution of recent estimations of H_0 as a function of time. A systematic offset between the values from the Cepheid calibrated SNe Ia (pentagons) and those from the CMBR analysis (open circles) are seen. Our initial estimate based on a single SN Ia, SN 2011fe, yielded a significantly low value of H_0 (Lee & Jang 2012). Our estimates are getting increased by adding two and four SNe Ia (Lee & Jang 2013; Jang & Lee 2015). Our best estimate from the six low-reddened SNe Ia is $H_0 = 70.45 \pm 1.67(\text{random}) \pm 1.56(\text{systematic})$ km s^{-1} Mpc^{-1}(Jang & Lee 2016). It agrees within $\sim 1\sigma$ level with the two recent estimations: $H_0 = 73.02 \pm 1.79$ km s^{-1} Mpc^{-1} based on the Cepheid calibrated SNe Ia (Riess et al. 2016) and $H_0 = 67.8 \pm 0.9$ km s^{-1} Mpc^{-1} based on the CMDR analysis (Planck Collaboration et al. 2015).

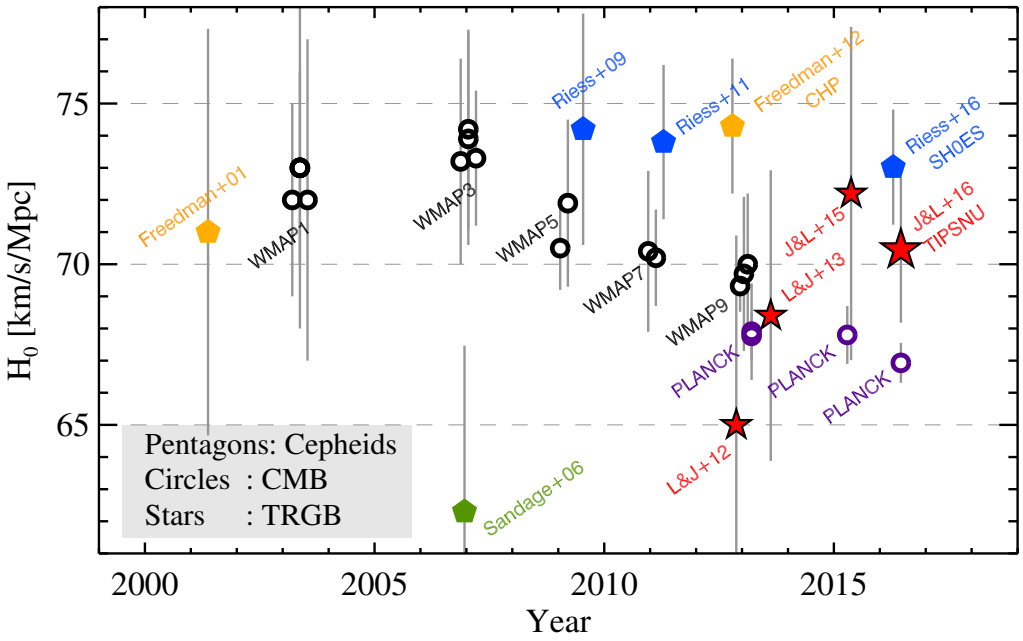

Figure 7.1: Comparison of recent values of the Hubble Constant based on the TRGB calibration of SN Ia (starlets), the Cepheid calibration of SN Ia (pentagons), and the WMAP and PLANCK CMBR results (circles). Note that our best TRGB estimate in this study is between the 2016 Cepheid value and the 2015 Planck value.

Bibliography

Addison, G. E., Huang, Y., Watts, D. J., et al. 2016, ApJ, 818, 132

Ajhar, E. A., Tonry, J. L., Blakeslee, J. P., Riess, A. G., & Schmidt, B. P. 2001, ApJ, 559, 584

Amanullah, R., Lidman, C., Rubin, D., et al. 2010, ApJ, 716, 712

Argon, A. L., Greenhill, L. J., Reid, M. J., Moran, J. M., & Humphreys, E. M. L. 2007, ApJ, 659, 1040

Aubourg, É., Bailey, S., Bautista, J. E., et al. 2014, arXiv:1411.1074

Aubourg, É., Bailey, S., Bautista, J. E., et al. 2015, Phys. Rev. D, 92, 123516

Baade, W. 1938, ApJ, 88, 285

Baade, W. 1944, ApJ, 100, 137

Barbon, R., Capaccioli, M., & Ciatti, F. 1975, A&A, 44, 267

Barone-Nugent, R. L., Lidman, C., Wyithe, J. S. B., et al. 2012, MNRAS, 425, 1007

Beaton, R. L., Freedman, W. L., Madore, B. F., et al. 2016, arXiv:1604.01788

Bellazzini, M., Ferraro, F. R., & Pancino, E. 2001, ApJ, 556, 635

Bellazzini, M., Ferraro, F. R., Sollima, A., Pancino, E., & Origlia, L. 2004, A&A, 424, 199

Bellazzini, M. 2008, Mem. Soc. Astron. Italiana, 79, 440

Bennett, C. L., Larson, D., Weiland, J. L., et al. 2012, arXiv:1212.5225

Bennett, C. L., Larson, D., Weiland, J. L., et al. 2013, ApJS, 208, 20

Bennett, C. L., Larson, D., Weiland, J. L., & Hinshaw, G. 2014, ApJ, 794, 135

Bird, J. C., Stanek, K. Z., & Prieto, J. L. 2009, ApJ, 695, 874

Bloom, J. S., Kasen, D., Shen, K. J., et al. 2012, ApJ, 744, L17

Branch, D., & Bettis, C. 1978, AJ, 83, 224

Branch, D., & Tammann, G. A. 1992, ARA&A, 30, 359

Brown, P. J., Roming, P. W. A., Milne, P., et al. 2010, ApJ, 721, 1608

Burns, C. R., Stritzinger, M., Phillips, M. M., et al. 2011, AJ, 141, 19

Cadonau, R., Tammann, G. A., & Sandage, A. 1985, Supernovae as Distance Indicators, 224, 151

Capaccioli, M., Cappellaro, E., della Valle, M., et al. 1990, ApJ, 350, 110

Carretta, E., Gratton, R. G., Clementini, G., & Fusi Pecci, F. 2000, ApJ, 533, 215

Cassisi, S., Potekhin, A. Y., Pietrinferni, A., Catelan, M., & Salaris, M. 2007, ApJ, 661, 1094

Ciardullo, R., Feldmeier, J. J., Jacoby, G. H., et al. 2002, ApJ, 577, 31

Ciatti, F., & Rosino, L. 1977, A&A, 56, 59

Conn, A. R., Lewis, G. F., Ibata, R. A., et al. 2011, ApJ, 740, 69

Conn, A. R., Ibata, R. A., Lewis, G. F., et al. 2012, ApJ, 758, 11

Courtois, H. M., & Tully, R. B. 2012, ApJ, 749, 174

Da Costa, G. S., & Armandroff, T. E. 1990, AJ, 100, 162

Dalcanton, J. J., Williams, B. F., Seth, A. C., et al. 2009, ApJS, 183, 67

de Bruijne, J. H. J., Rygl, K. L. J., & Antoja, T. 2014, EAS Publications Series, 67, 23

de Grijs, R., Wicker, J. E., & Bono, G. 2014, AJ, 147, 122

de Vaucouleurs, G. 1975, in Stars and Stellar Systems 9 : Galaxies and the Universe, ed. A. Sandage, M. Sandage, & J. Kristian (Chicago : Univ. Chicago Press), 557

de Vaucouleurs, G., & Peters, W. L. 1981, ApJ, 248, 395

de Vaucouleurs, G. 1993, ApJ, 415, 10

Dolphin, A. E. 2000, PASP, 112, 1383

Dotter, A., Chaboyer, B., Jevremović, D., et al. 2008, ApJS, 178, 89

Dolphin, A. E., & Kennicutt, R. C., Jr. 2002, AJ, 123, 207

Drake, A. J., Djorgovski, S. G., Williams, R., et al. 2007, Central Bureau Electronic Telegrams, 1172, 1

Efstathiou, G. 2014, MNRAS, 440, 1138

Elias-Rosa, N., Van Dyk, S. D., Li, W., et al. 2011, ApJ, 742,

Evans, R. O., & McNaught, R. H. 1989, IAU Circ., 4726, 1

Feldmeier, J. J., Ciardullo, R., & Jacoby, G. H. 1997, ApJ, 479, 231

Ferrarese, L., Mould, J. R., Kennicutt, R. C., Jr., et al. 2000, ApJ, 529, 745

Fiorentino, G., Clementini, G., Marconi, M., et al. 2012, Ap&SS, 341, 143

Fiorentino, G., Musella, I., & Marconi, M. 2013, MNRAS, 434, 2866

Folatelli, G., Phillips, M. M., Burns, C. R., et al. 2010, AJ, 139, 120

Freedman, W. L. 1988, ApJ, 326, 691

Freedman, W. L. 1988, AJ, 96, 1248

Freedman, W. L. 1989, AJ, 98, 1285

Freedman, W. L., Madore, B. F., Gibson, B. K., et al. 2001, ApJ, 553, 47

Freedman, W. L., & Madore, B. F. 2010, ARA&A, 48, 673

Freedman, W. L., Madore, B. F., Scowcroft, V., et al. 2012, ApJ, 758, 24

Frogel, J. A., Cohen, J. G., & Persson, S. E. 1983, ApJ, 275, 773

Fukugita, M., & Hogan, C. J. 1991, ApJ, 368, L11

Fusco, F., Buonanno, R., Bono, G., et al. 2012, A&A, 548, A129

Geha, M., Weisz, D., Grocholski, A., et al. 2015, ApJ, 811, 114

Gerke, J. R., Kochanek, C. S., Prieto, J. L., Stanek, K. Z., & Macri, L. M. 2011, ApJ, 743, 176

Gibson, B. K., Stetson, P. B., Freedman, W. L., et al. 2000, ApJ, 529, 723

Gibson, B. K., & Stetson, P. B. 2001, ApJ, 547, L103

Girardi, L., Bressan, A., Bertelli, G., & Chiosi, C. 2000, A&AS, 141, 371

Girardi, L., Barbieri, M., Groenewegen, M. A. T., et al. 2012, Red Giants as Probes of the Structure and Evolution of the Milky Way, 165

Green, E. M., Demarque, P., & King, C. R. 1987, The revised Yale isochrones and luminosity functions, New Haven: Yale Observatory, 1987,

Greenhill, L. J., Jiang, D. R., Moran, J. M., et al. 1995, ApJ, 440, 619

Guy, J., Astier, P., Nobili, S., Regnault, N., & Pain, R. 2005, A&A, 443, 781

Guy, J., Astier, P., Baumont, S., et al. 2007, A&A, 466, 11

Guy, J., Sullivan, M., Conley, A., et al. 2010, A&A, 523, A7

Hamuy, M., Folatelli, G., Morrell, N. I., et al. 2006, PASP, 118, 2

Harris, W. E., Harris, G. L. H., Layden, A. C., & Stetson, P. B. 2007, AJ, 134, 43

Harris, W. E., Harris, G. L. H., Layden, A. C., & Wehner, E. M. H. 2007, ApJ, 666, 903

Haschke, R., Grebel, E. K., & Duffau, S. 2011, AJ, 141, 158

Hernandez, M., Meikle, W. P. S., Aparicio, A., et al. 2000, MNRAS, 319, 223

Herrera, C. N., Boulanger, F., Nesvadba, N. P. H., & Falgarone, E. 2012, A&A, 538, L9

Herrnstein, J. R., Moran, J. M., Greenhill, L. J., et al. 1999, Nature, 400, 539

Hicken, M., Challis, P., Jha, S., et al. 2009, ApJ, 700, 331

Hislop, L., Mould, J., Schmidt, B., et al. 2011, ApJ, 733, 75

Humphreys, E. M. L., Argon, A. L., Greenhill, L. J., Moran, J. M., & Reid, M. J. 2005, Future Directions in High Resolution Astronomy, 340, 466

Humphreys, E. M. L., Reid, M. J., Greenhill, L. J., Moran, J. M., & Argon, A. L. 2008, ApJ, 672, 800

Humphreys, E. M. L., Reid, M. J., Moran, J. M., Greenhill, L. J., & Argon, A. L. 2013, ApJ, 775, 13

Illingworth, G. D., Magee, D., Oesch, P. A., et al. 2013, ApJS, 209, 6

Jang, I. S., Lim, S., Park, H. S., & Lee, M. G. 2012, ApJ, 751, L19

Jang, I. S., & Lee, M. G. 2014, ApJ, 792, 52

Jang, I. S., & Lee, M. G. 2015, ApJ, 807, 133 (Paper III)

Jang, I. S., & Lee, M. G. 2016, ApJ, Submitted (Paper IV)

Jensen, J. B., Tonry, J. L., Barris, B. J., et al. 2003, ApJ, 583, 712

Jha, S., Garnavich, P. M., Kirshner, R. P., et al. 1999, ApJS, 125, 73

Jha, S., Riess, A. G., & Kirshner, R. P. 2007, ApJ, 659, 122

Kattner, S., Leonard, D. C., Burns, C. R., et al. 2012, PASP, 124, 114

Kanbur, S. M., Ngeow, C., Nikolaev, S., Tanvir, N. R., & Hendry, M. A. 2003, A&A, 411, 361

Karachentsev, I. D., & Makarov, D. A. 1996, AJ, 111, 794

Kelson, D. D., Illingworth, G. D., Freedman, W. F., et al. 1996, ApJ, 463, 26

Kelson, D. D., Illingworth, G. D., Tonry, J. L., et al. 2000, ApJ, 529, 768

Kennicutt, R. C., Jr., Stetson, P. B., Saha, A., et al. 1998, ApJ, 498, 181

Kochanek, C. S. 1997, ApJ, 491, 13

Komatsu, E., Smith, K. M., Dunkley, J., et al. 2011, ApJS, 192, 18

Kowal, C. T. 1968, AJ, 73, 1021

Krisciunas, K., Phillips, M. M., & Suntzeff, N. B. 2004, ApJ, 602, L81

Lagattuta, D. J., Mould, J. R., Staveley-Smith, L., et al. 2013, ApJ, 771, 88

Leavitt, H. S. 1908, Annals of Harvard College Observatory, 60, 87

Leavitt, H. S., & Pickering, E. C. 1912, Harvard College Observatory Circular, 173, 1

Lee, M. G., Freedman, W. L., & Madore, B. F. 1993, ApJ, 417, 553

Lee, M. G., & Jang, I. S. 2012, ApJ, 760, L14 (Paper I)

Lee, M. G., & Jang, I. S. 2013, ApJ, 773, 13 (Paper II)

Lee, M. G., & Jang, I. S. 2016, arXiv:1601.06798

Liu, J., Di Stefano, R., Wang, T., & Moe, M. 2012, ApJ, 749, 141

Macri, L. M., Calzetti, D., Freedman, W. L., et al. 2001, ApJ, 549, 721

Macri, L. M., Stanek, K. Z., Bersier, D., Greenhill, L. J., & Reid, M. J. 2006, ApJ, 652, 1133

Macri, L. M., Ngeow, C.-C., Kanbur, S. M., Mahzooni, S., & Smitka, M. T. 2015, AJ, 149, 117

Madore, B. F., & Freedman, W. L. 1995, AJ, 109, 1645

Madore, B. F., Mager, V., & Freedman, W. L. 2009, ApJ, 690, 389

Mager, V. A., Madore, B. F., & Freedman, W. L. 2008, ApJ, 689, 721

Makarov, D., Makarova, L., Rizzi, L., et al. 2006, AJ, 132, 2729

Mandel, K. S., Wood-Vasey, W. M., Friedman, A. S., & Kirshner, R. P. 2009, ApJ, 704, 629

Mandel, K. S., Narayan, G., & Kirshner, R. P. 2011, ApJ, 731, 120

Marigo, P., Girardi, L., Bressan, A., et al. 2008, A&A, 482, 883

Matheson, T., Joyce, R. R., Allen, L. E., et al. 2012, ApJ, 754, 19

Méndez, B., Davis, M., Moustakas, J., et al. 2002, AJ, 124, 213

Michel-Dansac, L., Duc, P.-A., Bournaud, F., et al. 2010, ApJ, 717, L143

Miyoshi, M., Moran, J., Herrnstein, J., et al. 1995, Nature, 373, 127

Mouhcine, M., Harris, W. E., Ibata, R., & Rejkuba, M. 2010, MNRAS, 404, 1157

Mould, J. R., Kristian, J., & Da Costa, G. S. 1983, ApJ, 270, 471

Mould, J., Kristian, J., & Da Costa, G. S. 1984, ApJ, 278, 575

Mould, J., & Kristian, J. 1986, ApJ, 305, 591

Mould, J., & Sakai, S. 2009a, ApJ, 694, 1331

Mould, J., & Sakai, S. 2009b, ApJ, 697, 996

Mueller, E., & Hoeflich, P. 1994, A&A, 281, 51

Naito, H., Sakane, Y., Anan, T., Kouzuma, S., & Yamaoka, H. 2007, Central Bureau Electronic Telegrams, 1173, 1

Nowak, N., Thomas, J., Erwin, P., et al. 2010, MNRAS, 403, 646

Nugent, P. E., Sullivan, M., Cenko, S. B., et al. 2011, Nature, 480, 344

Patat, F., Cordiner, M. A., Cox, N. L. J., et al. 2011, arXiv:1112.0247

Paturel, G., Teerikorpi, P., Theureau, G., et al. 2002, A&A, 389, 19

Pereira, R., Thomas, R. C., Aldering, G., et al. 2013, A&A, 554, AA27

Perlmutter, S., Aldering, G., Goldhaber, G., et al. 1999, ApJ, 517, 565

Phillips, M. M. 1993, ApJ, 413, L105

Phillips, M. M., Lira, P., Suntzeff, N. B., et al. 1999, AJ, 118, 1766

Phillips, M. M., Simon, J. D., Morrell, N., et al. 2013, ApJ, 779, 38

Pierce, M. J. 1994, ApJ, 430, 53

Pietrinferni, A., Cassisi, S., Salaris, M., & Castelli, F. 2004, ApJ, 612, 168

Pietrinferni, A., Cassisi, S., Salaris, M., & Castelli, F. 2006, ApJ, 642, 797

Pietrzyński, G., Graczyk, D., Gieren, W., et al. 2013, Nature, 495, 76

Planck Collaboration, Ade, P. A. R., Aghanim, N., et al. 2013, arXiv:1303.5076

Planck Collaboration, Ade, P. A. R., Aghanim, N., et al. 2014, A&A, 571, AA16

Planck Collaboration, Ade, P. A. R., Aghanim, N., et al. 2015, arXiv:1502.01589

Pojmanski, G., 1997, Acta Astronomica, 47, 467 The All Sky Automated Survey

Popowski, P., & Gould, A. 1998, ApJ, 506, 259

Popowski, P., & Gould, A. 1998, ApJ, 506, 271

Radburn-Smith, D. J., de Jong, R. S., Seth, A. C., et al. 2011, ApJS, 195, 18

Reindl, B., Tammann, G. A., Sandage, A., & Saha, A. 2005, ApJ, 624, 532

Ribas, I., Jordi, C., Vilardell, F., et al. 2005, ApJ, 635, L37

Richmond, M. W., & Smith, H. A. 2012, arXiv:1203.4013

Riess, A. G., Press, W. H., & Kirshner, R. P. 1995, ApJ, 438, L17

Riess, A. G., Filippenko, A. V., Challis, P., et al. 1998, AJ, 116, 1009

Riess, A. G., Kirshner, R. P., Schmidt, B. P., et al. 1999, AJ, 117, 707

Riess, A. G., Li, W., Stetson, P. B., et al. 2005, ApJ, 627, 579

Riess, A. G., Macri, L., Li, W., et al. 2009, ApJS, 183, 109

Riess, A. G., Macri, L., Casertano, S., et al. 2009, ApJ, 699, 539

Riess, A. G., Macri, L., Casertano, S., et al. 2011, ApJ, 730, 119

Riess, A. G., Macri, L., Casertano, S., et al. 2012, ApJ, 752, 76

Riess, A. G., Macri, L. M., Hoffmann, S. L., et al. 2016, arXiv:1604.01424

Rizzi, L., Tully, R. B., Makarov, D., et al. 2007, ApJ, 661, 815

Röpke, F. K., Kromer, M., Seitenzahl, I. R., et al. 2012, ApJ, 750, L19

Russell, D. G. 2002, ApJ, 565, 681

Saha, A., Sandage, A., Tammann, G. A., et al. 1999, ApJ, 522, 802

Saha, A., Thim, F., Tammann, G. A., et al. 2006, ApJS, 165, 108

Saha, A., Shaw, R. A., Claver, J. A., & Dolphin, A. E. 2011, PASP, 123, 481

Sakai, S., Madore, B. F., & Freedman, W. L. 1996, ApJ, 461, 713

Sakai, S., Ferrarese, L., Kennicutt, R. C., Jr., & Saha, A. 2004, ApJ, 608, 42

Salaris, M., & Cassisi, S. 1997, MNRAS, 289, 406

Salaris, M. 2011, Ap&SS, 714

Sandage, A. R. 1971, Study Week on Nuclei of Galaxies, 601

Sandage, A., & Tammann, G. A. 1974, ApJ, 190, 525

Sandage, A., & Tammann, G. A. 1974, ApJ, 191, 603

Sandage, A., & Tammann, G. A. 1974, ApJ, 194, 223

Sandage, A., & Tammann, G. A. 1974, ApJ, 194, 559

Sandage, A., & Tammann, G. A. 1975, ApJ, 196, 313

Sandage, A., & Tammann, G. A. 1975, ApJ, 197, 265

Sandage, A., & Tammann, G. A. 1976, ApJ, 210, 7

Sandage, A., & Tammann, G. A. 1982, ApJ, 256, 339

Sandage, A., & Tammann, G. A. 1993, ApJ, 415, 1

Sandage, A., Saha, A., Tammann, G. A., et al. 1994, ApJ, 423, L13

Sandage, A., Tammann, G. A., Saha, A., et al. 2006, ApJ, 653, 843

Saviane, I., Hibbard, J. E., & Rich, R. M. 2004, AJ, 127, 660

Saviane, I., Momany, Y., da Costa, G. S., Rich, R. M., & Hibbard, J. E. 2008, ApJ, 678, 179-186

Savitzky, A., & Golay, M. J. E. 1964, Analytical Chemistry, 36, 1627

Schaefer, B. E. 2008, AJ, 135, 112

Schlafly, E. F., & Finkbeiner, D. P. 2011, ApJ, 737, 103

Schlegel, D. J., Finkbeiner, D. P., & Davis, M. 1998, ApJ, 500, 525

Schneider, S. E., Helou, G., Salpeter, E. E., & Terzian, Y. 1983, ApJ, 273, L1

Schneider, S. E. 1989, ApJ, 343, 94

Schweizer, F., Burns, C. R., Madore, B. F., et al. 2008, AJ, 136, 1482

Shappee, B. J., & Stanek, K. Z. 2011, ApJ, 733, 124

Simon, J. D., Gal-Yam, A., Penprase, B. E., et al. 2007, ApJ, 671, L25

Sirianni, M., Jee, M. J., Benítez, N., et al. 2005, PASP, 117, 1049

Sorce, J. G., Tully, R. B., & Courtois, H. M. 2012, ApJ, 758, L12

Sorce, J. G., Tully, R. B., Courtois, H. M., et al. 2014, MNRAS, 444, 527

Spergel, D. N., Verde, L., Peiris, H. V., et al. 2003, ApJS, 148, 175

Spergel, D. N., Bean, R., Doré, O., et al. 2007, ApJS, 170, 377

Springob, C. M., Masters, K. L., Haynes, M. P., Giovanelli, R., & Marinoni, C. 2009, ApJS, 182, 474

Spyromilio, J., Gilmozzi, R., Sollerman, J., et al. 2004, A&A, 426, 547

Stetson, P. B. 1987, PASP, 99, 191

Stetson, P. B. 1994, PASP, 106, 250

Stetson, P. B. 1998, PASP, 110, 1448

Stetson, P. B., Saha, A., Ferrarese, L., et al. 1998, ApJ, 508, 491

Suntzeff, N. B., Phillips, M. M., Covarrubias, R., et al. 1999, AJ, 117, 1175

Suzuki, N., Rubin, D., Lidman, C., et al. 2012, ApJ, 746, 85

Takanashi, N., Doi, M., & Yasuda, N. 2008, MNRAS, 389, 1577

Tammann, G. A., & Leibundgut, B. 1990, A&A, 236, 9

Tammann, G. A., Sandage, A., & Reindl, B. 2008, ApJ, 679, 52

Tammann, G. A., & Reindl, B. 2012, A&A, in press (arXiv:1208.5054)

Tammann, G. A., & Reindl, B. 2013, A&A, 549, 136

Tanvir, N. R., Shanks, T., Ferguson, H. C., & Robinson, D. R. T. 1995, Nature, 377, 27

Tanvir, N. R., Ferguson, H. C., & Shanks, T. 1999, MNRAS, 310, 175

Theureau, G., Hanski, M. O., Coudreau, N., Hallet, N., & Martin, J.-M. 2007, A&A, 465, 71

Thilker, D. A., Donovan, J., Schiminovich, D., et al. 2009, Nature, 457, 990

Thompson, I. B., Kaluzny, J., Pych, W., et al. 2001, AJ, 121, 3089

Tonry, J. L., Blakeslee, J. P., Ajhar, E. A., & Dressler, A. 2000, ApJ, 530, 625

Tonry, J. L., Dressler, A., Blakeslee, J. P., et al. 2001, ApJ, 546, 681

Tully, R. B., Rizzi, L., Shaya, E. J., et al. 2009, AJ, 138, 323

Tully, R. B., Courtois, H. M., Dolphin, A. E., et al. 2013, AJ, 146, 86

Ulaczyk, K., Szymański, M. K., Udalski, A., et al. 2012, Acta Astron, 62, 247

Umbriaco, G., Pietrogrande, T., di Mille, F., et al. 2007, Central Bureau Electronic

van den Bergh, S. 1960, ZAp, 49, 198

van den Bergh, S. 1960, JRASC, 54, 49

van den Bergh, S. 1975, Galaxies and the Universe, 509

van den Bergh, S., & Pazder, J. 1992, ApJ, 390, 34

van den Bergh, S. 1994, PASP, 106, 1113

Van Dyk, S. D., Peng, C. Y., King, J. Y., et al. 2000, PASP, 112, 1532

Vilardell, F., Ribas, I., Jordi, C., Fitzpatrick, E. L., & Guinan, E. F. 2010, A&A, 509, A70

Villi, M., Nakano, S., Aoki, M., Skiff, B. A., & Hanzl, D. 1998, IAU Circ., 6899, 1

Vinko, J., Sarneczky, K., Takats, K., et al. 2012, A&A, 546, 12

Wang, X., Wang, L., Pain, R., Zhou, X., & Li, Z. 2006, ApJ, 645, 488

Wells, L. A., Phillips, M. M., Suntzeff, B., et al. 1994, AJ, 108, 2233

Whitmore, B. C., Chandar, R., Schweizer, F., et al. 2010, AJ, 140, 75

Willick, J. A., & Batra, P. 2001, ApJ, 548, 564

Wood-Vasey, W. M., Friedman, A. S., Bloom, J. S., et al. 2008, ApJ, 689, 377

Yang, S.-C., Wagner-Kaiser, R., Sarajedini, A., Kim, S. C., & Kyeong, J. 2014, ApJ, 784, 76

Zaritsky, D., Hill, J. M., & Elston, R. 1990, AJ, 99, 1108

초 록

먼 거리에 위치한 은하는 가까운 거리에 위치한 은하들 보다 더 빠른 후퇴속도를 보여준다. 이를 허블의 법칙이라고 부른다. 허블의 법칙에서 은하의 속도와 거리 사이의 비례상수를 허블상수라고 부른다. 우주의 크기와 나이는 허블상수 값을 통해 유추될 수 있다. 그렇기 때문에 정확하고 정밀한 허블상수 값을 알아내는 일은 외부은하 천문학과 우주론에 있어 핵심적인 단계이다. 지난 수십 년 동안 많은 연구가 수행되어 왔지만, 정확한 허블상수 값은 아직도 불분명하다.

제 1a형 초신성은 초신성의 하위 범주 중 하나로, 백색왜성이 터진 결과물이다. 제 1a형 초신성은 밝고 ($M_V \sim -19.3$), 또 최대광도의 분산이 크지 않기 때문에 ($\sigma \lesssim 0.14$) 외부은하의 거리와 허블상수 값을 측정하는데 유용하게 사용될 수 있다. 제 1a형 초신성의 광도를 측정하여 허블상수를 측정하는 선행연구들이 여러 차례 수행되었다. 초신성의 광도측정에는 세페이드 변광성이 주로 사용되었다. 하지만 제 1a형 초신성을 통해 결정된 허블상수 값은 우주배경복사를 이용하여 결정된 허블상수 값과 $2 \sim 3\sigma$ 정도의 차이가 있다. 이러한 허블상수 값의 불일치는 현대우주론에서 해결해야 할 문제 중 하나이다. 적색거성가지 최대밝기 (the tip of the red giant branch) 방법은 외부은하까지의 거리를 가장 정밀하게 측정하는 방법 중 하나이다. 이 방법은 기존에 주로 사용되었던 세페이드 변광성과 비교해 볼 때 몇 가지 장점이 있다. 적색거성가지 최대밝기 방법을 이용하면 제 1a형 초신성의 광도와 허블상수를 더 정밀하게 측정할 수 있을 것으로 예상된다.

본 연구에서는 적색거성가지 최대밝기 방법을 이용하여 제 1a형 초신성의 최대광도를 측정하였다. 기존에 수행된 연구들 보다 더 정밀한 적색거성가지 최대밝기 측정을 위해 금속함량이 보정된 등급, QT등급을 고안하고 적용하였다. 적색거성가지 별들의 색(금속함량)에 따른 밝기 변화는 허블우주망원경으로 관측된 8개 은하의 영상자료를 분석하여 결정하였다. 적색거성가지의 최대밝기는 거리가 비교적 잘 알려진 두 개의 은하, NGC 4258과 대 마젤란 은하 (LMC)를 이용하였다. 이를 통해 도출된 값은 NGC 4258의 경우 $M_{I,TRGB} = -4.121 \pm 0.067$, 대 마젤란 은하의 경우 $M_{I,TRGB} = -4.033 \pm 0.063$, 그리고 두 은하를 모두 사용했을 경우 $M_{I,TRGB} = -4.074 \pm 0.046$ 이다. 두 은하를 사용하여 도출한 최대밝기는 기존 연

구에서 측정한 값과 비슷하다. 하지만 최대밝기의 오차는 기존연구에서 도출한 오차보다 2 ∼ 3배 더 작다.

개선된 적색거성가지 최대밝기 방법을 이용하여 제 1a형 초신성이 발견된 은하까지의 거리를 측정하였다. 측정에는 총 8개 은하가 사용되었다: SN 2011fe가 발견된 M101, SN 1989B가 발견된 M66, SN 1998bu가 발견된 M96, SN 2007sr이 발견된 NGC 4038/39, SN 2007af가 발견된 NGC 5584, SN 1995al이 발견된 NGC3021, SN 1994ae가 발견된 NGC 3370, 그리고 SN 2002fk가 발견된 NGC 1309. 8개 은하에서 관측된 적색거성 별들의 광도함수는 분명한 적색거성가지 최대밝기의 위치를 보여준다. 측정된 값은 $QT = 25.083 \pm 0.034$(M101) 과 28.398 ± 0.048(NGC 1309) 사이에 분포한다. 도출된 적색거성 최대밝기를 이용하여 거리를 측정하였다. 측정된 거리지수는 $(m - M)_0 = 26.168 \pm 0.034$(M101) 과 32.475 ± 0.048(NGC 1309) 사이의 값을 보여준다. 본 연구에서 도출한 제 1a형 초신성 모은하까지의 거리와 Riess et al. (2011)에서 제시하는 제 1a형 초신성의 보정식을 이용하여 허블상수를 도출하였다. 도출한 값은 8개 초신성을 모두 이용할 경우 $H_0 = 71.15 \pm 1.80 \pm 1.51$ km s^{-1} Mpc^{-1} , 그리고 성간소광의 영향을 덜 받은 6개의 초신성을 이용할 경우 $H_0 = 72.95 \pm 2.03 \pm 1.55$ km s^{-1} Mpc^{-1} 이다. Riess et al. (2016)은 개선된 초신성 보정식을 발표하였다. 개선된 보정식과 성간소광의 영향을 덜 받은 6개의 초신성을 이용할 경우 측정된 허블상수 값은 $H_0 = 70.45 \pm 1.67 \pm 1.65$ km s^{-1} Mpc^{-1} 이다. 이 값은 기존에 세페이드 변광성을 이용하여 측정한 허블상수와 우주배경복사를 이용하여 측정한 허블상수 값의 중간정도 이다.

주요어: 은하: 거리 – 은하: M66, M96, M101, NGC 1309, NGC 3021, NGC 3370, NGC 4038/39, NGC 4258, NGC 5584, – 은하: 별

학 번: 2011-30130